Microstructure and Mechanical Properties of In-situ Synthesized Al_2O_3/Ba-β-Al_2O_3/ZrO_2 Composites

January 2020

Lei LIU

Contents

Chapter 1: Introduction

Conventional structural ceramics such as alumina (Al_2O_3), silicon nitride (Si_3N_4), silicon carbide (SiC), and zirconia (ZrO_2), exhibit excellent mechanical properties and corrosion resistance, as well as good thermodynamic stability [1-4]. These ceramics have already been widely employed in structural applications, such as tiles for aerospace vehicles, thermal barrier coatings for gas turbines, cutting tools for machining, abrasives for polishing and grinding [5-7]. In addition, the high yield stress of ceramics enables the production of precisely machined parts that maintain their accurate dimensions over long periods of use. This is due to the strong chemical bonds formed in ceramics, although it also leads to brittle failure.

1.1 Alumina matrix composites

Al_2O_3 is widely used in many applications such as cutting tools, dental implants, prostheses, electrical and thermal insulators, wear-resistant parts, and coatings because of its high hardness, electrical and thermal insulating properties, excellent oxidation and corrosion resistances, outstanding chemical and thermal stability, as well as low costs and simple processing procedures. Nevertheless, the relatively low fracture toughness considerably limits the large-scale applications of monolithic Al_2O_3 ceramic. Fig. 1.1 shows the schematic illustration of the toughening mechanisms in ceramics [8]. The fracture toughness of ceramics can be enhanced through intrinsic and extrinsic toughening. Al_2O_3 matrix composites containing whiskers, fibers, and platelets with improved fracture toughness have been successfully fabricated [9-17]. In these ceramic matrix composites (CMCs), a tailored interphase, or interface between reinforcements and matrix, plays a crucial role in determining the mechanical properties of the composites. The interphase should be weak enough to allow reinforcements/matrix interfacial debonding and subsequent pullout of reinforcements during fracture. However, the incorporation of fibers, whiskers, and platelets may cause some difficulties in achieving full density, due to the constraint of network formed by the reinforcements. Moreover, there are some difficulties in handling and distributing reinforcements into a matrix homogeneously. Therefore, it is desired to generate elongated reinforcements with high aspect ratios through in-situ reactions during materials processing.

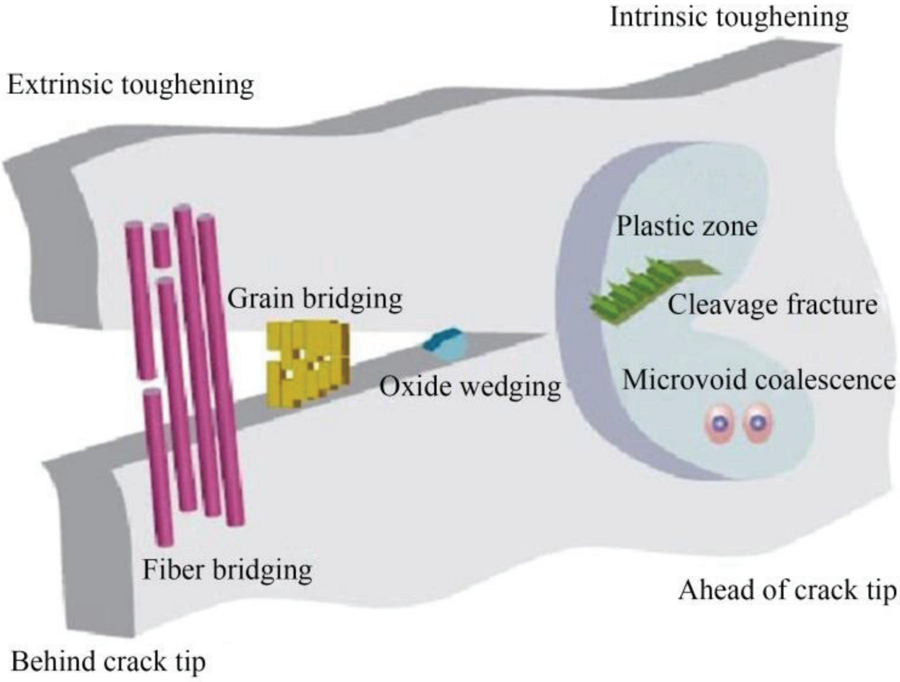

Fig. 1.1 Schematic illustration showing the toughening mechanisms in ceramics [8].

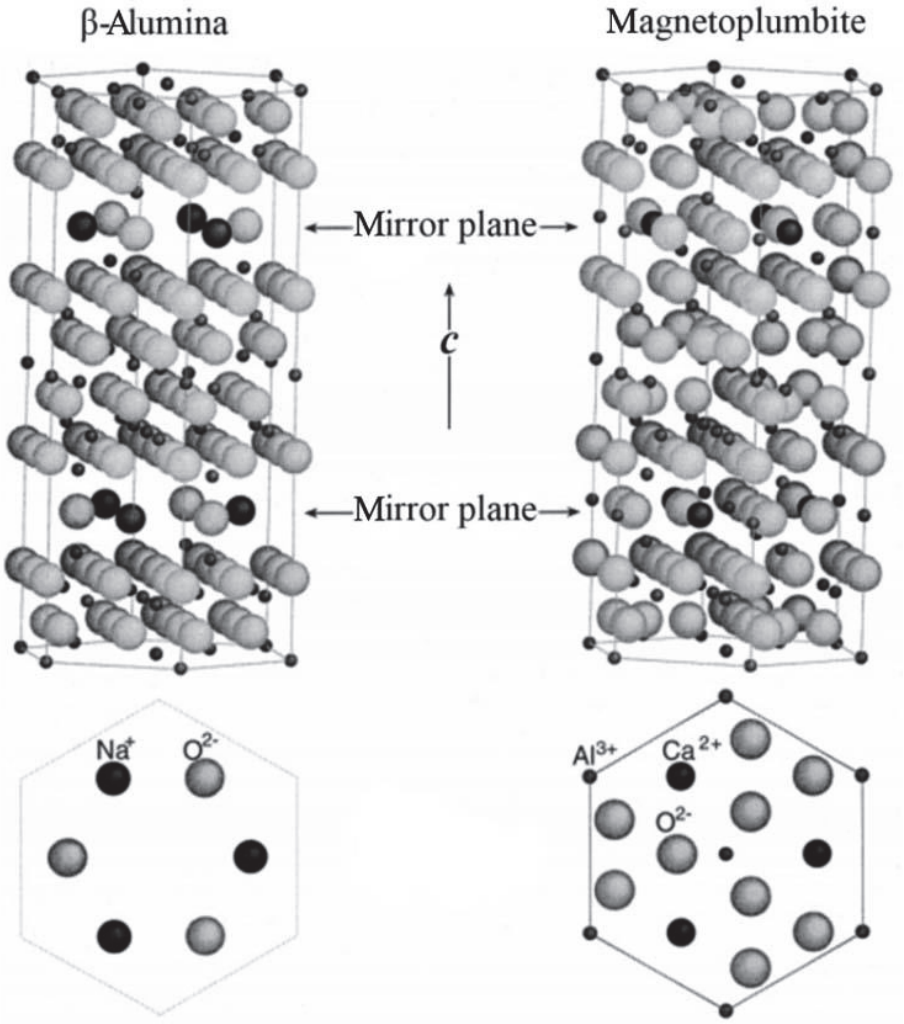

Fig. 1.2 β-Alumina and magnetoplumbite structures [14].

The elongated hexaaluminate compounds with layered β-Al_2O_3 (such as $LaAl_{11}O_{18}$ [18], $BaO\cdot7.3Al_2O_3$ [19], and $SrAl_{12}O_{19}$ [20]) and magnetoplumbite (MP) structures ($LaMgAl_{11}O_{19}$ [21] and $CaAl_{12}O_{19}$ [22]) (Fig. 1.2) have been used as reinforcements. It is well established that barium hexaaluminate is actually constituted by two distinct phases with defective β-Al_2O_3 structure, *i.e.*, $Ba_{0.75}Al_{11}O_{17.25}$ and $Ba_{2.33}Al_{21.33}O_{34.33}$. The present work is focused on the $Ba_{0.75}Al_{11}O_{17.25}$ phase and it is expressed as Ba-β-Al_2O_3. MP and β-Al_2O_3 structures are very similar, and both crystal structures consist of layered spinel blocks ($[Al_{11}O_{16}]^+$) with stabilizing cations and oxygen anions in mirror planes ($[M^{2+}AlO_3]^-$ or $[M^+O]^-$) between the spinel layers [14].

There exists an interfacial or surface energy difference between the basal plane and *c*-axis (perpendicular to basal plane), resulting in growth rate anisotropy in different crystal planes. The formation of hexaaluminate compounds with elongated morphologies is believed to enhance the fracture toughness of the Al_2O_3 matrix composites through crack deflection and crack bridging.

1.2 Zirconia ceramics

Zirconia (ZrO_2) has three crystallographic forms, namely: monoclinic (*m*), tetragonal (*t*), and cubic (*c*) phases (Fig. 1.3). Pure ZrO_2 at ambient pressure is polymorphic, exhibiting *c* structure at high temperatures (>2370 °C), *t* structure at intermediate temperatures (1200–2370 °C), and *m* symmetry at low temperatures (<950 °C). The tetragonal (*t*) to monoclinic (*m*) phase transformation in pure ZrO_2 commences at ~950 °C on cooling and is reversible at ~1150 °C on heating [23-28]. In addition, the stress-activated $t \rightarrow m$ transformation in ZrO_2-based ceramics provided a major impetus into the toughening mechanisms available to enhance the fracture toughness of brittle-matrix materials. ZrO_2-based ceramics are widely used in the structural and multifunctional applications such as solid oxide fuel cells, oxygen sensors, and ceramic membranes, due to chemical inertness, ionic conductivity, good wear resistance, high hardness and melting temperature as well as low coefficient of friction and thermal conductivity [29-33].

1.3 Zirconia toughened alumina ceramics

Zirconia toughened alumina (ZTA) ceramics, in which zirconia particles are dispersed as a second phase in the Al_2O_3 matrix, are currently of great interest for many fields, particularly in biomedical applications [34-37]. The introduction of small amount of ZrO_2 into Al_2O_3 matrix causes the formation of solid solutions, as can be seen from the Al_2O_3–ZrO_2 phase diagram (Fig. 1.4). The solid solutions promote the densification of the Al_2O_3-based composites by the introduction of lattice defects [38,39]. ZTA ceramics have improved mechanical properties with higher ageing resistance, which is attributed to high hardness contributed by alumina and fracture toughness provided by stabilized zirconia. The toughening mechanisms in ZTA ceramic materials are mainly composed of martensitic transformation of ZrO_2 and subsequent microcracking.

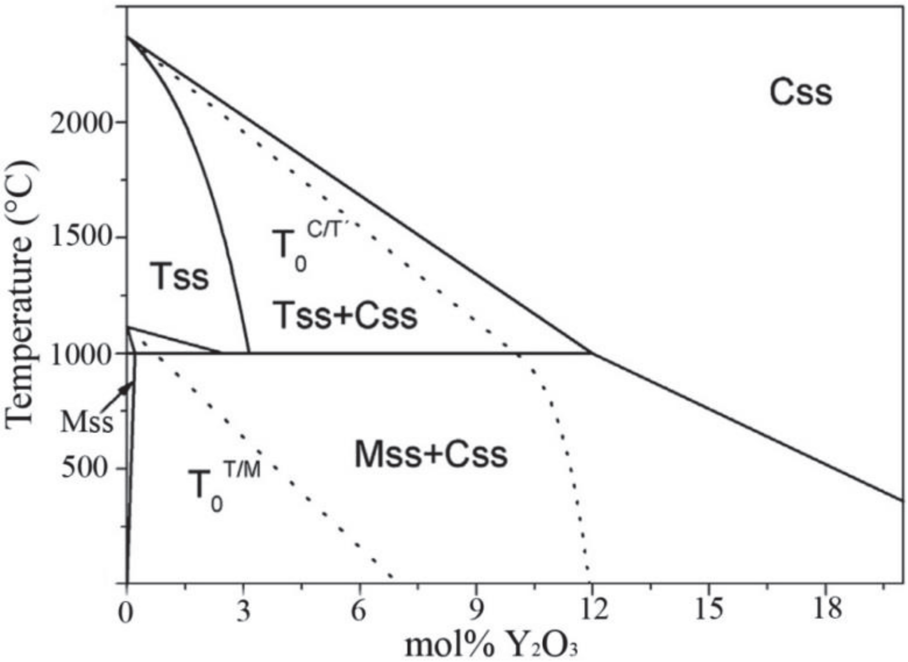

Fig. 1.3 Phase diagram of ZrO_2–Y_2O_3 system [24].

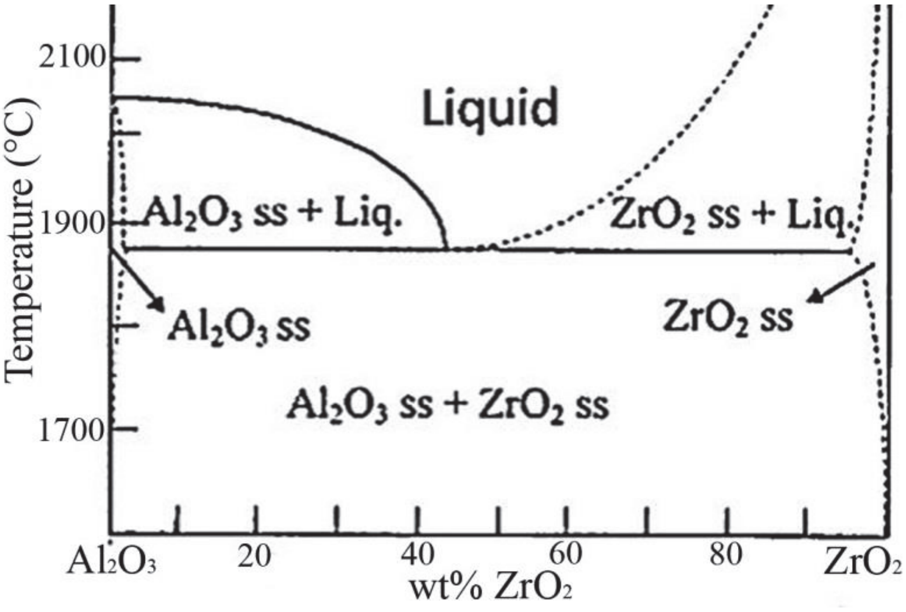

Fig. 1.4 Phase diagram of Al_2O_3–ZrO_2 system [28].

1.4 Purpose and significance of present work

Al_2O_3/Ba-β-Al_2O_3/ZrO_2 composites with improved fracture toughness, as a result of multiple toughening effects including crack deflection, crack bridging, and martensitic transformation of ZrO_2 from tetragonal to monoclinic phase, were successfully fabricated in the present work. The purpose is to understand the relationships among processing conditions, densification behavior, microstructure, mechanical properties, and thermal shock resistance, thus to promote their industrial applications and contribute to enhance the reliability and service life of Al_2O_3 matrix composites.

1.5 Outline of this work

This research focused on the fabrication and mechanical properties improvement of Al_2O_3/Ba-β-Al_2O_3/ZrO_2 composites. In Chapter 1, the background of present work was described. In order to enhance the fracture toughness of Al_2O_3 ceramic, a combination of crack deflection, crack bridging, and martensitic transformation of ZrO_2 from tetragonal to monoclinic phase was proposed to fabricate Al_2O_3/Ba-β-Al_2O_3/ZrO_2 composites.

In Chapter 2, the fabrication of Al_2O_3/Ba-β-Al_2O_3/ZrO_2 composites with 3 mol% yttria-stabilized zirconia (3YSZ) addition using solid-state reaction sintering of Al_2O_3, barium zirconate ($BaZrO_3$), and 3YSZ powders has been investigated. The effects of 3YSZ addition on densification behavior, phase evolution, microstructure, and mechanical properties were also discussed.

In Chapter 3, Al_2O_3/Ba-β-Al_2O_3/ZrO_2 composites were prepared via reactive sintering of Al_2O_3 and $BaZrO_3$ powders with additions of 1.5YSZ, 2YSZ, 3YSZ, and yttria (Y_2O_3), and the effects of YSZ with different Y_2O_3 contents and Y_2O_3 additions on microstructure and mechanical properties of Al_2O_3/Ba-β-Al_2O_3/ZrO_2 composites were investigated.

In Chapter 4, to obtain dense composites at a lower temperature, Al_2O_3/Ba-β-Al_2O_3/ZrO_2 composites were prepared by solid-state reaction sintering of high-energy ball-milled Al_2O_3–$BaZrO_3$ powder mixtures and YSZ nanopowder, and the influences of high-energy ball-milling (HEBM) on sintering ability, microstructure, and mechanical properties of Al_2O_3/Ba-β-Al_2O_3/ZrO_2 composites were also investigated.

In Chapter 5, to improve the mechanical properties and thermal shock resistance of ZTA composites, barium carbonate ($BaCO_3$) was added to the powder mixtures of

Al_2O_3 and 3YSZ, fabricated by a solid-state reactive sintering method. The effects of in-situ synthesized Ba-β-Al_2O_3 on densification behavior, phase evolution, microstructure, mechanical properties, and thermal shock resistance of ZTA composites were also investigated.

In Chapter 6, calcium hexaaluminate ($CaAl_{12}O_{19}$, or CA_6) ceramics were fabricated by solid-state reaction sintering of Al_2O_3 and calcium carbonate ($CaCO_3$) powder mixtures. The aim was to fabricate denser CA_6 ceramics and investigate the influence of titania (TiO_2) addition on densification behavior, phase evolution, and microstructure of CA_6 ceramics.

In Chapter 7, some general conclusions of this work were made. In addition, a few schedules to motivate the future research were also proposed.

References

1. A. Okada, Automotive and industrial applications of structural ceramics in Japan, J. Eur. Ceram. Soc. 28 (2008) 1097–1104.
2. J.R. Kelly, I. Denry, Stabilized zirconia as a structural ceramic: an overview, Dent. Mater. 24 (2008) 289–298.
3. S.M. Wiederhorn, B.J. Hockey, J.D. French, Mechanisms of deformation of silicon nitride and silicon carbide at high temperatures, J. Eur. Ceram. Soc. 19 (1999) 2273–2284.
4. N.P. Padture, Advanced structural ceramics in aerospace propulsion, Nat. Mater. 15 (2016) 804–809.
5. F. Bouville, E. Maire, S. Meille, B. Van de Moortèle, A.J. Stevenson, S. Deville, Strong, tough and stiff bioinspired ceramics from brittle constituents, Nat. Mater. 13 (2014) 508–514.
6. Y.W. Kim, Y.S. Chun, T. Nishimura, M. Mitomo, Y.H. Lee, High-temperature strength of silicon carbide ceramics sintered with rare-earth oxide and aluminum nitride, Acta. Mater. 55 (2007) 727–736.
7. Z.C. Chen, S. Nugroho, M. Ezumi, T. Akao, T. Onda, In-situ synthesis of alumina-matrix oxide/oxide composites by reactive sintering, Mater. Sci. Eng. A 557 (2012) 59–68.
8. R.O. Ritchie, The conflicts between strength and toughness, Nat. Mater. 10 (2011) 817–822.
9. K. Takahashi, M. Yokouchi, S.K. Lee, K. Ando, Crack-healing behavior of Al_2O_3

toughened by SiC whiskers, J. Am. Ceram. Soc. 86 (2003) 2143–2147.

10. J. Liu, H.X. Yan, M.J. Reece, K. Jiang, Toughening of zirconia/alumina composites by the addition of graphene platelets, J. Eur. Ceram. Soc. 32 (2012) 4185–4193.
11. B. Lee, M.Y. Koo, S.H. Jin, K.T. Kim, S.H. Hong, Simultaneous strengthening and toughening of reduced graphene oxide/alumina composites fabricated by molecular-level mixing process, Carbon 78 (2014) 212–219.
12. Z.C. Chen, S. Duncan, K.K. Chawla, M. Koopman, G.M. Janowski, Characterization of interfacial reaction products in alumina fiber/barium zirconate coating/alumina matrix composite, Mater. Charact. 48 (2002) 305–314.
13. Z.C. Chen, T. Tamachi, R. Kulkarni, K.K. Chawla, M. Koopman, Interfacial reaction behavior and thermal stability of barium zirconate-coated alumina fiber/alumina matrix composites, J. Eur. Ceram. Soc. 28 (2008) 1149–1160.
14. M.K. Cinibulk, Hexaluminates as a cleavable fiber-matrix interphase: synthesis, texture development, and phase compatibility, J. Eur. Ceram. Soc. 20 (2000) 569–582.
15. M.K. Cinibulk, R.S. Hay, Textured magnetoplumbite fiber-matrix interphase derived from sol-gel fiber coatings, J. Am. Ceram. Soc. 79 (1996) 1233–1246.
16. J.J. Cao, H.H. Chen, F. Du, H.C. Zhao, L. Fan, Preliminary study of in situ transformed carbon fibers/Al_2O_3 ceramic matrix composites, Ceram. Int. 39 (2013) 7037–7042.
17. S.J. Lee, W.M. Kriven, Toughened oxide composites based on porous

alumina-platelet interphases, J. Am. Ceram. Soc. 84 (2001) 767–774.

18. Z. Negahdari, M. Willert-Porada, Tailoring the microstructure of reaction-sintered alumina/lanthanum hexaaluminate particulate composites, J. Eur. Ceram. Soc. 30 (2010) 1381–1389.
19. Z.C. Chen, K.K. Chawla, M. Koopman, Microstructure and mechanical properties of in situ synthesized alumina/Ba-β-alumina/zirconia composites, Mater. Sci. Eng. A 367 (2004) 24–32.
20. K. Vishista, F.D. Gnanam, Microstructural development of $SrAl_{12}O_{19}$ in alumina-strontia composites, J. Eur. Ceram. Soc. 29 (2009) 77–83.
21. H. Tang, M.H. Fang, X. Min, X.J. Wang, Z.H. Huang, R.L. Wen, Y.A. Liu, X.W. Wu, Mechanical properties and solid particle erosion behavior of $LaMgAl_{11}O_{19}$-Al_2O_3 ceramic at room and elevated temperatures, J. Am. Ceram. Soc. 99 (2016) 2138–2146.
22. D. Asmi, I.M. Low, Processing of an in-situ layered and graded alumina/calcium-hexaluminate composite: physical characteristics, J. Eur. Ceram. Soc. 18 (1998) 2019–2024.
23. J.A. Krogstad, R.M. Leckie, S. Krämer, J.M. Cairney, D.M. Lipkin, C.A. Johnson, C.G. Levi, Phase evolution upon aging of air plasma sprayed *t′*-zirconia coatings: II–microstructure evolution, J. Am. Ceram. Soc. 96 (2013) 299–307.
24. I.O. Fábregas, M. Reinoso, E. Otal, M. Kim, Grain-size/(*t″*_or *c*)-phase relationship in dense ZrO_2 ceramics, J. Eur. Ceram. Soc. 36 (2016) 2043–2049.
25. W.H. Tuan, R.Z. Chen, T.C. Wang, C.H. Cheng, P.S. Kuo, Mechanical properties

of Al_2O_3/ZrO_2 composites, J. Eur. Ceram. Soc. 22 (2002) 2827–2833.

26. C. Meunier, F. Zuo, N. Peillon, S. Saunier, S. Marinel, D. Goeuriot, In situ study on microwave sintering of ZTA ceramic: Effect of ZrO_2 content on densification, hardness, and toughness, J. Am. Ceram. Soc. 100 (2017) 929–936.
27. R.H.J. Hannink, P.M. Kelly, B.C. Muddle, Transformation toughening in zirconia-containing ceramics, J. Am. Ceram. Soc. 83 (2000) 461–487.
28. K. Maiti, A. Sil, Microstructural relationship with fracture toughness of undoped and rare earths (Y, La) doped Al_2O_3–ZrO_2 ceramic composites, Ceram. Int. 37 (2011) 2411–2421.
29. D. Glymond, M.J. Vick, F. Giuliani, L.J. Vandeperre, High-temperature fracture toughness of mullite with monoclinic zirconia, J. Am. Ceram. Soc. 100 (2017) 1570–1577.
30. J.H. Shin, S.H. Hong, Fabrication and properties of reduced graphene oxide reinforced yttria-stabilized zirconia composite ceramics, J. Eur. Ceram. Soc. 34 (2014) 1297–1302.
31. F. Zhang, K. Vanmeensel, M. Inokoshi, M. Batuk, J. Hadermann, B. Van Meerbeek, I. Naert, J. Vleugels, 3Y-TZP ceramics with improved hydrothermal degradation resistance and fracture toughness, J. Eur. Ceram. Soc. 34 (2014) 2453–2463.
32. W.J. Xue, Z.P. Xie, J. Yi, J. Chen, Critical grain size and fracture toughness of 2 mol.% yttria-stabilized zirconia at ambient and cryogenic temperatures, Scripta mater. 67 (2012) 963–966.

33. I. Hussainova, M. Drozdova, D. Pérez-Coll, F. Rubio-Marcos, I. Jasiuk, J.A.N.T. Soares, M.A. Rodríguez, Electroconductive composite of zirconia and hybrid graphene/alumina nanofibers, J. Eur. Ceram. Soc. 37 (2017) 3713–3719.

34. X.Q. Xu, X.X. Hu, S. Ren, H.T. Geng, H.Y. Du, J.C. Liu, Fine grained Al_2O_3-ZrO_2 (Y_2O_3) ceramics by controlled crystallization of amorphous phase, J. Eur. Ceram. Soc. 36 (2016) 1791–1796.

35. F. Sommer, R. Landfried, F. Kern, R. Gadow, Mechanical properties of zirconia toughened alumina with 10-24 vol.% 1Y-TZP reinforcement, J. Eur. Ceram. Soc. 32 (2012) 4177–4184.

36. D. Trejo-Arroyo, J. Zárate-Medina, J.M. Alvarado-Orozco, M.E. Contreras-García, M.S. Boldrick, J. Muñoz-Saldaña, Microstructure and mechanical properties of Al_2O_3-YSZ spherical polycrystalline composites, J. Eur. Ceram. Soc. 33 (2013) 1907–1916.

37. A. Larrea, V.M. Orera, R.I. Merino, J.I. Peña, Microstructure and mechanical properties of Al_2O_3-YSZ and Al_2O_3-YAG directionally solidified eutectic plates, J. Eur. Ceram. Soc. 25 (2005) 1419–1429.

38. H.P. Cahoon, C.J. Christensen, Sintering and grain growth of alpha-alumina, J. Am. Ceram. Soc. 39 (1956) 337–344.

39. M.M.R. Boutz, A.J.A. Winnubst, F. Hartgers, A.J. Burggraaf, Effect of additives on densification and deformation of tetragonal zirconia, J. Mater. Sci. 29 (1994) 5374–5382.

Chapter 2: Microstructure and improved mechanical properties of Al_2O_3/Ba-β-Al_2O_3/ZrO_2 composites with YSZ addition

2.1 Introduction

Self-reinforced Al_2O_3 matrix composites with improved fracture toughness have been developed by incorporating various hexaaluminate compounds such as $CaAl_{12}O_{19}$ [1-3], $SrAl_{12}O_{19}$ [4,5], $Ba_{0.75}Al_{11}O_{17.25}$ (one of Ba-β-Al_2O_3 compounds) [6,7], $LaAl_{11}O_{18}$ [8,9], and $LaMgAl_{11}O_{19}$ [10,11]. The formation of these hexaaluminate compounds with elongated morphologies resulted in enhancement of fracture toughness of Al_2O_3 ceramic due to crack deflection and crack bridging. Meanwhile, the phase transformation of ZrO_2 from tetragonal (*t*) to monoclinic (*m*) has been widely used to improve the fracture toughness of Al_2O_3 [12-15]. Based on above-mentioned toughening mechanisms, some researchers [16-18] have introduced multiple reinforcing phases into Al_2O_3 matrix. The in-situ formed $SrAl_{12}O_{19}$, $LaAl_{11}O_{18}$, and $CaAl_{12}O_{19}$ enhanced the fracture toughness of zirconia toughened alumina (ZTA) composites. Nevertheless, almost all studies dealt with the influences of elongated reinforcements on microstructure and mechanical properties of ZTA composites. So far, little research work has been focused on the effects of YSZ addition on microstructure and mechanical properties of Al_2O_3/hexaaluminate composites. Burger et al. [19] prepared an Al_2O_3 matrix composites containing homogeneously distributed metastable ZrO_2 particles and in-situ formed hexagonal $SrAl_{12}O_{19}$ platelets and investigated the effects of ZrO_2 addition on strength, fracture toughness, and wear resistance of $Al_2O_3/SrAl_{12}O_{19}$ composites.

Chen et al. have examined the in-situ synthesis of Al_2O_3 matrix composites by using reactive sintering of Al_2O_3 and $BaZrO_3$ powders [6,7]. At high temperatures, the chemical reactions between Al_2O_3 and $BaZrO_3$ can be expressed as [6,7]

$$BaZrO_3 + 7.3Al_2O_3 = BaO\cdot 7.3Al_2O_3 + ZrO_2 \tag{2.1}$$

As a result of the above reaction, the elongated $BaO\cdot 7.3Al_2O_3$ phase and *m*-ZrO_2 particles were produced during sintering period. $BaO\cdot 7.3Al_2O_3$ is one of the Ba-β-Al_2O_3 compounds and it will be described as Ba-β-Al_2O_3 hereafter. Since the reaction-formed ZrO_2 is completely monoclinic phase (*m*-ZrO_2), the fracture toughness enhancement of the obtained Al_2O_3 matrix composites is mainly attributed to the contribution of Ba-β-Al_2O_3 phase through crack deflection and crack bridging.

In this chapter, an attempt has been made to introduce yttria-stabilized zirconia (YSZ) powder to Al_2O_3 and $BaZrO_3$ powder mixtures and to promote the formation of tetragonal zirconia (*t*-ZrO_2) during reactive sintering. In this way, the fracture toughness of the Al_2O_3 matrix composites containing both Ba-β-Al_2O_3 and *t*-ZrO_2 may be further improved as a result of multiple toughening effects including crack deflection, crack bridging, and martensitic transformation of ZrO_2 from tetragonal to monoclinic phase. The objective of this chapter was to clarify the effects of YSZ addition on densification behavior, phase evolution, microstructure, and mechanical properties of Al_2O_3/Ba-β-Al_2O_3/ZrO_2 composites and to understand the mechanisms of improving the mechanical properties of these in-situ synthesized Al_2O_3 matrix composites.

2.2 Experimental procedure

The starting materials used in this study were Al_2O_3 (average particle size 0.16 µm, 99.99% purity; Taimei Chemicals, Tokyo, Japan), $BaZrO_3$ (1.5 µm, 99% purity; Kojundo Chemical Lab., Saitama, Japan), and 3YSZ (3 mol% Y_2O_3-ZrO_2 (TZ-3Y); 50 nm, 99.9% purity; Tosoh, Tokyo) powders. The raw powders with nominal compositions listed in Table 2.1 were mixed in ethanol for 24 h at a speed of 90 rpm with Al_2O_3 balls of 5 mm diameter (grade SSA-995, NIKKATO, Osaka, Japan) as milling media. For simplicity's sake, in the present paper, the composites containing both reaction-formed ZrO_2 and added YSZ are expressed as Al_2O_3/Ba-β-Al_2O_3/ZrO_2, whereas Al_2O_3/Ba-β-Al_2O_3/*m*-ZrO_2 implies the composites without YSZ addition. After milling, the slurries were dried at 120 °C for 24 h. The disk-shaped green compacts (Φ19 mm × 3 mm) were prepared by uniaxial pressing at 20 MPa for 2 min, followed by cold isostatic pressing at 200 MPa for 2 min. The obtained green compacts were sintered in an electric furnace at 1400, 1500, and 1600 °C in air with a heating rate of 400 °C/h and a dwelling time of 2 h at each temperature. The specimens were then cooled down to room temperature at a rate of 400 °C/h. In addition, some AB-8Z specimens were subjected to the following thermal shock test. The specimens were heated from room temperature to 1100 °C with a heating rate of 400 °C/h in a furnace. After heating at 1100 °C for 15 min, the specimens were taken out of the furnace and cooled in air to room temperature. This process was repeated for 5 times.

Table 2.1 Nominal compositions of Al_2O_3/Ba-β-Al_2O_3/ZrO_2 composites (vol%).

Samples	Al_2O_3	Ba-β-Al_2O_3	ZrO_2	3YSZ
AB-2.5Z	70	27.5	2.5	0
AB-8Z	72	20	1.8	6.2
AB-16Z	64	20	1.8	14.2

Density values of the sintered samples were measured in distilled water using the Archimedes principle. The phase identification of mixed powder, sintered samples, and fractured surfaces was performed by X-ray diffraction (XRD; RINT-TTR III, Rigaku, Japan) using Cu Kα radiation with a step of 0.02° (2θ) and a scanning rate of 2 °/min ranging from 15° to 75°. The volume fractions of monoclinic and tetragonal ZrO_2 phases (V_{m} and V_{t}) were calculated by the modified Garvie and Nicholson equation [20].

$$X_{\mathrm{m}} = \frac{I_{\mathrm{m}(1\,1\,1)} + I_{\mathrm{m}(1\,1\,\bar{1})}}{I_{\mathrm{m}(1\,1\,1)} + I_{\mathrm{m}(1\,1\,\bar{1})} + I_{\mathrm{t}(1\,1\,1)}} \tag{2.2}$$

$$V_{\mathrm{m}} = \frac{1.311 X_{\mathrm{m}}}{1 + 0.311 X_{\mathrm{m}}} \tag{2.3}$$

$$V_{\mathrm{t}} = 1 - V_{\mathrm{m}} \tag{2.4}$$

where X_{m} is the intensity ratio. $I_{\mathrm{t}(1\,1\,1)}$, $I_{\mathrm{m}(1\,1\,\bar{1})}$, and $I_{\mathrm{m}(1\,1\,1)}$ are the peak intensities corresponding to the tetragonal $(1\ 1\ 1)$, monoclinic $(1\ 1\ \bar{1})$, and monoclinic $(1\ 1\ 1)$ planes, respectively.

Microstructural observations and compositional analyses were conducted by scanning electron microscopy (SEM; JXA-9800RL, JEOL, Japan) and electron probe micro-analyzer (EPMA; JXA-9800RL, JEOL), respectively. In addition, transmission electron microscopy (TEM; JEM-2010, JEOL) attached with energy-dispersive spectroscopy (EDS) was also used for microstructural evaluation. Thermal etching was performed by heating the polished samples in air to 1300 °C for 30 min for the purpose of measuring the grain sizes of the Al_2O_3 matrix. The average grain size of the Al_2O_3 matrix was determined quantitatively using the linear intercept method with the 1.56 correction, and the aspect ratio of the Ba-β-Al_2O_3 phase was obtained by directly measuring the length and width on SEM micrographs.

The flexural strength was measured by four-point bending tests with a crosshead loading rate of 0.5 mm/min. The nominal size of test specimens was 3 mm × 4 mm × 36 mm, and the upper and lower spans were 10 mm and 30 mm, respectively. Each specimen was polished with diamond paste (3 μm) and the edges were chamfered (about 45^{o}). At least 8 specimens were tested for each condition, and the average values were reported. Furthermore, the Vickers hardness and fracture toughness were determined by an indentation method with a load of 98 N (15 s holding), and the fracture toughness was calculated by the following equation [21].

$$K_{\mathrm{IC}} = 0.16 HV \cdot a^{1/2} \cdot (c/a)^{-3/2} \tag{2.5}$$

where K_{IC} is the fracture toughness (MPa m$^{1/2}$), HV is the Vickers hardness (MPa), a is the half diagonal length of the indentation (m), and c is the half length of the radical crack (m). 10 indentations were made to obtain representative mean values of hardness and toughness.

2.3 Results and discussion

2.3.1 Densification behavior and phase analysis

The relative density of the in-situ synthesized samples sintered at different temperatures is shown in Fig. 2.1. All the samples showed similar densification trend with increasing sintering temperature. The composites with a higher YSZ content exhibited higher relative density, and the relative density values of all the samples were higher than 98% at 1600 °C. This indicates that the addition of YSZ particles promotes the densification of the Al_2O_3 matrix composites. Similar results have also been found in the sintering of Al_2O_3–ZrO_2 composites [22-24]. The densification improvement may be attributed to much larger diffusion coefficients of Zr^{4+} and O^{2-} in ZrO_2 than those of Al^{3+} and O^{2-} in Al_2O_3, respectively [25]. Furthermore, the homogeneous dispersion of the added YSZ particles in Al_2O_3 matrix can effectively restrain the abnormal grain growth of Al_2O_3 matrix, thus accelerating the densification of the composites [22].

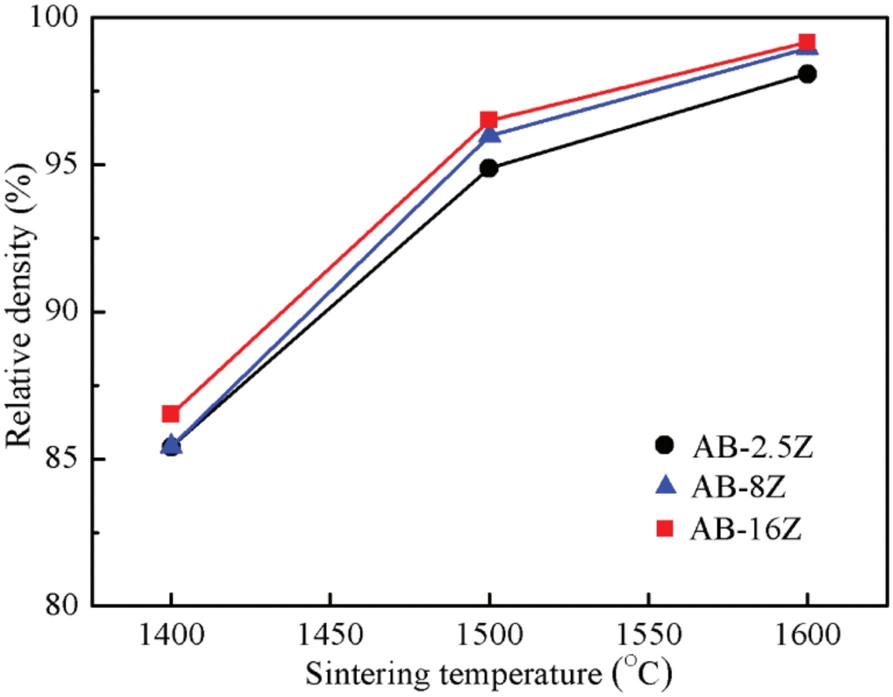

Fig. 2.1 Relative density of the different samples sintered at different temperatures.

Fig. 2.2 shows the XRD patterns of the mixed powder and sintered AB-8Z samples in a temperature range of 1400-1600 °C. At 1400 °C, no peaks of $BaZrO_3$ or $BaO \cdot Al_2O_3$ were detected within the detection limit of the XRD analysis. Instead, the peaks corresponding to Ba-β-Al_2O_3 and ZrO_2 phases were found. It is noted that the ZrO_2 phase existed in both *m*-ZrO_2 and *t*-ZrO_2 forms. No evident changes in XRD patterns could be observed with the increase in sintering temperature. However, the *m*-ZrO_2 almost disappeared at 1600 °C.

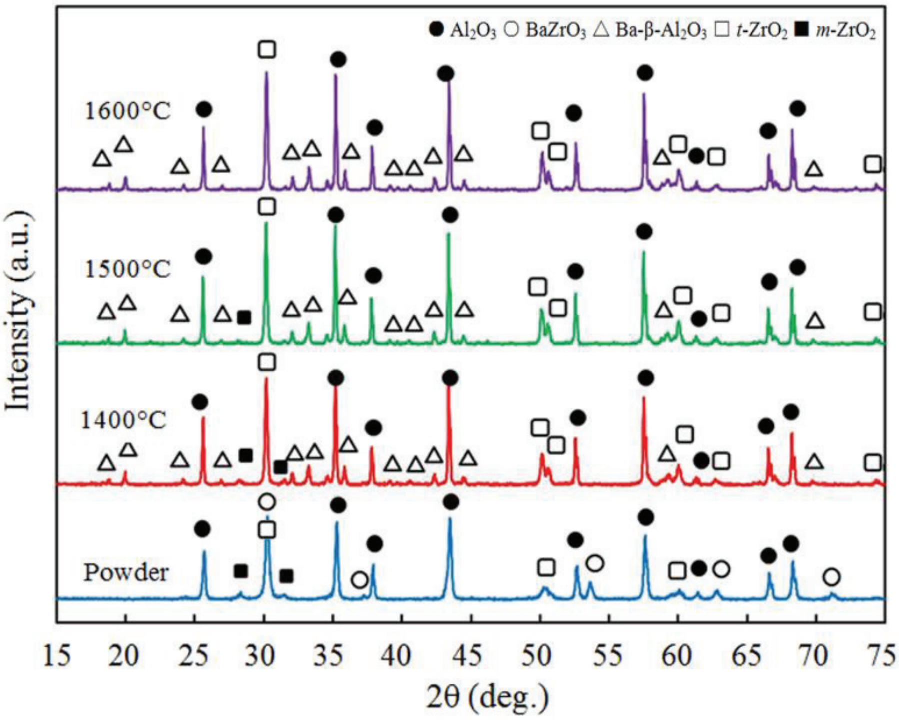

Fig. 2.2 XRD patterns of mixed powder and sintered AB-8Z at different sintering temperatures.

The volume fractions of *m*-ZrO_2 phase in AB-8Z and AB-16Z samples sintered at different temperatures are shown in Fig. 2.3. The amount of *m*-ZrO_2 was gradually reduced with increasing sintering temperature. This suggests that more Y^{3+} diffuses from the initial YSZ particles into *m*-ZrO_2 at higher temperatures, which is formed through the reactions between Al_2O_3 and $BaZrO_3$, thus resulting in the stabilization of *m*-ZrO_2 and formation of more *t*-ZrO_2 phase. It can be concluded from Fig. 2.3 that the majority of ZrO_2 in the in-situ synthesized Al_2O_3/Ba-β-Al_2O_3/ZrO_2 composites are present in *t*-ZrO_2 form. Furthermore, AB-16Z samples showed higher volume fractions of *t*-ZrO_2 than AB-8Z samples, because the former had a higher Y_2O_3 content than the latter.

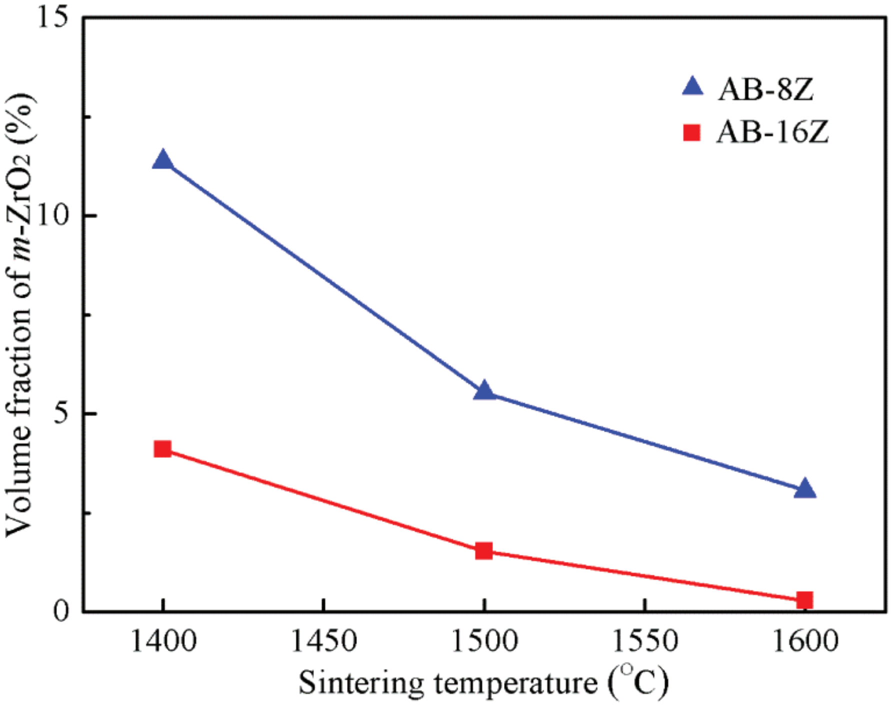

Fig. 2.3 Volume fractions of monoclinic ZrO_2 phase in AB-8Z and AB-16Z samples as a function of sintering temperature.

2.3.2 Microstructure

Fig. 2.4 shows the SEM images (backscattered electron mode) of the samples sintered at 1600 °C. Based on the results of XRD (Fig. 2.2) and EPMA (Fig. 2.5) analyses, the dark and white phases corresponded to Al_2O_3 matrix and ZrO_2 particles, respectively, while the gray phase with a platelet morphology was Ba-β-Al_2O_3. For the samples with YSZ addition (Fig. 2.4(b) and (c)), the white ZrO_2 particles included

YSZ added directly and ZrO_2 formed through the reactions between Al_2O_3 and $BaZrO_3$ during reactive sintering. In comparison with the images shown in Fig. 2.4, it seems that the particle sizes of most added YSZ were smaller than those of the reaction-formed ZrO_2 in AB-8Z sample. Nevertheless, the agglomeration of some YSZ particles was observed in AB-16Z sample due to its high YSZ content.

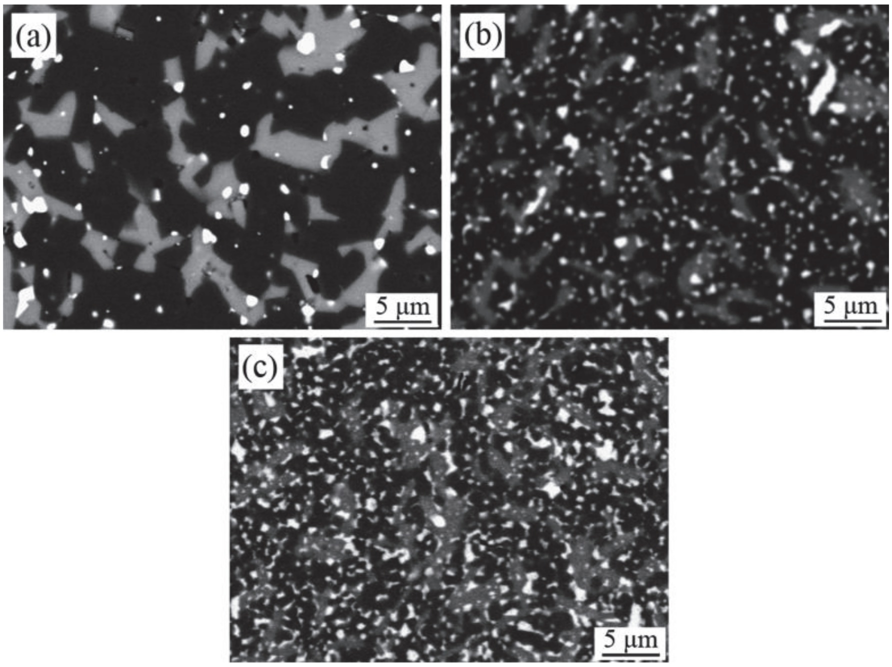

Fig. 2.4 SEM images (backscattered electron mode) showing the microstructure of samples sintered at 1600 °C. (a) AB-2.5Z, (b) AB-8Z, and (c) AB-16Z.

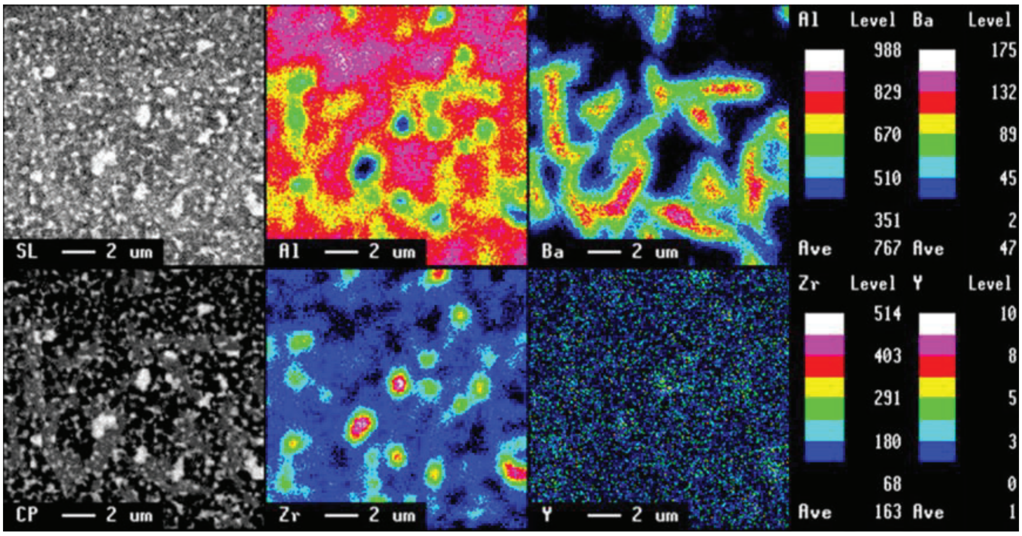

Fig. 2.5 EPMA results of AB-16Z sample sintered at 1600 °C.

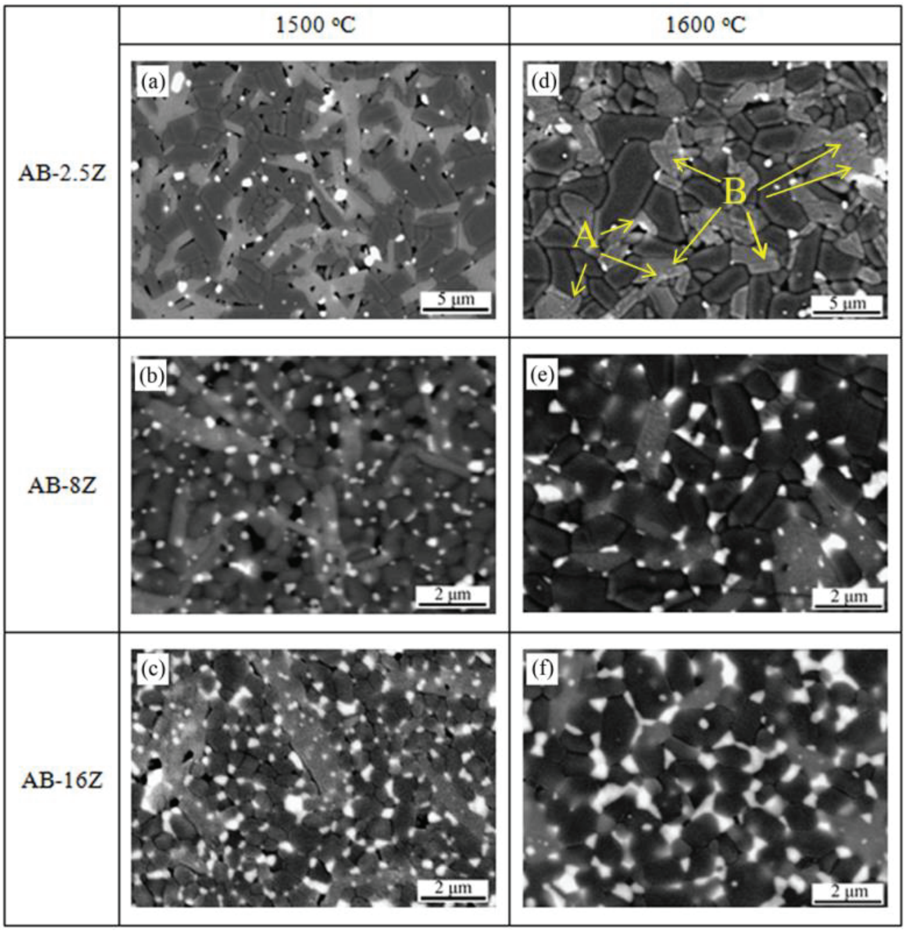

Fig. 2.6 SEM images (backscattered electron mode) showing the microstructure of thermally etched samples sintered at 1500 and 1600 °C.

The SEM images of the thermally etched samples sintered at 1500 and 1600 °C are shown in Fig. 2.6. Some small pores still existed in the composites sintered at 1500 °C (Fig. 2.6(a)-(c)). After sintering at 1600 °C, denser microstructure as well as significant growth of both Al_2O_3 grains and ZrO_2 particles were observed, whereas the aspect ratios of the Ba-β-Al_2O_3 decreased. The reduction of the aspect ratios of the Ba-β-Al_2O_3 at a higher temperature may be due to the following two reasons. The growth of Ba-β-Al_2O_3 phase along its basal plane is clamped by the neighboring Ba-β-Al_2O_3, as indicated by the arrows “A” in Fig. 2.6(d). Thus, the growth proceeds in *c*-axis (perpendicular to basal plane). Another reason is the coalescence of neighboring Ba-β-Al_2O_3 when they are disposed with their basal planes parallelly [26,27], as it can be seen that some of these boundaries began to disappear (the arrows "B" in Fig. 2.6(d)). In addition, most YSZ particles were located at the grain boundaries of the Al_2O_3 matrix, resulting in smaller grain sizes of the Al_2O_3 matrix.

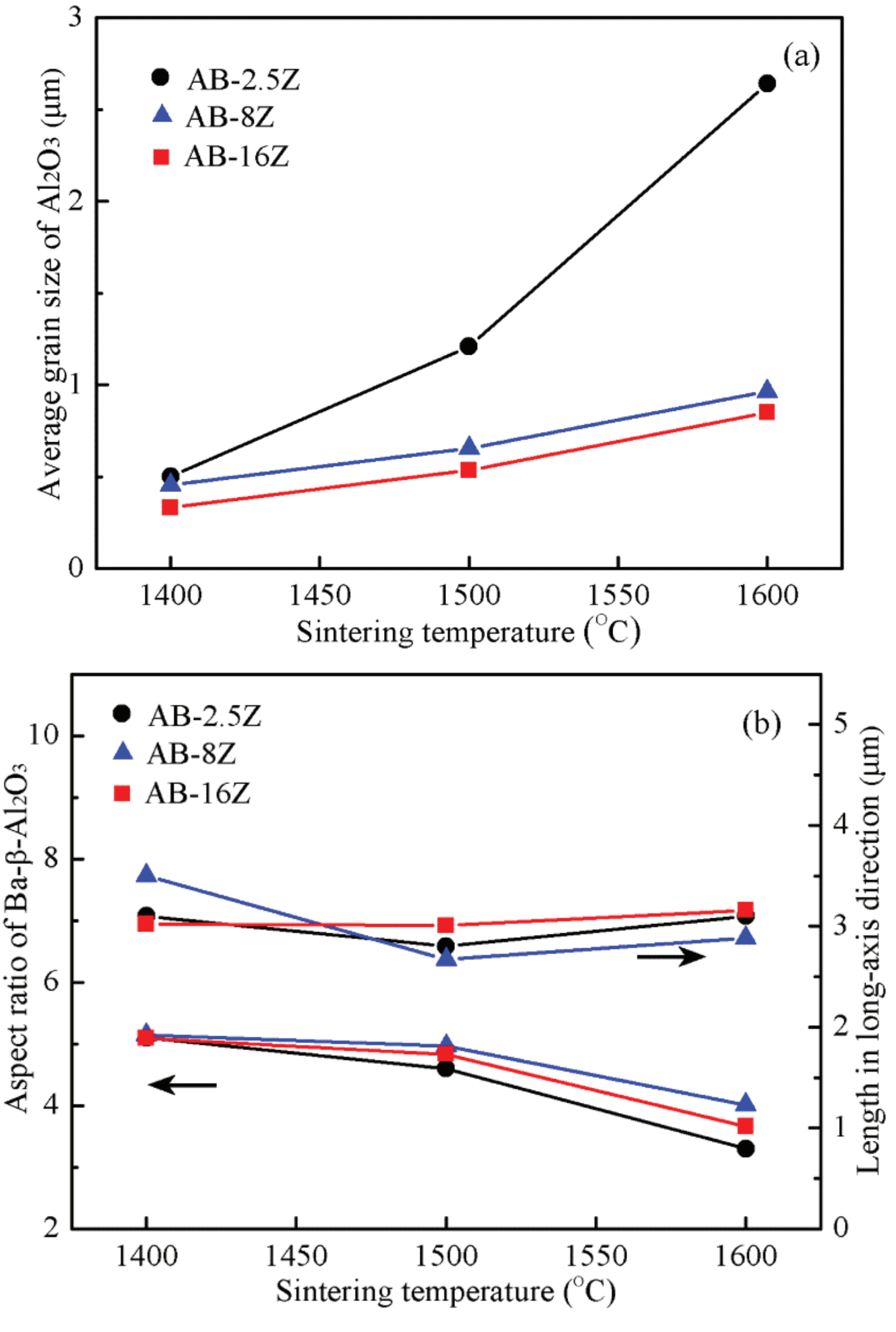

Fig. 2.7 Average grain size of (a) A_2O_3 matrix as well as (b) aspect ratio and length in long-axis direction of Ba-β-Al_2O_3 phase as a function of sintering temperature.

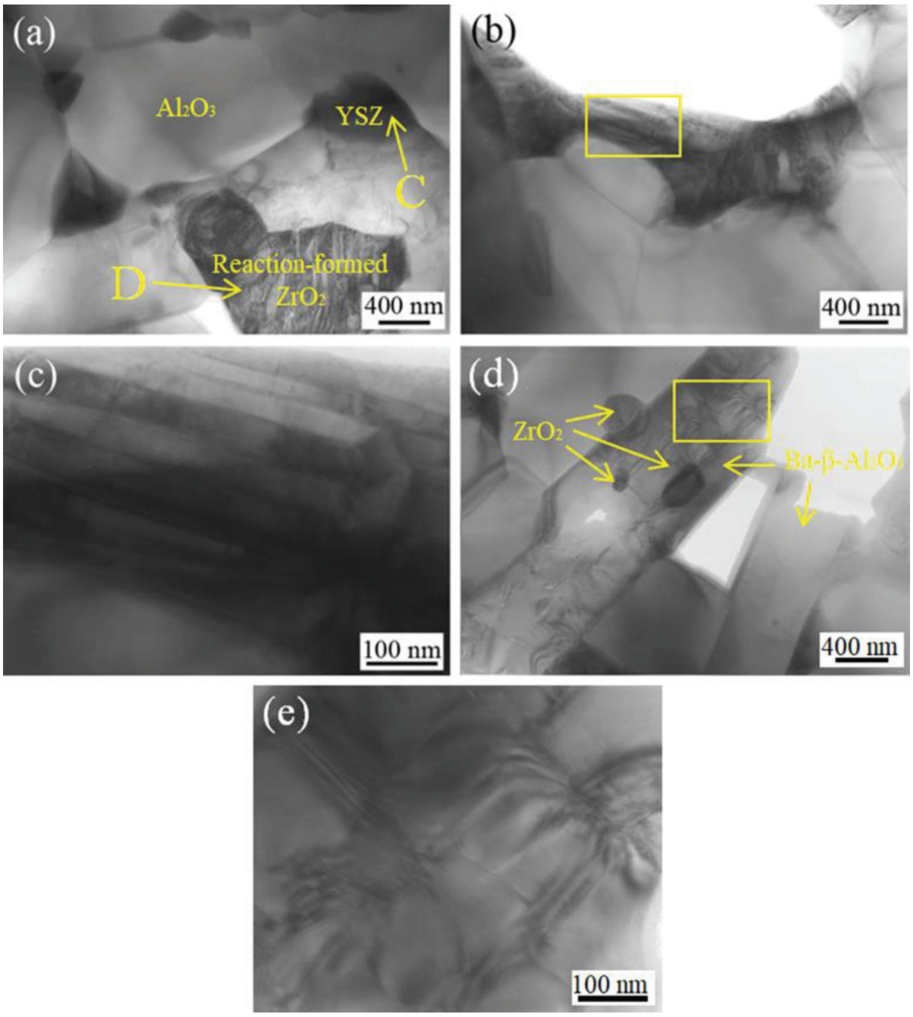

Fig. 2.8 TEM results of AB-8Z sample sintered at 1600 °C. TEM images showing (a) Al_2O_3, YSZ, and reaction-formed ZrO_2, (b) band structure of reaction-formed ZrO_2, (c) magnified view of the marked rectangular region in (b), (d) Ba-β-Al_2O_3, and (e) magnified view of the marked rectangular region in (d).

Table 2.2 EDS analyses of YSZ and ZrO_2 pointed by arrows “C” and ”D” in Fig. 2.8(a).

Positions	ZrO_2 (wt%)	Y_2O_3 (wt%)	Al_2O_3 (wt%)	BaO (wt%)
C	94.0	4.9	1.1	0
D	97.0	2.3	0.5	0.2

Fig. 2.7 illustrates the average grain size of the Al_2O_3 matrix as well as the aspect ratio and length in long-axis direction of the Ba-β-Al_2O_3 phase as a function of sintering temperature. At 1400 °C, no significant differences in average grain size of the Al_2O_3 matrix were observed. As the sintering temperature increased, rapid grain

growth occurred in AB-2.5Z, but AB-8Z and AB-16Z still exhibited relatively small grain sizes due to the addition of YSZ particles. For example, the average grain sizes of the Al_2O_3 matrix in AB-8Z and AB-16Z showed a submicron order even sintered at 1600 °C. As shown in Fig. 2.7(b), as the sintering temperature increased, the length in long-axis direction of the Ba-β-Al_2O_3 phase was almost unchanged, while its aspect ratio showed a similar downtrend in all the samples.

Fig. 2.8 shows the TEM images of AB-8Z sample sintered at 1600 °C. The added YSZ and reaction-formed ZrO_2 particles were distributed in the Al_2O_3 matrix (Fig. 2.8(a)). It was found from the EDS analyses that there existed Y_2O_3 in both YSZ and ZrO_2 particles (Table 2.2), but the Y_2O_3 content in the reaction-formed ZrO_2 particle was lower than that in YSZ. This indicates that the migration and diffusion of some Y^{3+} definitely occur from YSZ to reaction-formed ZrO_2 during sintering process, giving rise to the stabilization of *m*-ZrO_2 and increase of *t*-ZrO_2 phase. As can be seen from Fig. 2.8(a)-(c), the reaction-formed ZrO_2 exhibited a band structure. This might be the result of twinning during $t \rightarrow m$ martensitic transformation. Although the added YSZ particles are stable, the reaction-formed ZrO_2 particles have transformed from tetragonal to monoclinic phase due to their larger particle sizes and lower Y^{3+} contents (Table 2.2). The formation of twins provides an effective way of accommodating excessive stresses [28,29]. Moreover, as shown in Fig. 2.8(d), considerable dislocations were observed within the Ba-β-Al_2O_3 phase, and some small ZrO_2 particles were embedded in the Ba-β-Al_2O_3 phase.

2.3.3 Mechanical properties

The Vickers hardness and flexural strength of the in-situ synthesized samples sintered at different temperatures are shown in Fig. 2.9. Both the Vickers hardness and flexural strength were enhanced with increasing sintering temperature for all the samples. The improvement of the hardness and strength at higher temperatures is mainly ascribed to the increase of density. The YSZ added samples showed higher hardness and strength values than those samples without YSZ addition (AB-2.5Z). The improved hardness and strength of the YSZ added samples are believed to result from density improvement, dispersion strengthening of the YSZ particles, and grain refinement of Al_2O_3 matrix due to the existence of the YSZ particles. In comparison with AB-2.5Z, a lower Ba-β-Al_2O_3 content in AB-8Z and AB-16Z is also beneficial to the hardness enhancement, because Ba-β-Al_2O_3 has a low hardness value. Nevertheless, AB-16Z sintered at 1600 °C exhibited a slightly lower hardness value than AB-8Z because YSZ has a lower hardness value than Al_2O_3.

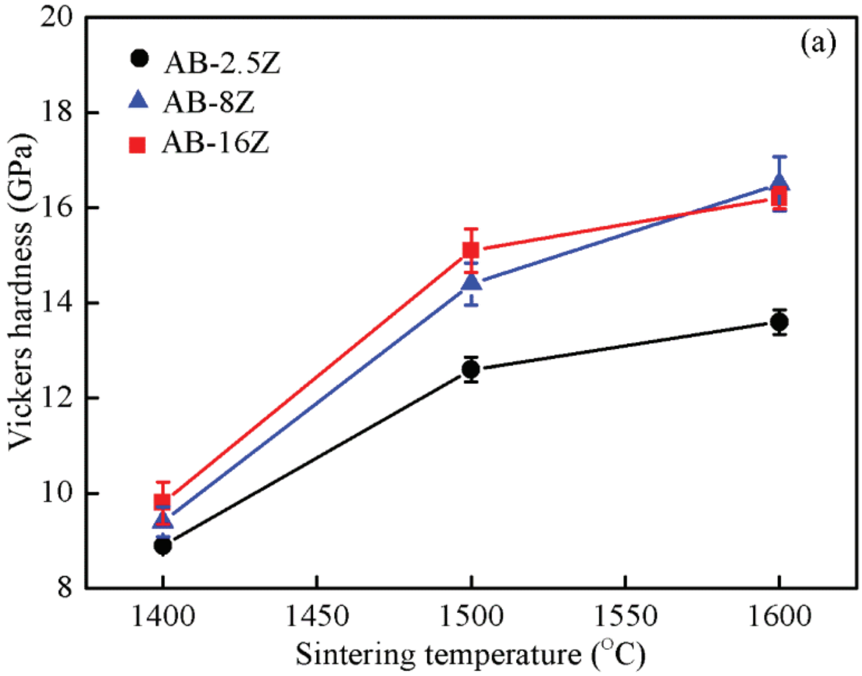

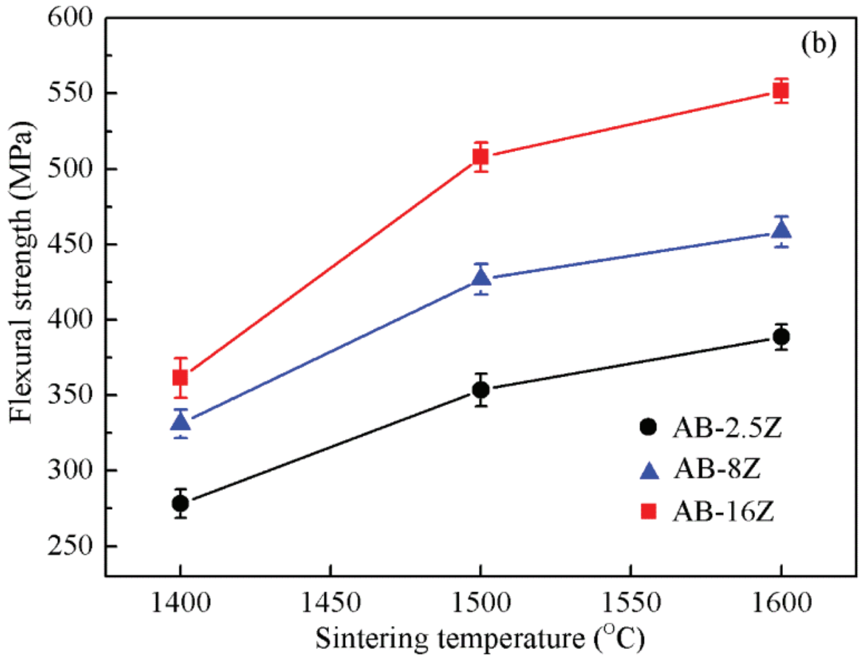

Fig. 2.9 (a) Vickers hardness and (b) flexural strength of in-situ synthesized samples sintered at different temperatures.

The fracture toughness of the in-situ synthesized samples is plotted in Fig. 2.10 as a function of sintering temperature. The fracture toughness of all the samples was enhanced with increasing sintering temperature except for Al_2O_3. The Al_2O_3 matrix composites showed higher fracture toughness than monolithic Al_2O_3. Furthermore, the addition of YSZ particles led to further improvements in fracture toughness of the composites. In the previous work [6,7], it has been demonstrated that the presence of Ba-β-Al_2O_3 phase with an elongated morphology in Al_2O_3 matrix composites causes toughness enhancement, as a result of crack deflection and crack bridging. In the Al_2O_3 matrix composites with YSZ addition, the improvements in fracture toughness are likely to be associated with martensitic transformation of ZrO_2 from tetragonal to monoclinic phase, in addition to the contribution of elongated Ba-β-Al_2O_3 phase. As mentioned above, the ZrO_2 phase is mainly present in *t*-ZrO_2 form in the composites with YSZ addition. Accordingly, the stresses generated during fracture may induce martensitic transformation of ZrO_2 from *t* to *m* phase.

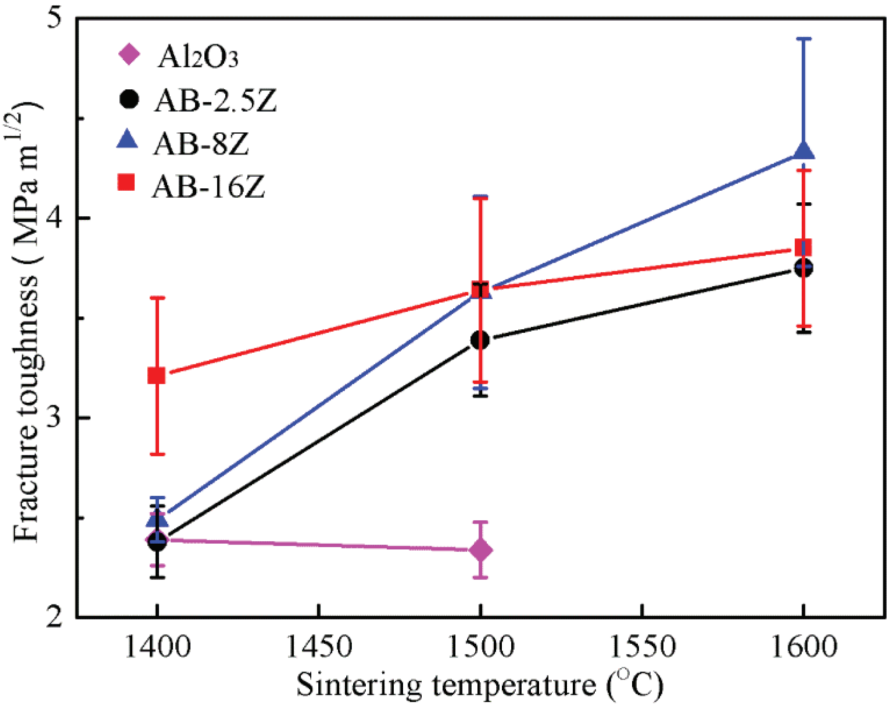

Fig. 2.10 Fracture toughness of in-situ synthesized samples as a function of sintering temperature.

Fig. 2.11 illustrates the transformation amount of ZrO_2 from *t* to *m* phase during fracture process, determined by XRD measurements. The results showed that the *t*→*m* phase transformation does occur during fracture process. Moreover, the volume fraction of transformed ZrO_2 increased with increasing sintering temperature, which is in agreement with the change tendency of fracture toughness (Fig. 2.10). The fracture toughness of Al_2O_3/Ba-β-Al_2O_3/ZrO_2 composites sintered at 1600 °C was enhanced from 3.8±0.3 to 4.3±0.6 MPa m$^{1/2}$. The transformability of the ZrO_2 phase was only 4.9 vol%, but the increasing rate of fracture toughness was 13.2%. The ZrO_2 in the composites includes 1.8 vol% reaction-formed ZrO_2 and 6.2 vol% added YSZ (Table 2.1). The toughness enhancement due to YSZ addition in the current work is comparable to the data reported by Tuan et al. [30]. They found that the fracture toughness of Al_2O_3/ZrO_2 composites sintered at 1600 °C was enhanced from 4.0 to 5.1 MPa $m^{1/2}$ by adding 7.5 vol% ZrO_2. The volume fraction of transformed ZrO_2 was 5 vol%, but the fracture toughness was raised by 27.5%.

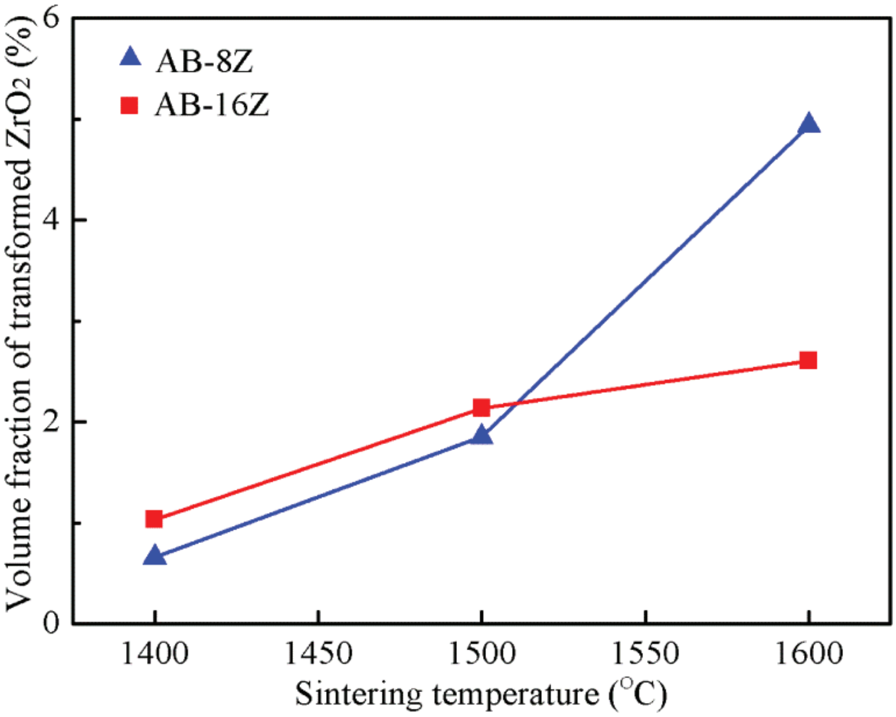

Fig. 2.11 Volume fraction of transformed ZrO_2 as a function of sintering temperature.

As stated above, the flexural strength was enhanced with increasing YSZ content. As for fracture toughness, however, although the experimental data are somewhat scattered, AB-16Z with a higher YSZ content exhibited a larger fracture toughness than AB-8Z at 1400 °C, whereas an opposite result was obtained at 1600 °C. This is associated with the phase transformation of ZrO_2. When reactive sintering is performed at a higher temperature, *e.g.*, 1600 °C, more Y^{3+} diffuses from the added YSZ particles into the Al_2O_3 matrix and reaction-formed ZrO_2, leading to the formation of more *t*-ZrO_2 (Fig. 2.3). As shown in Fig. 2.11, however, AB-16Z showed a lower amount of $t \rightarrow m$ transformation than AB-8Z at 1600 °C. Combined with the TEM results, it seems reasonable to consider that the added YSZ particles may be too stable to undergo stress-induced phase transformation and $t \rightarrow m$ transformation occurring during fracture process is mainly originated from the reaction-formed ZrO_2. A larger contribution of martensitic transformation toughening in AB-8Z sintered at 1600 °C results in its higher fracture toughness compared to AB-16Z. As reported by Tuan et al. [30], the volume fraction of transformed ZrO_2 in Al_2O_3/ZrO_2 composites sintered at 1600 °C was only 5 vol% by incorporating 7.5 vol% ZrO_2 (ZrO_2-3 mol% Y_2O_3 powder with d_{50}=0.24 μm). Furthermore, it has been demonstrated that the transformation-induced toughening decreases with decreasing the grain size of YSZ [31]. Accordingly, it seems that smaller particle size (50 nm) of the YSZ powder used in the current experiment is responsible for the high stability of the added YSZ particles. Further investigation is necessary to understand the effects of YSZ size and content on phase transformation of ZrO_2 and transformation toughening. Moreover, some reaction-formed ZrO_2 particles with smaller sizes may lose $t \rightarrow m$ phase transformation when a large amount of YSZ particles is added into Al_2O_3 matrix. This is because more Y^{3+} can diffuse from the added YSZ particles into reaction-formed ZrO_2, resulting in lower $t \rightarrow m$ phase transformation. Additionally, the effects of the residual stress related to the coefficient of thermal expansion (CTE) mismatch between Al_2O_3 and ZrO_2 have to be taken into consideration. The CTE values of Al_2O_3 and YSZ in the temperature range of 25-1000 °C are 8.1×10^{-6} °C^{-1} and 10.3×10^{-6} °C^{-1}, respectively [32]. Thus, when the sintered samples are cooled down from the sintering temperature, the Al_2O_3 grains in the vicinity of ZrO_2 particles are subjected to compressive stress, while residual tensile stress is accumulated in ZrO_2, which may promote occurrence of the phase transformation of ZrO_2 [33].

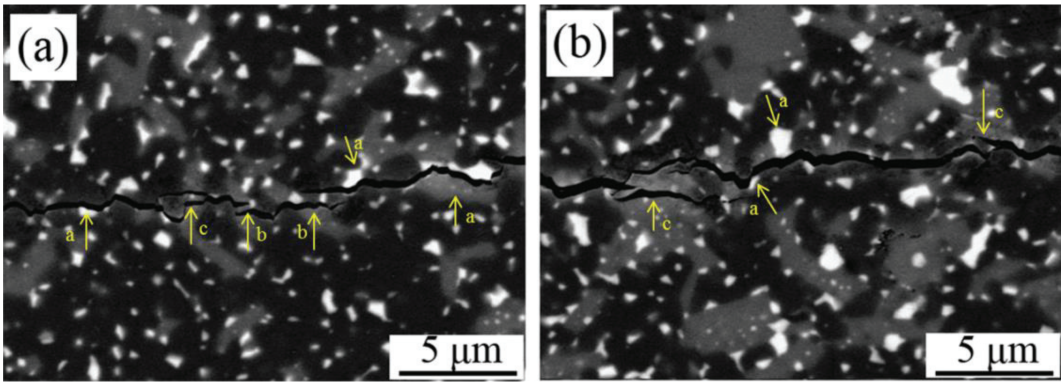

Fig. 2.12 SEM images showing crack propagation behavior in AB-8Z sample sintered at 1600 °C.

The propagation behavior of cracks introduced by a Vickers indenter in AB-8Z sample sintered at 1600 °C is shown in Fig. 2.12. Crack deflection caused by Ba-β-Al_2O_3 phase and ZrO_2 particles (indicated by arrows “a”) was observed, where the main cracks propagated along the interfaces between Al_2O_3 matrix and Ba-β-Al_2O_3 phase or ZrO_2 particles. Although the added YSZ particles have lower stress-induced phase transformability, it could toughen the composites by crack deflection. Crack bridging (arrows “b”) and crack branching (arrows “c”) could also be observed. The fracture surface of AB-8Z sample with 6.2 vol% YSZ addition after four-point bending test is shown in Fig. 2.13. The fracture mode was a mixture of intergranular and transgranular fracture due to the existence of the elongated Ba-β-Al_2O_3 phase.

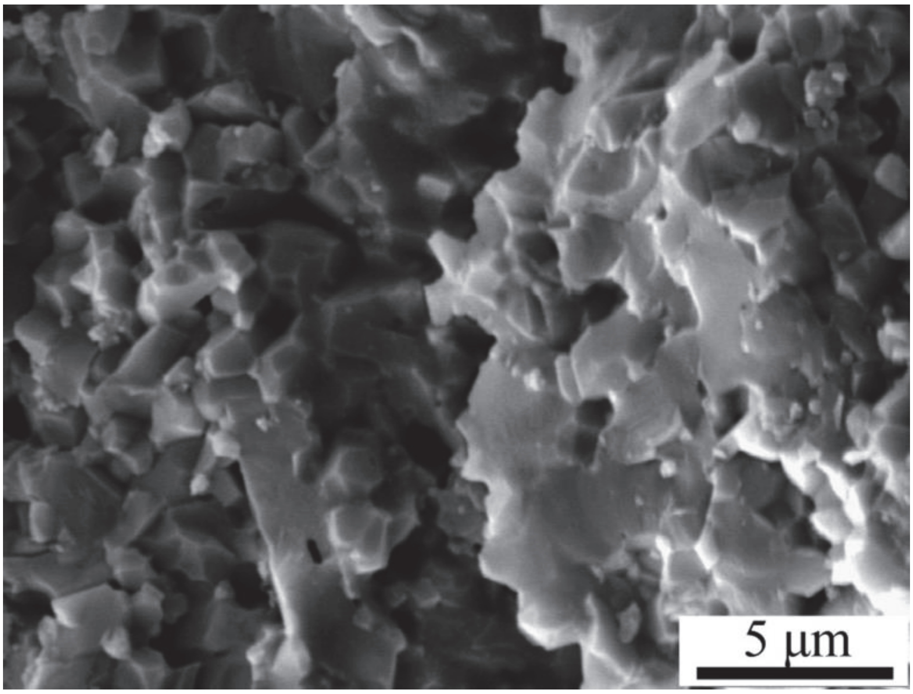

Fig. 2.13 SEM image (secondary electron mode) of the fracture surface of AB-8Z sample sintered at 1600 °C after four-point bending test.

According to the above results, the toughening mechanisms of the in-situ synthesized Al_2O_3 matrix composites with YSZ addition include the following two aspects: (i) the transformation toughening of ZrO_2 formed by the reactions inhibits crack growing and propagating; (ii) crack deflection, crack bridging, and crack branching resulting from both Ba-β-Al_2O_3 phase and ZrO_2 particles can absorb plentiful fracture energy and hinder further propagation of the cracks in the matrix, which plays an important role in enhancement of fracture toughness [34-36].

Larger fracture toughness values at room temperature imply that it is effective to inhibit crack growing and propagating, which is favorable to the improvement of thermal shock resistance of the composites [37,38]. Nevertheless, the CTE mismatch between Al_2O_3 and ZrO_2, and higher density may lead to more microcracks in YSZ added samples. Consequently, thermal shock resistance is another important factor to be considered. During cooling of samples from 1100 °C to room temperature, some microcracks emerged inevitably. The resistance to crack propagation during thermal cycling is the main concern, rather than the resistance to crack initiation [37]. Fig. 2.14 shows the SEM image of AB-8Z sample after thermal shock cycling. The initial microcracks are considered to be preferentially generated along the boundaries between Al_2O_3 and ZrO_2. These microcracks are arrested after a short propagation when contacting with Ba-β-Al_2O_3 (pointed by the arrows). This is mainly attributed to the toughening effects of Ba-β-Al_2O_3 phase.

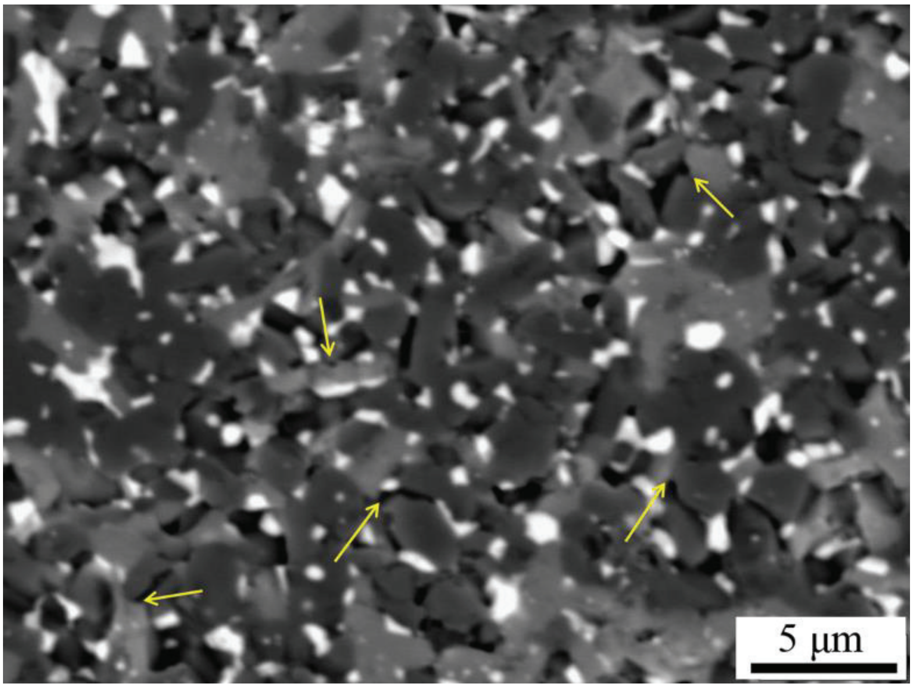

Fig. 2.14 SEM image of AB-8Z sample after thermal shock cycling.

Based on the above results, it can be concluded that the addition of YSZ enhanced the mechanical properties including the Vickers hardness, flexural strength, and fracture toughness of Al_2O_3/Ba-β-Al_2O_3/ZrO_2 composites in comparison with Al_2O_3/Ba-β-Al_2O_3/*m*-ZrO_2 composites without YSZ addition. For example, the

AB-8Z composite with 6.2 vol% YSZ addition showed the fracture toughness of 4.3±0.6 MPa $m^{1/2}$, Vickers hardness of 16.5±0.6 GPa, and flexural strength of 458±9.9 MPa. Compared to ZTA/$SrAl_{12}O_{19}$, ZTA/$LaAl_{11}O_{18}$, and ZTA/$CaAl_{12}O_{19}$ composites reported in the literature [16-18], the Al_2O_3/Ba-β-Al_2O_3/ZrO_2 composites showed comparable Vickers hardness and flexural strength, but the facture toughness was relatively lower, which is ascribed to the low phase transformability of the added YSZ particles. Thus, 1.5YSZ and 2YSZ with lower Y_2O_3 contents are considered to be incorporated into the composites and further improve the mechanical properties in chapter 2.

2.4 Conclusions

Al_2O_3/Ba-β-Al_2O_3/ZrO_2 composites were fabricated by solid-state reaction sintering, and the effects of YSZ addition on microstructure and mechanical properties were investigated. Based on the above experimental results, the following conclusions can be drawn:

(1) The incorporation of YSZ promoted the densification of the Al_2O_3 matrix composites and formation of tetragonal ZrO_2 phase. The ZrO_2 phase (1.8 vol%) formed by the reactions between Al_2O_3 and $BaZrO_3$ was stabilized due to the diffusion of Y^{3+} from nearby YSZ particles.

(2) The microstructure of the composites was characterized by elongated Ba-β-Al_2O_3 phase and equiaxed ZrO_2 particles including added YSZ and reaction-formed ZrO_2. Most fine and homogeneously distributed ZrO_2 particles in the composites were

located at the grain boundaries, effectively suppressing the grain growth of Al_2O_3 matrix.

(3) The in-situ synthesized Al_2O_3 matrix composites exhibited improved fracture toughness as well as high Vickers hardness and flexural strength. For example, the composite with 6.2 vol% YSZ addition showed the fracture toughness of 4.3±0.6 MPa $m^{1/2}$, Vickers hardness of 16.5±0.6 GPa, and flexural strength of 458±9.9 MPa. In comparison with Al_2O_3/Ba-β-Al_2O_3/*m*-ZrO_2 composites without YSZ addition, the Al_2O_3/Ba-β-Al_2O_3/ZrO_2 composites exhibited higher Vickers hardness and flexural strength, which are mainly ascribed to dispersion strengthening of the added YSZ particles and grain refinement of Al_2O_3 matrix.

(4) The addition of YSZ led to enhancement of fracture toughness of the in-situ synthesized Al_2O_3 matrix composites as a result of multiple toughening effects including crack deflection, crack bridging, crack branching, and martensitic transformation of ZrO_2. The added YSZ particles seem to be too stable to undergo stress-induced phase transformation and martensitic transformation is mainly originated from the reaction-formed ZrO_2.

References

1. D. Asmi, I.M. Low, Self-reinforced Ca-hexaluminate/alumina composites with graded microstructures, Ceram. Int. 34 (2008) 311–316.
2. L. An, H.M. Chan, R-curve behavior of in-situ-toughened Al_2O_3: $CaAl_{12}O_{19}$ ceramic composites, J. Am. Ceram. Soc. 79 (1996) 3142–3148.
3. D. Asmi, I.M. Low, Processing of an in-situ layered and graded alumina/calcium-hexaluminate composite: physical characteristics, J. Eur. Ceram. Soc. 18 (1998) 2019–2024.
4. K. Vishista, F.D. Gnanam, Microstructural development of $SrAl_{12}O_{19}$ in alumina-strontia composites, J. Eur. Ceram. Soc. 29 (2009) 77–83.
5. K. Vishista, F.D. Gnanam, Effect of strontia on the densification and mechanical properties of sol-gel alumina, Ceram. Int. 32 (2006) 917–922.
6. Z.C. Chen, K.K. Chawla, M. Koopman, Microstructure and mechanical properties of in situ synthesized alumina/Ba-β-alumina/zirconia composites, Mater. Sci. Eng. A 367 (2004) 24–32.
7. Z.C. Chen, S. Nugroho, M. Ezumi, T. Akao, T. Onda, In situ synthesis of alumina-matrix oxide/oxide composites by reactive sintering, Mater. Sci. Eng. A 557 (2012) 59–68.
8. M. Yasuoka, K. Hirao, M.E. Brito, S. Kanzaki, High-strength and high-fracture-toughness ceramics in the $Al_2O_3/LaAl_{11}O_{18}$ systems, J. Am. Ceram. Soc. 78 (1995) 1853–1856.
9. Z. Negahdari, M. Willert-Porada, Tailoring the microstructure of reaction-sintered

alumina/lanthanum hexaaluminate particulate composites, J. Eur. Ceram. Soc. 30 (2010) 1381–1389.

10. H. Tang, M.H. Fang, X. Min, X.J. Wang, Z.H. Huang, R.L. Wen, Y.A. Liu, X.W. Wu, Mechanical properties and solid particle erosion behavior of $LaMgAl_{11}O_{19}$-Al_2O_3 ceramic at room and elevated temperatures, J. Am. Ceram. Soc. 99 (2016) 2138–2146.
11. H. Tang, M.H. Fang, C. Tang, Z.H. Huang, H.T. Liu, H.K. Zhu, Y.A. Liu, X.W. Wu, Effect of $LaMgAl_{11}O_{19}$ addition and temperature on the mechanical properties of Al_2O_3-based ceramics, Mater. Sci. Eng. A 655 (2016) 160–167.
12. K.Y. Fan, J.Y. Pastor, J. Ruiz-Hervias, J. Gurauskis, C. Baudin, Determination of mechanical properties of Al_2O_3/Y-TZP ceramic composites: Influence of testing method and residual stresses, Ceram. Int. 42 (2016) 18700–18710.
13. J. Chen, Z.P. Xie, W.N. Zeng, W.W. Wu, Toughening mechanisms of ZTA ceramics at cryogenic temperature (77 K), Ceram. Int. 43 (2017) 3970–3974.
14. C. Exare, J.M. Kiat, N. Guiblin, F. Porcher, V. Petricek, Structural evolution of ZTA composites during synthesis and processing, J. Eur. Ceram. Soc. 35 (2015) 1273–1283.
15. X.Q. Xu, X.X. Hu, S. Ren, H.T. Geng, H.Y. Du, J.C. Liu, Fine grained Al_2O_3-ZrO_2 (Y_2O_3) ceramics by controlled crystallization of amorphous phase, J. Eur. Ceram. Soc. 36 (2016) 1791–1796.
16. R.A. Cutler, R.J. Mayhew, K.M. Prettyman, A.V. Virkar, High-toughness Ce-TZP/Al_2O_3 ceramics with improved hardness and strength, J. Am. Ceram. Soc.

74 (1991) 179–186.

17. R. Guo, D. Guo, Y. Chen, Z. Yang, Q. Yuan, In situ formation of $LaAl_{11}O_{18}$ rodlike particles in ZTA ceramics and effect on the mechanical properties, Ceram. Int. 28 (2002) 699–704.
18. Z.D.I. Sktani, A.Z.A. Azhar, M.M. Ratnam, Z.A. Ahmad, The influence of in-situ formation of hibonite on the properties of zirconia toughened alumina (ZTA) composites, Ceram. Int. 40 (2014) 6211–6217.
19. W. Burger, H.G. Richter, High strength and toughness alumina matrix composites by transformation toughening and “in situ” platelet reinforcement (ZPTA)–the new generation of bioceramics, Key Eng. Mater. 192-195 (2001) 545–548.
20. R.C. Garvie, P.S. Nicholson, Phase analysis in zirconia systems, J. Am. Ceram. Soc. 55 (1972) 303–305.
21. A.G. Evans, E.A. Charles, Fracture toughness determinations by indentation, J. Am. Ceram. Soc. 59 (1976) 371–372.
22. Y.P. Ye, J.G. Li, H.D. Zhou, J.M. Chen, Microstructure and mechanical properties of yttria-stabilized ZrO_2/Al_2O_3 nanocomposite ceramics, Ceram. Int. 34 (2008) 1797–1803.
23. F.C. Meng, C. Liu, F. Zhang, Z.Q. Tian, W.J. Huang, Densification and mechanical properties of fine-grained Al_2O_3–ZrO_2 composites consolidated by spark plasma sintering, J. Alloys Compd. 512 (2012) 63–67.
24. W.M. Ma, L. Wen, R.G. Guan, X.D. Sun, X.K. Li, Sintering densification, microstructure and transformation behavior of $Al_2O_3/ZrO_2(Y_2O_3)$ composites,

Mater. Sci. Eng. A 477 (2008) 100–106.

25. Y. Moriyoshi, Y. Chida, T. Ikegami, H. Yamamura, A. Watanabe, Microstructure in Al_2O_3-ZrO_2 ceramics, in: S. Sōmiya, (Ed.), Zirconia ceramics, Uchida Rokakuho Publishing Co., Ltd., Tokyo, 1983, pp. 97–108.
26. C. Domínguez, J. Chevalier, R. Torrecillas, G. Fantozzi, Microstructure development in calcium hexaluminate, J. Eur. Ceram. Soc. 21 (2001) 381–387.
27. C. Domínguez, J. Chevalier, R. Torrecillas, L. Gremillard, G. Fantozzi, Thermomechanical properties and fracture mechanisms of calcium hexaluminate, J. Eur. Ceram. Soc. 21 (2001) 907–917.
28. P.M. Kelly, C.J. Ball, Crystallography of stress-induced martensitic transformations in partially stabilized zirconia, J. Am. Ceram. Soc. 69 (1986) 259–264.
29. J.A. Krogstad, R.M. Leckie, S. Krämer, J.M. Cairney, D.M. Lipkin, C.A. Johnson, C.G. Levi, Phase evolution upon aging of air plasma sprayed *t′*-zirconia coatings: II-microstructure evolution, J. Am. Ceram. Soc. 96 (2013) 299–307.
30. W.H. Tuan, R.Z. Chen, T.C. Wang, C.H. Cheng, P.S. Kuo, Mechanical properties of Al_2O_3/ZrO_2 composites, J. Eur. Ceram. Soc. 22 (2002) 2827–2833.
31. J. Eichler, J. Rodel, U. Eisele, M. Hoffman, Effect of grain size on mechanical properties of submicrometer 3Y-TZP: Fracture strength and hydrothermal degradation, J. Am. Ceram. Soc. 90 (2007) 2830–2836.
32. A.Z.A. Azhar, M.M. Ratnam, Z.A. Ahmad, Effect of Al_2O_3/YSZ microstructures on wear and mechanical properties of cutting inserts, J. Alloys Compd. 478 (2009)

608–614.

33. A. Smirnov, J.I. Beltrán, T. Rodriguez-Suarez, C. Pecharromán, M.C. Muñoz, J.S. Moya, J.F. Bartolomé, Unprecedented simultaneous enhancement in damage tolerance and fatigue resistance of zirconia/Ta composites, Sci. Rep. 7 (2017) 44922.
34. Z.Y. Deng, Y. Zhou, M.E. Brito, J.F. Yang, T. Ohji, Fracture-mode change in alumina-silicon carbide composites doped with rare-earth impurities, J. Am. Ceram. Soc. 86 (2003) 1789–1792.
35. Z.Y. Deng, Y. Zhou, M.E. Brito, Y. Tanaka, T. Ohji, Effects of rare earth dopants on grain boundary bonding in alumina–silicon carbide composites, J. Eur. Ceram. Soc. 24 (2004) 511–516.
36. G.D. West, J.M. Perkins, M.H. Lewis, The effect of rare earth dopants on grain boundary cohesion in alumina, J. Eur. Ceram. Soc. 27 (2007) 1913–1918.
37. L. Xu, M. Chen, L.Y. Jin, X.L. Yin, N. Wang, L. Liu, Effect of ZrO_2 addition on densification and mechanical properties of $MgAl_2O_4$-$CaAl_4O_7$-$CaAl_{12}O_{19}$ composite, J. Am. Ceram. Soc. 98 (2015) 4117–4123.
38. L. Liu, M. Chen, L. Xu, X.L. Yin, W.J. Sun, Effect of BaO addition on densification and mechanical properties of Al_2O_3-MgO-CaO refractories, Metals 6 (2016) 84.

Chapter 3: Effect of YSZ with different Y_2O_3 contents on toughening behavior of in-situ synthesized Al_2O_3/Ba-β-Al_2O_3/ZrO_2 composites

3.1 Introduction

The in-situ formation of reinforcements with elongated morphologies during sintering has attracted much attention in toughening Al_2O_3 matrix composites. So far, a lot of research work has been focused on synthesis of Al_2O_3 matrix composites containing elongated $CaAl_{12}O_{19}$, $SrAl_{12}O_{19}$, $LaAl_{11}O_{18}$, $LaMgAl_{11}O_{19}$, and Ba-β-Al_2O_3 phases by in-situ chemical reactions [1-9]. The fracture toughness enhancement of Al_2O_3/Ba-β-Al_2O_3/*m*-ZrO_2 composites is mainly ascribed to the presence of Ba-β-Al_2O_3 phase through crack deflection/bridging. In addition, the elongated Ba-β-Al_2O_3 phase also contributes to the enhancement of thermal shock resistance [10]. Nevertheless, the fracture toughness value of Al_2O_3/Ba-β-Al_2O_3/*m*-ZrO_2 composites is still relatively low (～3.8 MPa $m^{1/2}$). It has been demonstrated that the incorporation of small amounts of yttria-stabilized zirconia (YSZ) or Y_2O_3 promotes the phase transformation from *m*-ZrO_2 to *t*-ZrO_2 [11-13]. Therefore, the *m*-ZrO_2 formed through the reaction may be transformed into *t*-ZrO_2 by adding YSZ or Y_2O_3, thus resulting in enhancement in fracture toughness.

In chapter 2, we attempted to introduce transformation toughening mechanism in Al_2O_3/Ba-β-Al_2O_3/*m*-ZrO_2 composites by adding different amounts of 3YSZ to the powder mixtures of Al_2O_3 and $BaZrO_3$. However, the contribution of 3YSZ to toughness enhancement is still small. Furthermore, a further increase in 3YSZ content even resulted in a lower toughness value at 1600 °C. Thus, in this chapter, 1.5YSZ and 2YSZ with lower Y_2O_3 contents were incorporated into the powder mixtures of Al_2O_3 and $BaZrO_3$. In addition, Y_2O_3 was also used as an additive to compare its toughening effect.

In this chapter, Al_2O_3/Ba-β-Al_2O_3/ZrO_2 composites were fabricated by reactive sintering of Al_2O_3, $BaZrO_3$, and YSZ (Y_2O_3) powder mixtures. The aim was to investigate the influences of YSZ with different Y_2O_3 contents and Y_2O_3 additions on densification behavior, phase evolution, microstructure, and mechanical properties of Al_2O_3/Ba-β-Al_2O_3/ZrO_2 composites.

3.2 Experimental procedure

Al_2O_3 (99.99% purity, Taimei Chemicals), $BaZrO_3$ (99%, Kojundo Chemical Lab.), 3 mol% Y_2O_3-ZrO_2 (3YSZ, 99.9%, Tosoh), 2 mol% Y_2O_3-ZrO_2 (2YSZ, 99.9%, Tosoh), 1.5 mol% Y_2O_3-ZrO_2 (1.5YSZ, 99.8%, Daiichi Kigenso Kagaku Kogyo), and Y_2O_3 (99.9%, Shin-Etsu Chemical) powders were used as the starting materials. The mean particle sizes of Al_2O_3, $BaZrO_3$, 3YSZ, 2YSZ, 1.5YSZ, and Y_2O_3 powders were 0.16 μm, 1.5 μm, 50 nm, 50 nm, 0.7 μm, and 1 μm, respectively. 1.5YSZ, 2YSZ, and 3YSZ powders were added to the powder mixtures of Al_2O_3 and $BaZrO_3$ to synthesize Al_2O_3/Ba-β-Al_2O_3/ZrO_2 composites. For comparison, some composite samples were also prepared by adding 0.5 wt% Y_2O_3, and the nominal compositions were summarized in Table 3.1.

The raw powders were ball-milled for 24 h in ethanol with Al_2O_3 balls as milling media. After drying at 120 °C for 24 h, the powder mixtures were uniaxially pressed to pellets (*Φ*19 mm×3 mm) under 20 MPa, followed by cold isostatic pressing under 200 MPa. The resulting pellets were sintered at 1400, 1500, and 1600 °C for 2 h in air, and the heating/cooling rates were 400 °C/h.

Table 3.1 Nominal compositions of Al_2O_3/Ba-β-Al_2O_3/ZrO_2 composites (vol%).

Samples	Al_2O_3	Ba-β-Al_2O_3	ZrO_2	YSZ	Y_2O_3
AB-2.5Z	70	27.5	2.5	0	0
AB-10Z(1.5/2/3Y)	62.5	27.5	2.5	7.5	0
AB-2.5Z(Y)	70	27.5	2.5	0	0.5 wt%

The density of the sintered samples was measured in distilled water based on the Archimedes' principle. Phase identification was performed by X-ray diffraction (XRD; RINT-TTR III, Rigaku, Japan) using Cu Kα radiation. The volume fraction of monoclinic ZrO_2 phase (V_m) was calculated by the modified equation proposed by Garvie and Nicholson [14]. Scanning electron microscopy (SEM; JXA-9800RL, JEOL, Japan) and electron probe micro-analyzer (EPMA; JXA-9800RL, JEOL) were used to characterize the microstructure and element distributions, respectively. In addition, the microstructure was also analyzed by transmission electron microscopy (TEM; JEM-2010, JEOL), and elemental analysis was carried out by the TEM equipped with an energy-dispersive X-ray spectroscopy (EDS). The polished samples were heated at 1300 °C for 30 min to reveal the grain boundaries and measure the grain size of the Al_2O_3 matrix, and the aspect ratio of the Ba-β-Al_2O_3 phase was calculated by measuring the length and width.

The flexural strength was measured by four-point bending tests on rectangular bars with dimensions of 3 mm × 4 mm × 36 mm. The upper and lower spans were 10 and 30 mm, respectively, and the crosshead speed was 0.5 mm/min. Moreover, the Vickers hardness and fracture toughness were determined by an indentation method with a load of 98 N and a dwell time of 15 s, and the toughness was calculated by the equation proposed by Evans and Charles [15]. An average value of 10 tests was reported for each condition.

3.3 Results and discussion

3.3.1 Sintering behavior

Fig. 3.1 shows the variations of relative density with sintering temperature. The densification was promoted significantly at higher temperatures, and the YSZ-added samples exhibited higher relative density in comparison with AB-2.5Z sample. The densification enhancement of YSZ-added samples is mainly due to the following three reasons. (i) The diffusion coefficients of ions in ZrO_2 were much larger than those in Al_2O_3 [16]. (ii) The formation of solid solutions between Al_2O_3 and ZrO_2 leads to lattice defects [17]. (iii) The uniformly dispersed YSZ particles can effectively restrain the abnormal grain growth of Al_2O_3 matrix [18,19].

As shown in Fig. 3.1, the relative density of AB-10Z samples decreased with increasing Y_2O_3 content in YSZ, and AB-10Z(1.5Y) exhibited the largest density values at 1400 °C and 1500 °C. This results from the segregation of large Y^{3+} at the grain boundaries of Al_2O_3, which blocks the diffusion of ions along grain boundaries and results in reduced grain-boundary diffusivity and decreased densification rate [20]. Nevertheless, AB-2.5Z(Y) sample with 0.5 wt% Y_2O_3 addition presented higher relative density than AB-2.5Z sample. This is mainly attributed to the lower aspect ratio of the Ba-β-Al_2O_3 in AB-2.5Z(Y) sample, and it will be discussed later.

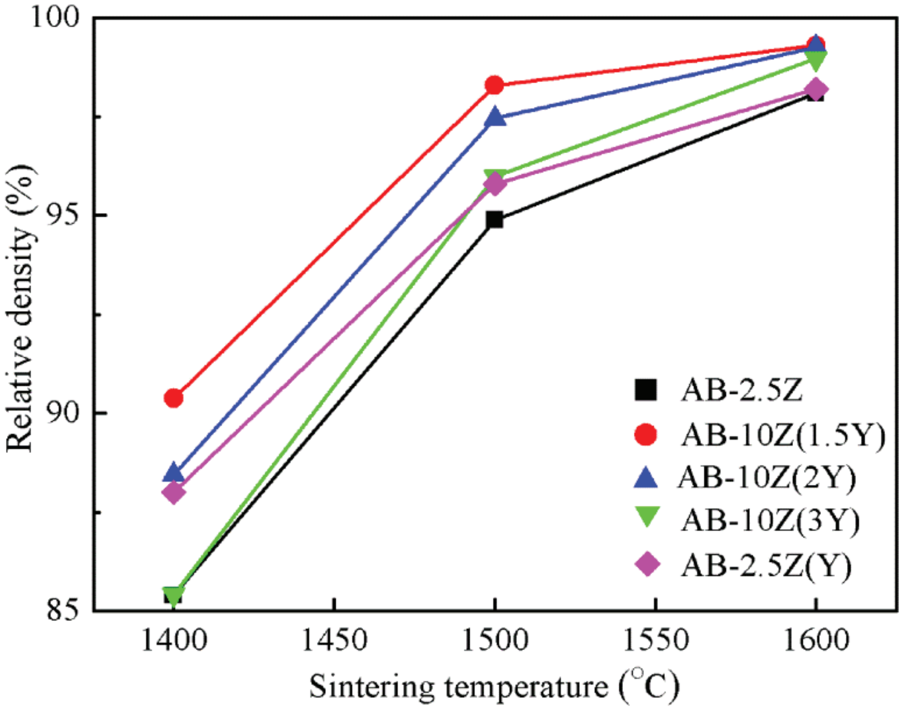

Fig. 3.1 Variations of relative density with sintering temperature.

3.3.2 Phase analysis and microstructure characterization

The XRD patterns of the sintered AB-10Z(2Y) and AB-2.5Z(Y) samples are shown in Fig. 3.2. At 1400-1600 °C, Al_2O_3, Ba-β-Al_2O_3, and ZrO_2 phases were found in both AB-10Z(2Y) and AB-2.5Z(Y) samples, while no peaks of $BaZrO_3$ or intermediate phases such as barium monoaluminate ($BaO\cdot Al_2O_3$), tri-barium monoaluminate ($3BaO\cdot Al_2O_3$), barium tetraaluminate ($BaO\cdot 4Al_2O_3$), barium hexaaluminate ($BaO\cdot 6Al_2O_3$) due to reactions between Al_2O_3 and $BaZrO_3$ were detected. The ZrO_2 phase existed in both *m*-ZrO_2 and *t*-ZrO_2 forms, and the *m*-ZrO_2 almost disappeared in AB-10Z(2Y) and AB-2.5Z(Y) samples sintered at 1600 °C.

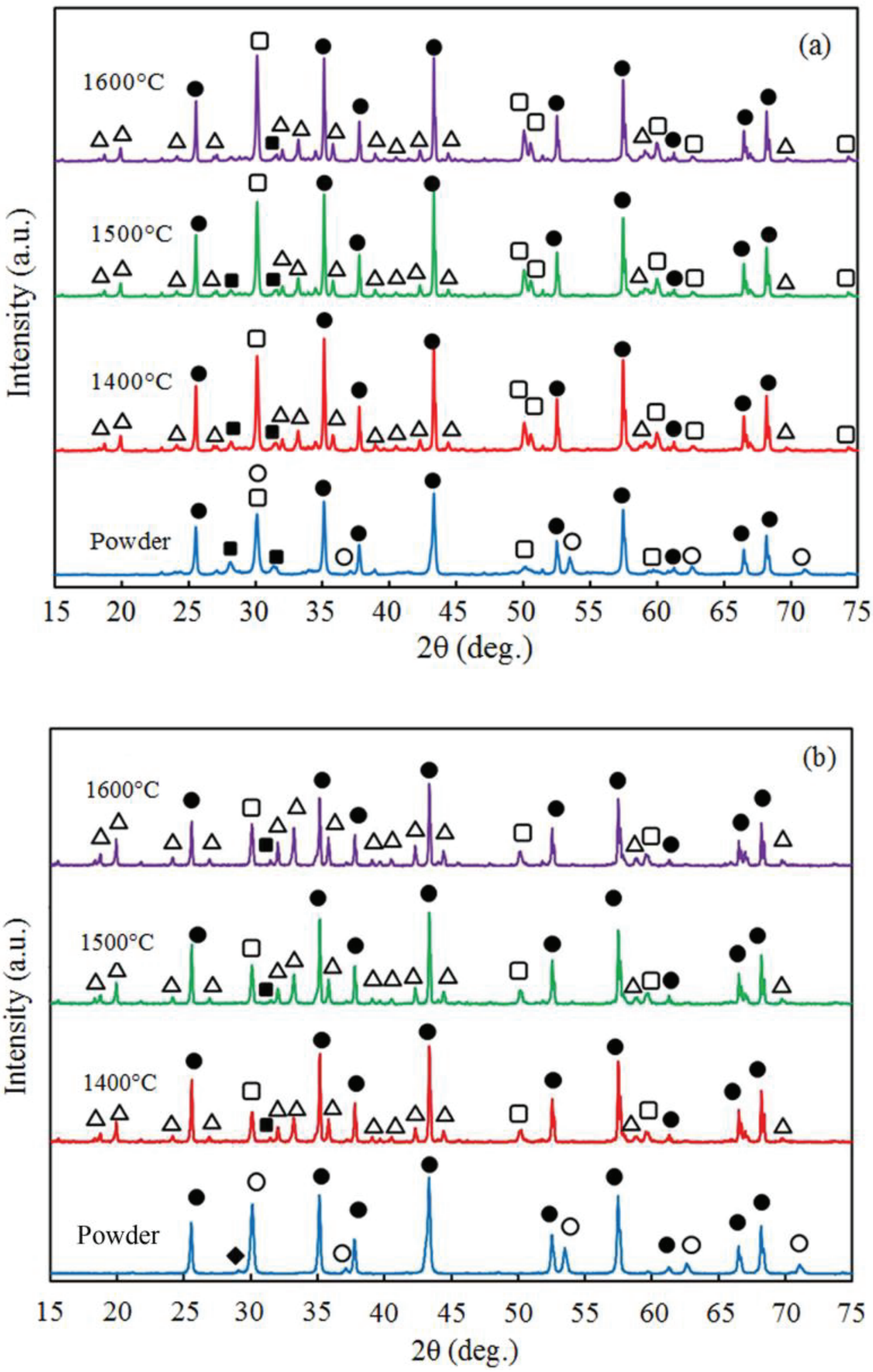

Fig. 3.2 XRD patterns of (a) AB-10Z(2Y) and (b) AB-2.5Z(Y) samples sintered at different temperatures. ● Al_2O_3, ○ $BaZrO_3$, △ Ba-β-Al_2O_3, □ *t*-ZrO_2, ■ *m*-ZrO_2, and ♦ Y_2O_3.

Fig. 3.3 shows the *m*-ZrO_2 phase content on the polished surfaces of AB-10Z and AB-2.5Z(Y) samples sintered at different temperatures. For AB-10Z samples, as the sintering temperature increased, the amount of *m*-ZrO_2 was gradually reduced, *i.e.*, more *t*-ZrO_2 was formed. This indicates that more Y^{3+} diffuses from YSZ particles into reaction-formed ZrO_2 at higher temperatures. Although similar *m*-ZrO_2 amounts were measured in AB-10Z(1.5Y) and AB-10Z(2Y) samples, the incorporation of higher Y_2O_3 content in YSZ (AB-10Z(3Y)) resulted in significant reductions of *m*-ZrO_2 amount. The Y_2O_3 content in AB-2.5Z(Y) was slightly lower than that in AB-10Z(3Y), but the former showed lower *m*-ZrO_2 amount than the latter due to the larger ZrO_2 amount in AB-10Z(3Y). In addition, no significant changes of *m*-ZrO_2 amount were found in AB-2.5Z(Y) sample with increasing temperature.

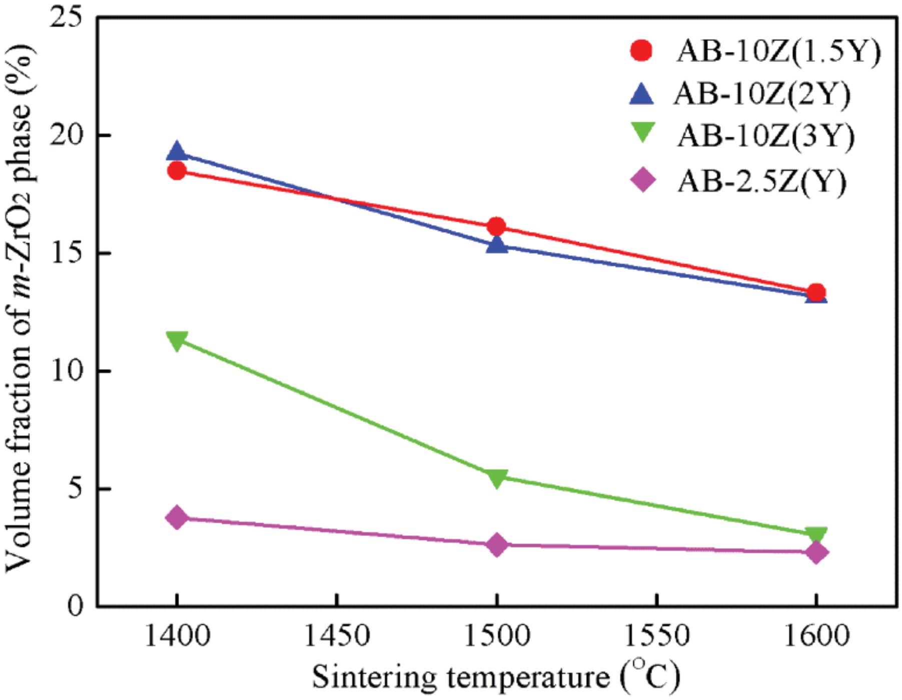

Fig. 3.3 Dependence of *m*-ZrO_2 phase content on sintering temperature.

The backscattered electron (BSE) images of the samples sintered at 1600 °C are shown in Fig. 3.4. Both white ZrO_2 particles and gray Ba-β-Al_2O_3 with a platelet morphology (pointed by the arrows in Fig. 3.4 (a)) were homogeneously distributed in the Al_2O_3 matrix with a dark contrast. For AB-2.5Z sample (Fig. 3.4 (a)), as mentioned before, all the ZrO_2 particles were formed through the reactions between Al_2O_3 and $BaZrO_3$ and existed in monoclinic phase. The added YSZ particles and reaction-formed ZrO_2 were included in YSZ-added samples (Fig. 3.4(b)-(d)), and the particle sizes of most reaction-formed ZrO_2 were larger than those of YSZ by comparing the images shown in Fig. 3.4. When 0.5 wt% Y_2O_3 was incorporated, although majority of ZrO_2 were present in *t*-ZrO_2 form, little difference in morphologies of ZrO_2 and Ba-β-Al_2O_3 was observed between AB-2.5Z and AB-2.5Z(Y) samples.

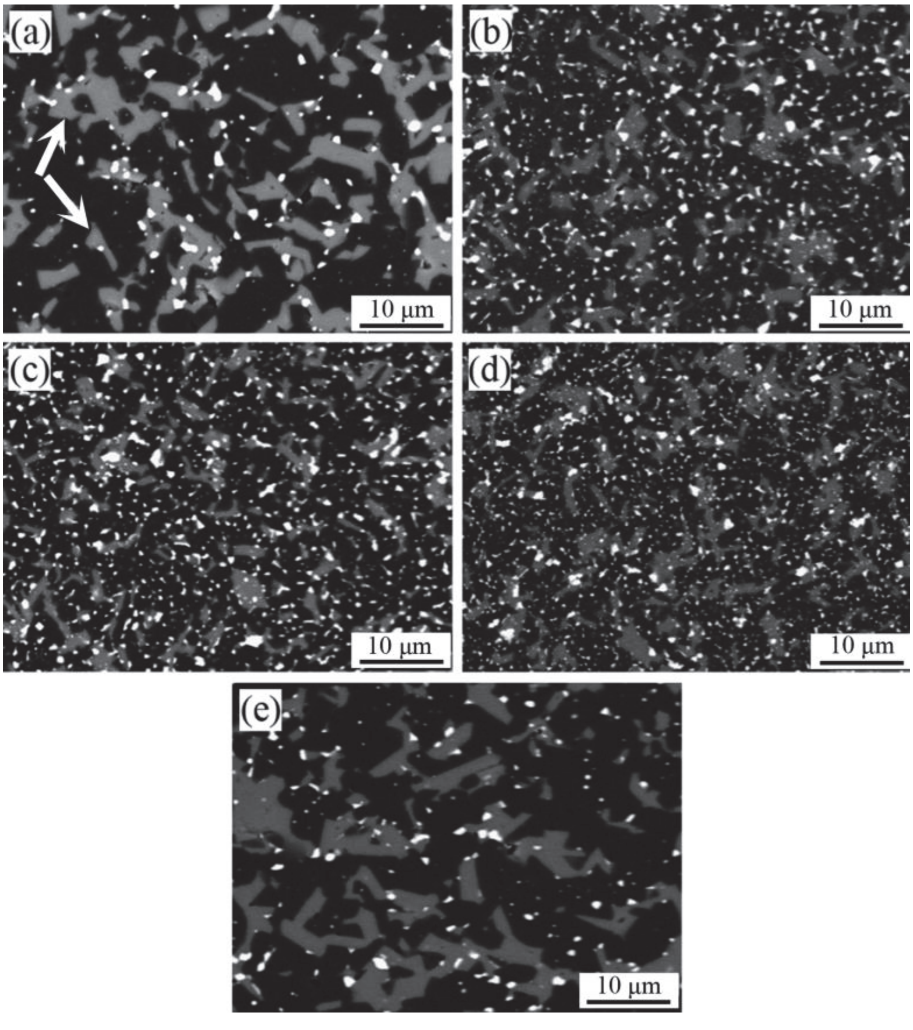

Fig. 3.4 Backscattered electron (BSE) images showing the microstructure of samples sintered at 1600 °C. (a) AB-2.5Z, (b) AB-10Z(1.5Y), (c) AB-10Z(2Y), (d) AB-10Z(3Y), and (e) AB-2.5Z(Y).

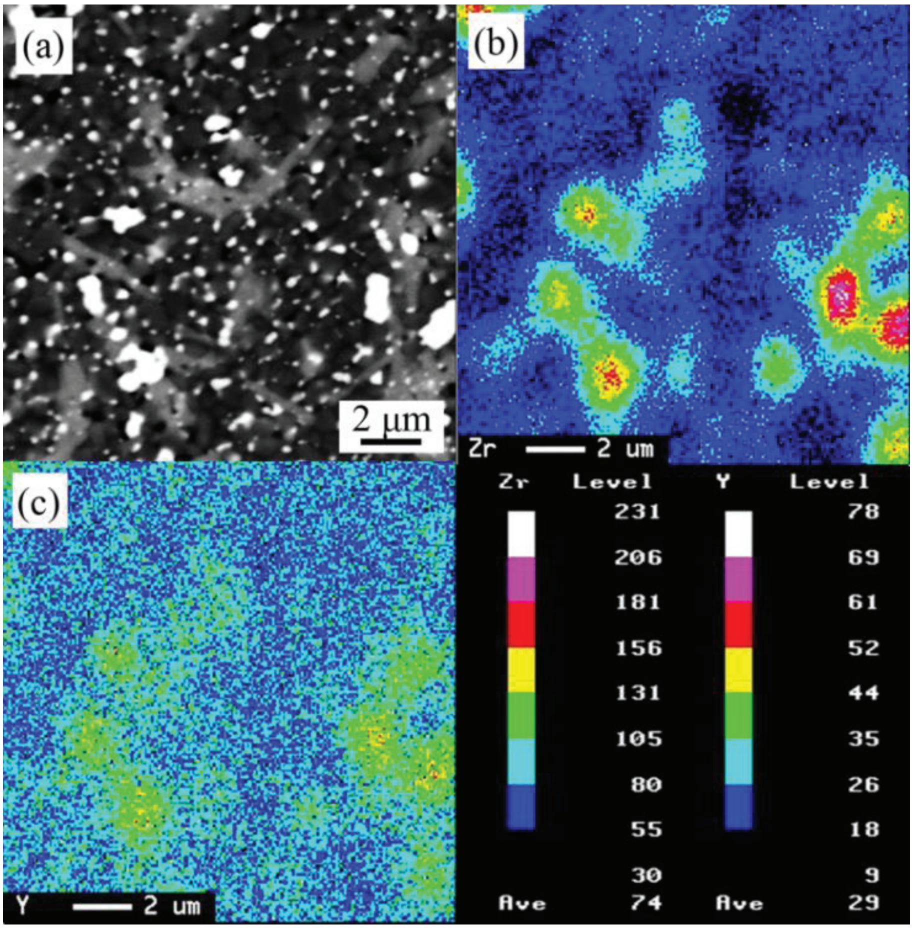

Fig. 3.5 EPMA analyses of AB-10Z(3Y) sample sintered at 1600 °C.

It can be seen from the EPMA analyses (Fig. 3.5) that some larger ZrO_2 particles exhibited higher amount of Y, indicating that Y^{3+} existed in YSZ particles has indeed migrated into reaction-formed ZrO_2. The BSE images of the thermally etched samples sintered at 1600 °C are shown in Fig. 3.6. Most added YSZ particles were located at the grain boundaries (Fig. 3.6 (b)-(d)) of the Al_2O_3 matrix, resulting in smaller Al_2O_3 grains in AB-10Z as compared to AB-2.5Z and AB-2.5Z(Y). Fig. 3.7 shows the average grain sizes in Al_2O_3/Ba-β-Al_2O_3/ZrO_2 composites. The average sizes of the Al_2O_3 grains and ZrO_2 particles increased gradually from 1400 to 1600 °C for all the samples. In comparison with AB-2.5Z and AB-2.5Z(Y), AB-10Z samples exhibited smaller grain sizes of Al_2O_3 due to inhibition effect of YSZ particles on movement of grain boundaries. The AB-10Z samples with a higher Y_2O_3 content showed smaller grain sizes of Al_2O_3, indicating that YSZ particles with a higher Y_2O_3 content have stronger inhibition effect on grain growth of the Al_2O_3 matrix. Although the solubility of Y_2O_3 in Al_2O_3 is extremely low, larger Y^{3+} (ionic radii of Al^{3+} and Y^{3+} are 0.053 and 0.089 nm, respectively) tends to segregate at the grain boundaries of Al_2O_3 and blocks the diffusion of ions along grain boundaries, resulting in reduced grain growth rates [20].

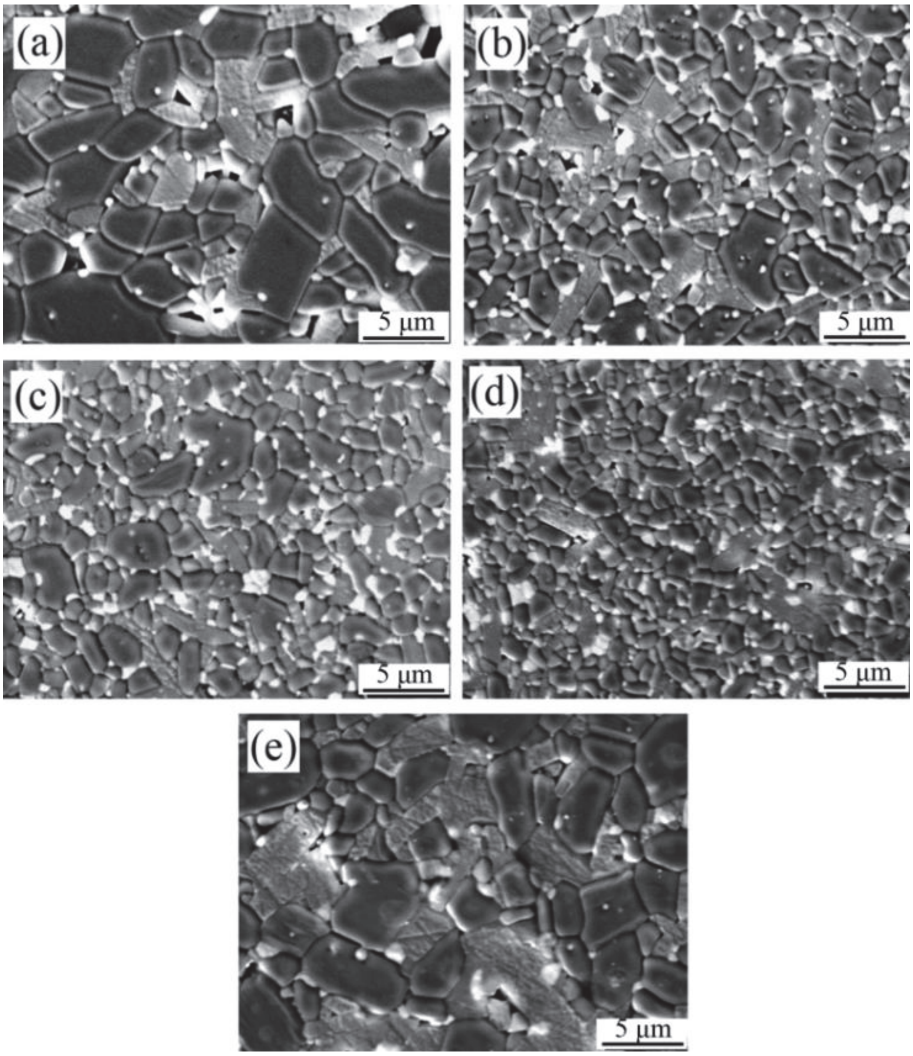

Fig. 3.6 BSE images showing the microstructure of thermally etched samples sintered at 1600 °C. (a) AB-2.5Z, (b) AB-10Z(1.5Y), (c) AB-10Z(2Y), (d) AB-10Z(3Y), and (e) AB-2.5Z(Y).

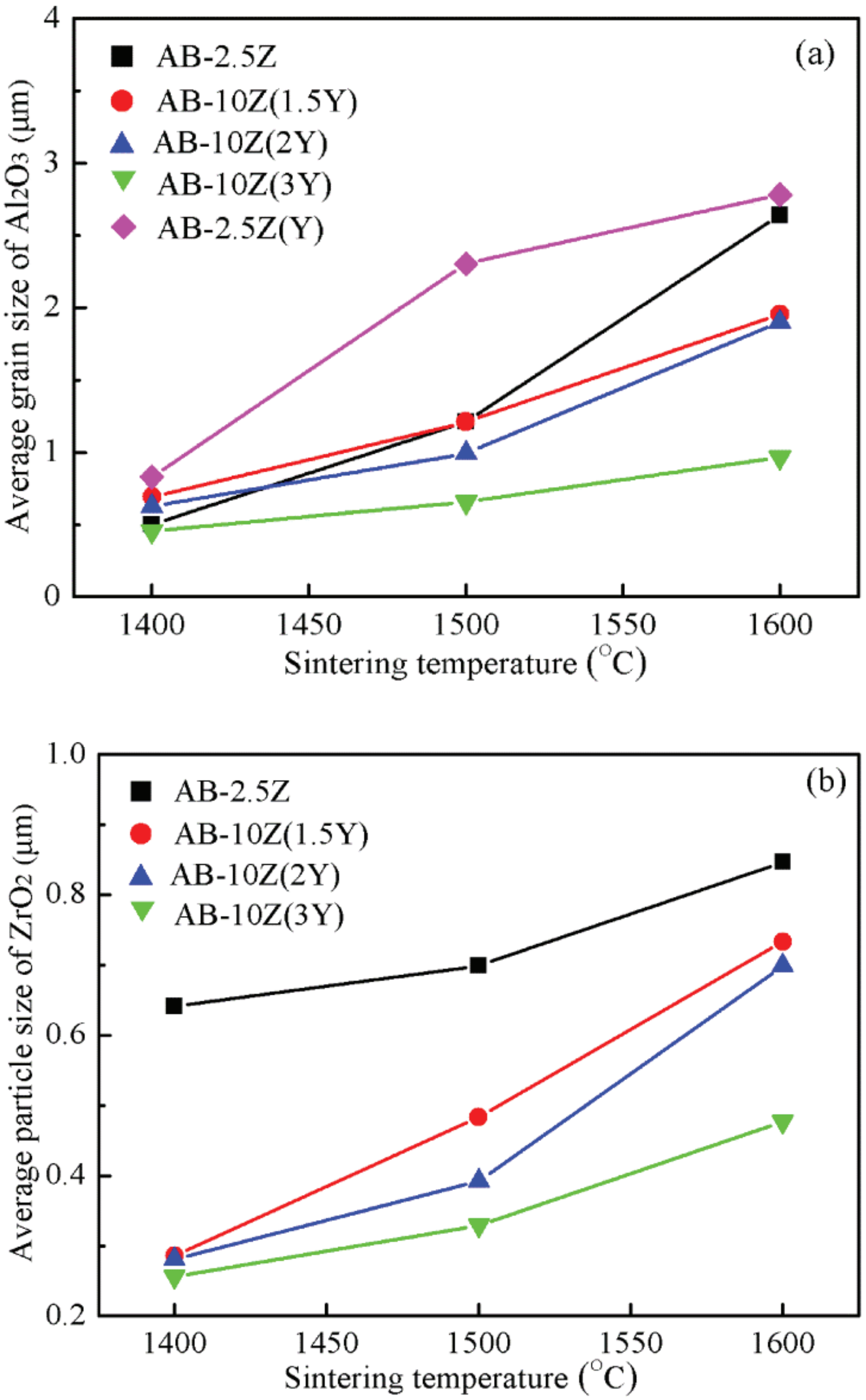
(a)
AB-2.5Z
AB-10Z(1.5Y)
AB-10Z(2Y)
AB-10Z(3Y)
AB-2.5Z(Y)
Average grain size of Al2O3 (μm)
0
1
2
3
4
1400
1450
1500
1550
1600
Sintering temperature (°C)
(b)
AB-2.5Z
AB-10Z(1.5Y)
AB-10Z(2Y)
AB-10Z(3Y)
Average particle size of ZrO2 (μm)
0.2
0.4
0.6
0.8
1.0
1400
1450
1500
1550
1600
Sintering temperature (°C)

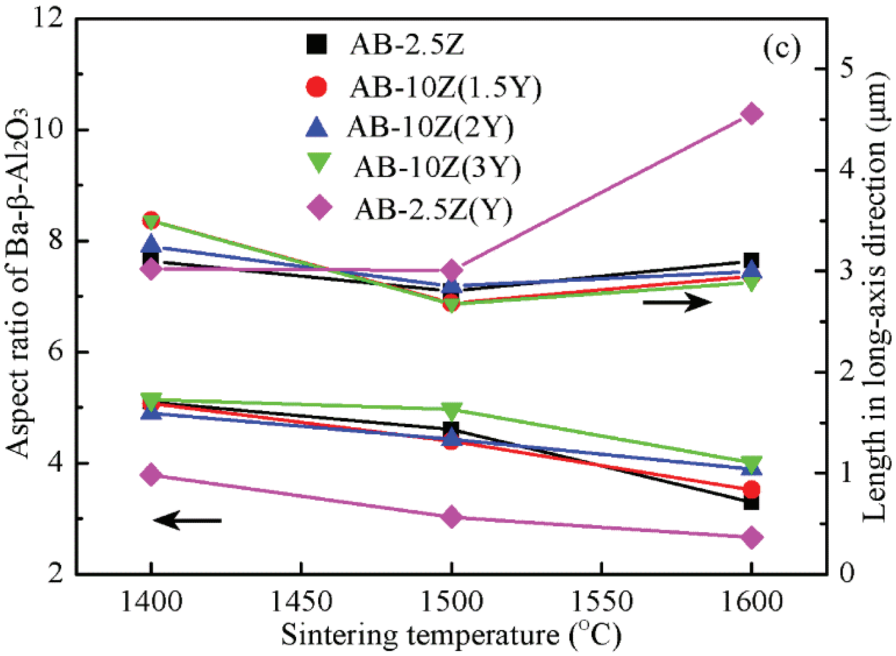

Fig. 3.7 Average sizes of (a) Al_2O_3 grains and (b) ZrO_2 particles, as well as (c) aspect ratio and length in long-axis direction of Ba-β-Al_2O_3 phase as a function of sintering temperature.

The ZrO_2 particles in all the samples became larger at higher temperatures due to faster diffusion rate of ions. As mentioned before, the reaction-formed ZrO_2 particles were larger than the YSZ particles. Thus, AB-10Z composites with YSZ additions showed smaller ZrO_2 particles than AB-2.5Z. Moreover, the particle sizes of the ZrO_2 in AB-10Z samples with a higher Y_2O_3 content were slightly smaller. Similar results have also been found in the sintering of Al_2O_3–(m-ZrO_2+t-ZrO_2) composites [21].

As shown in Fig. 3.7(c), the aspect ratio of the Ba-β-Al_2O_3 showed a similar downtrend with increasing sintering temperature. The length in long-axis direction of the Ba-β-Al_2O_3 phase was almost unchanged in all the samples with increasing sintering temperature, except for AB-2.5Z(Y) sample sintered at 1600 °C. Although the addition of Y_2O_3 degrades the densification of AB-2.5Z(Y) to some extent, the decreased aspect ratios of the elongated phase contributes to densification enhancement of the composites [22], thus resulting in higher density of AB-2.5Z(Y) than that of AB-2.5Z. On the other hand, lower aspect ratios of the elongated phase are favorable to ions diffusion [23,24], which promotes the grain growth of Al_2O_3 matrix and leads to larger grain sizes of Al_2O_3 in AB-2.5Z(Y) than that in AB-2.5Z.

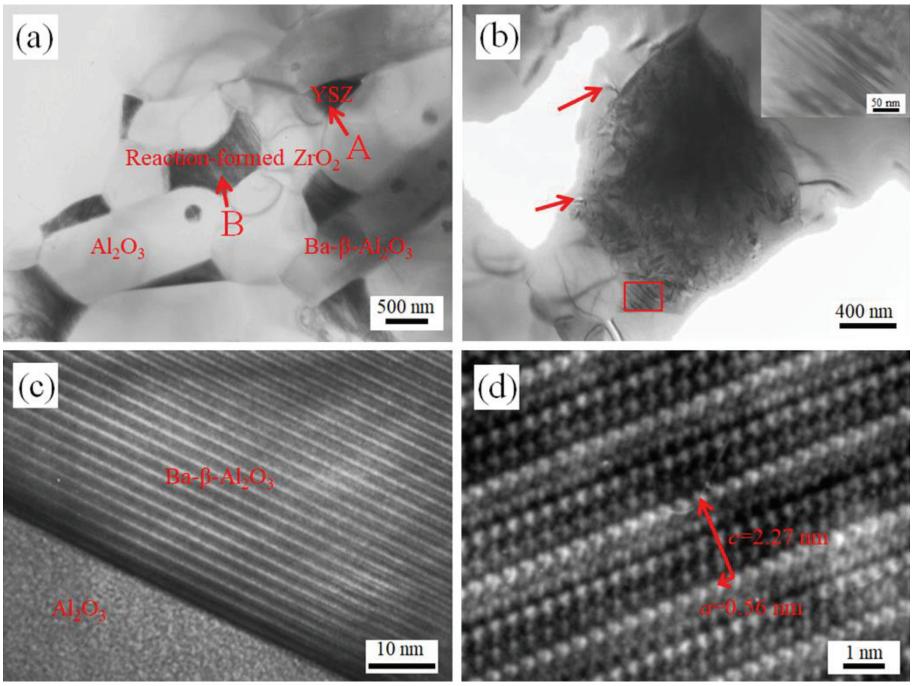

Fig. 3.8 TEM images of AB-10Z(3Y) sample sintered at 1600 °C. (a) Al_2O_3, reaction-formed ZrO_2, Ba-β-Al_2O_3, and YSZ, (b) ZrO_2, (c) interface between Al_2O_3 and Ba-β-Al_2O_3, and (d) HRTEM image of Ba-β-Al_2O_3 phase. Insert in (b) is an enlarged view of the rectangular area.

Table 3.2 EDS analyses of YSZ and ZrO_2 pointed by arrows “A” and ”B” in Fig. 3.8(a).

Positions	ZrO_2 (wt%)	Y_2O_3 (wt%)	Al_2O_3 (wt%)	BaO (wt%)
A	94.0	4.9	1.1	0
B	96.9	2.2	0.8	0.1

A low-magnification TEM image of the sintered AB-10Z(3Y) sample is shown in Fig. 3.8(a). The reaction-formed ZrO_2 is characterized by stacks of twins, which is the result of *t*→*m* martensitic transformation (indicated by the rectangular region and insert in Fig. 3.8(b)). The formation of twins prevents accumulation of excessive stresses [25], thus only limited microcracks (pointed by the arrows in Fig. 3.8(b)) were observed. Owing to smaller sizes and higher Y^{3+} content (Table 3.2) of YSZ particles, limited *t*→*m* transformation occurs in 3YSZ. In addition, the Ba-β-Al_2O_3 phase showed a layered structure (Fig. 3.8(c)). From the phase diagram of Al_2O_3-$BaAl_2O_4$ system [26], its lowest liquidus temperature is 1870 °C. The transient liquid phases existed in Al_2O_3-SrO [3] and Al_2O_3-CaO [27] systems do not appear during the formation of Ba-β-Al_2O_3 phase in the present work, which implies that the platelet structure of Ba-β-Al_2O_3 phase is ascribed to the preferred orientational diffusion of Ba cations, rather than the existence of liquid phase. From the HRTEM image of Ba-β-Al_2O_3 phase (Fig. 3.8(d)), the lattice parameters *a* and *c* were measured as 0.56 and 2.27 nm, respectively.

3.3.3 Mechanical properties

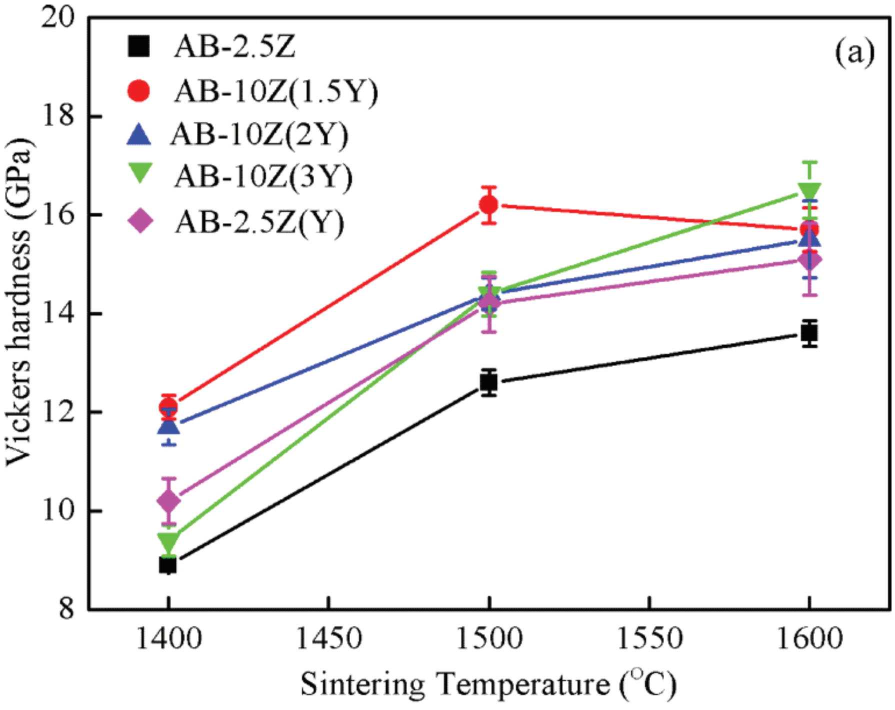

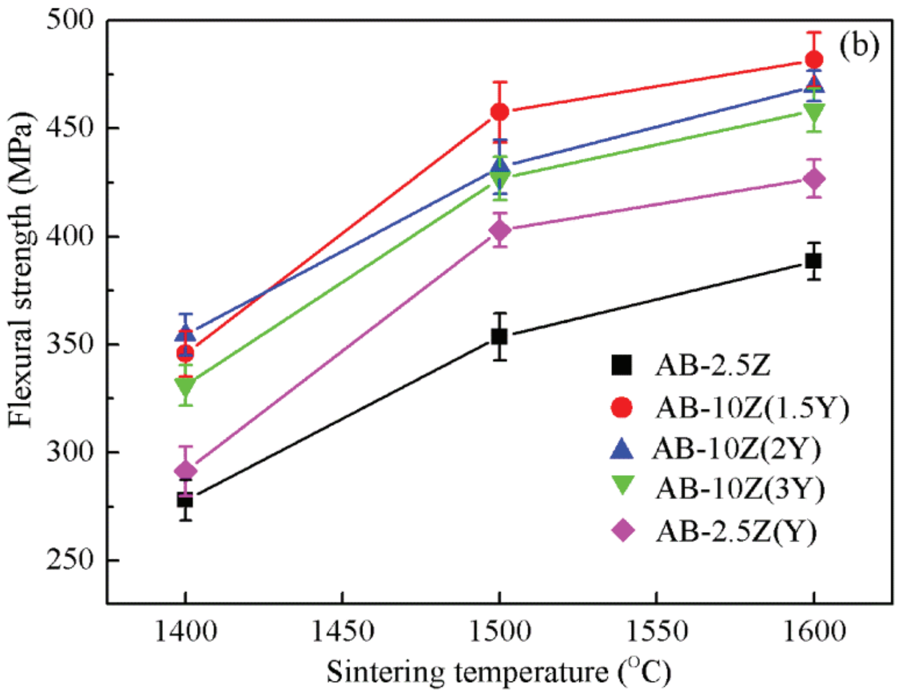

Fig. 3.9 (a) Vickers hardness and (b) flexural strength of in-situ synthesized samples sintered at different temperatures.

Fig. 3.9 shows the dependences of Vickers hardness and flexural strength on sintering temperature. The Vickers hardness and flexural strength were enhanced with increasing sintering temperature except for AB-10Z(1.5Y) sample sintered from 1500 to 1600 °C. AB-10Z samples exhibited higher hardness and strength values than AB-2.5Z and AB-2.5Z(Y) samples. The improved hardness and strength of the YSZ-added samples are likely to result from higher density, refined Al_2O_3 grains, and dispersion strengthening of the YSZ particles. For AB-10Z samples, the hardness was low at 1400 °C due to low density (Fig. 3.1). As the sintering temperature increased, the increase in density resulted in hardness improvement. For example, the AB-10Z(1.5Y) showed the highest hardness of 16.2 GPa at 1500 °C. AB-10Z(3Y) presented the highest hardness among AB-10Z samples sintered at 1600 °C, which is mainly attributed to the smallest Al_2O_3 grains and ZrO_2 particles. Besides, the expansion of ZrO_2 particles during $t \rightarrow m$ transformation could introduce compressive stresses [21], hence the strength of AB-10Z(1.5Y) showed the highest value among AB-10Z samples sintered at 1600 ^{o}C.

Fig. 3.10 illustrates the dependence of fracture toughness on sintering temperature. The fracture toughness of Al_2O_3/Ba-β-Al_2O_3/ZrO_2 composites was enhanced with increasing sintering temperature except for AB-2.5Z(Y) sintered at 1600 ^{o}C, where the fracture toughness was apparently lower than that at 1500 ^{o}C. Besides, the fracture toughness of Al_2O_3 matrix composites was improved due to the addition of YSZ or Y_2O_3. Fig. 3.11 shows the transformed ZrO_2 content during fracture process as a function of sintering temperature. The transformation amount of ZrO_2 from *t* to *m* phase increased with increasing sintering temperature except for AB-2.5Z(Y) sample sintered at 1600 ^{o}C. These results are in good agreement with the change in fracture toughness (Fig. 3.10). As shown in Fig. 3.11, the Al_2O_3/Ba-β-Al_2O_3/ZrO_2 composite with Y_2O_3 addition showed a lower $t \rightarrow m$ transformation amount at 1600 ^{o}C. This is because more Y^{3+} can diffuse into reaction-formed ZrO_2 at a higher temperature, resulting in stabilization of the ZrO_2. In particular, those reaction-formed ZrO_2 particles with smaller sizes may lose $t \rightarrow m$ phase transformation during fracture process.

The propagation behavior of cracks in AB-10Z(1.5Y) sample sintered at 1600 ^{o}C is shown in Fig. 3.12. The crack was deflected by Ba-β-Al_2O_3 phase and ZrO_2 particles, and crack bridging was also observed. The martensitic transformation of ZrO_2 inhibits crack propagation, while crack deflection/bridging increase the fracture surface areas and hence total energy consumed during crack propagation.

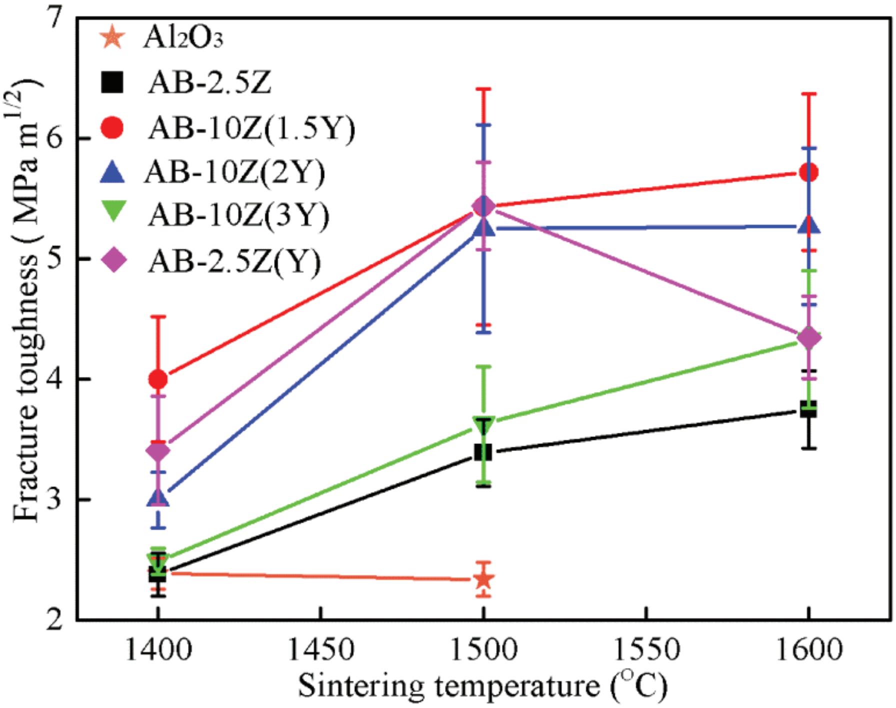

Fig. 3.10 Dependence of fracture toughness on sintering temperature.

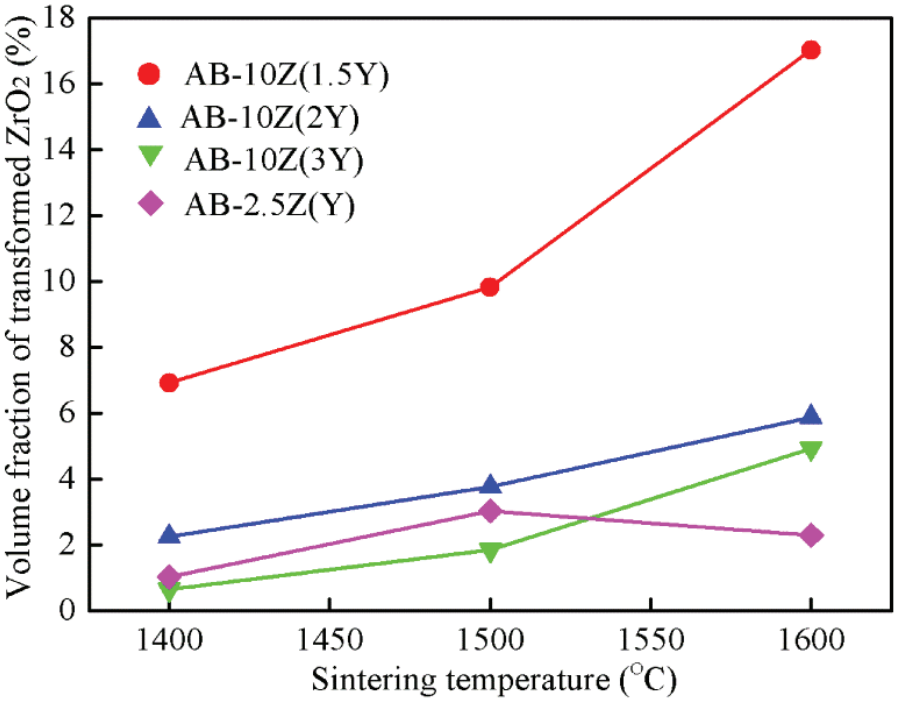

Fig. 3.11 Dependence of transformed ZrO_2 content on sintering temperature.

As shown in Figs. 3.10 and 11, the fracture toughness values of AB-10Z samples containing 1.5Y, 2Y, and 3Y were 5.7, 5.3, and 4.4 MPa $m^{1/2}$, respectively, which corresponded to transformed ZrO_2 amounts of 17.0, 5.9, and 4.9 vol%, respectively. As Y_2O_3 content in AB-10Z samples decreased, the volume fraction of $t \rightarrow m$ transformation ($V_{t \rightarrow m}$) during fracture process increased. Considering much higher amounts of transformed ZrO_2 in AB-10Z(1.5Y) than those in AB-10Z(2Y) and AB-10Z(3Y), together with the results obtained from TEM observations, most added 2YSZ and 3YSZ particles probably lose phase transformability and $t \rightarrow m$ phase transformation results mainly from the reaction-formed ZrO_2.

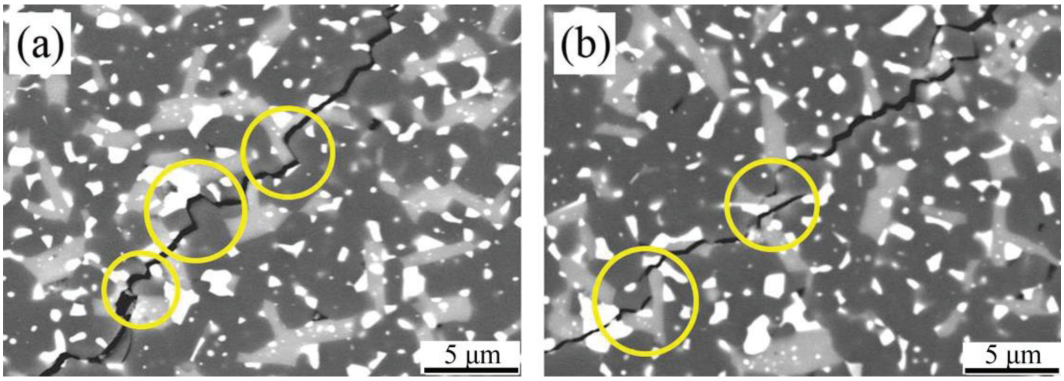

Fig. 3.12 SEM images showing (a) crack deflection and (b) crack bridging (indicated by the circles) behavior in AB-10Z(1.5Y) sample sintered at 1600 °C.

Based on the above results, the toughening mechanisms of Al_2O_3/Ba-β-Al_2O_3/ZrO_2 composites with YSZ or Y_2O_3 addition include $t \rightarrow m$ transformation toughening and crack deflection/bridging. In addition, these toughening mechanisms seem to have different contributions to the toughness of AB-10Z samples with different Y_2O_3 contents. For AB-10Z(1.5Y), transformation toughening of ZrO_2 is more important than crack deflection/bridging toughening, while crack deflection/bridging are predominant for AB-10Z(2Y) and AB-10Z(3Y). Due to much higher phase transformability of 1.5YSZ compared to 2YSZ and 3YSZ, the propagation of cracks may be significantly impeded in 1.5YSZ-added sample. As a result, limited Ba-β-Al_2O_3 phase deflects and bridges the cracks.

Although AB-2.5Z(Y) sample sintered at 1500 °C had comparable fracture toughness with AB-10Z(1.5Y) sample sintered at 1600 °C, YSZ-added samples showed higher flexural strength than AB-2.5Z(Y).

From the above discussion, there is no doubt that the introduction of YSZ or Y_2O_3 showed positive effects on mechanical properties of Al_2O_3/Ba-β-Al_2O_3/ZrO_2 composites. Although AB-2.5Z(Y) sample sintered at 1500 °C had comparable fracture toughness with AB-10Z(1.5Y) sample sintered at 1600 °C, YSZ-added samples showed higher Vickers hardness and flexural strength compared to AB-2.5Z and AB-2.5Z(Y) samples.

3.4 Conclusions

Al_2O_3/Ba-β-Al_2O_3/ZrO_2 composites were prepared via reactive sintering of Al_2O_3 and $BaZrO_3$ powders with additions of 1.5YSZ, 2YSZ, 3YSZ, and Y_2O_3, and the effects of YSZ with different Y_2O_3 contents and Y_2O_3 additions on microstructure and mechanical properties of Al_2O_3/Ba-β-Al_2O_3/ZrO_2 composites were investigated. According to the above results, the following conclusions can be drawn:

(1) The addition of YSZ or Y_2O_3 promoted the densification of Al_2O_3 matrix composites and phase transformation from *m*-ZrO_2 to *t*-ZrO_2. The grains of Al_2O_3

matrix were refined in YSZ-added samples, whereas Y_2O_3-added samples showed larger grain sizes of Al_2O_3 matrix. In addition, the Al_2O_3 grains and ZrO_2 particles in YSZ-added samples with a higher Y_2O_3 content exhibited slightly smaller sizes.

(2) The enhanced Vickers hardness and flexural strength of the composites with YSZ additions are ascribed to refined Al_2O_3 grains, dispersion strengthening of the YSZ particles, and enhanced densification of the composites. The optimum Vickers hardness (16.3 GPa) and flexural strength (481.8 MPa) were obtained in Al_2O_3/Ba-β-Al_2O_3/ZrO_2 composites with additions of 7.5 vol% 3YSZ and 1.5YSZ, respectively.

(3) The improved fracture toughness of Al_2O_3/Ba-β-Al_2O_3/ZrO_2 composites with YSZ and Y_2O_3 additions is attributed to crack deflection/bridging and $t \rightarrow m$ transformation toughening. The phase transformation mainly comes from reaction-formed ZrO_2, but 1.5YSZ particles added in the composites also showed high phase transformability. The optimum fracture toughness (5.7 MPa $m^{1/2}$) was obtained by adding 7.5 vol% 1.5YSZ.

References

1. L. An, H.M. Chan, R-curve behavior of in-situ-toughened Al_2O_3: $CaAl_{12}O_{19}$ ceramic composites, J. Am. Ceram. Soc. 79 (1996) 3142–3148.
2. D. Asmi, I.M. Low, Processing of an in-situ layered and graded alumina/calcium-hexaluminate composite: physical characteristics, J. Eur. Ceram. Soc. 18 (1998) 2019–2024.
3. K. Vishista, F.D. Gnanam, Microstructural development of $SrAl_{12}O_{19}$ in alumina-strontia composites, J. Eur. Ceram. Soc. 29 (2009) 77–83.
4. M. Yasuoka, K. Hirao, M.E. Brito, S. Kanzaki, High-strength and high-fracture-toughness ceramics in the $Al_2O_3/LaAl_{11}O_{18}$ systems, J. Am. Ceram. Soc. 78 (1995) 1853–1856.
5. H. Tang, M.H. Fang, X. Min, X.J. Wang, Z.H. Huang, R.L. Wen, Y.A. Liu, X.W. Wu, Mechanical properties and solid particle erosion behavior of $LaMgAl_{11}O_{19}$-Al_2O_3 ceramic at room and elevated temperatures, J. Am. Ceram. Soc. 99 (2016) 2138–2146.
6. H. Tang, M.H. Fang, C. Tang, Z.H. Huang, H.T. Liu, H.K. Zhu, Y.A. Liu, X.W. Wu, Effect of $LaMgAl_{11}O_{19}$ addition and temperature on the mechanical properties of Al_2O_3-based ceramics, Mater. Sci. Eng. A 655 (2016) 160–167.
7. Z. Negahdari, M. Willert-Porada, Tailoring the microstructure of reaction-sintered alumina/lanthanum hexaaluminate particulate composites, J. Eur. Ceram. Soc. 30 (2010) 1381–1389.
8. Z.C. Chen, K.K. Chawla, M. Koopman, Microstructure and mechanical

properties of in situ synthesized alumina/Ba-β-alumina/zirconia composites, Mater. Sci. Eng. A 367 (2004) 24–32.

9. Z.C. Chen, S. Nugroho, M. Ezumi, T. Akao, T. Onda, In situ synthesis of alumina-matrix oxide/oxide composites by reactive sintering, Mater. Sci. Eng. A 557 (2012) 59–68.
10. X.L. Chen, Y.F. Zhang, X.H. Zhong, Z.H. Xu, J.F. Zhang, Y.L. Cheng, Y. Zhao, Y.J. Liu, X.Z. Fan, Y. Wang, H.M. Ma, X.Q. Cao, Thermal cycling behaviors of the plasma sprayed thermal barrier coatings of hexaluminates with magnetoplumbite structure, J. Eur. Ceram. Soc. 30 (2010) 1649–1657.
11. W.Z. Zhu, Grain size dependence of the transformation temperature of tetragonal to monoclinic phase in ZrO_2 (Y_2O_3) ceramics, Ceram. Int. 22 (1996) 389–395.
12. R.H.J. Hannink, P.M. Kelly, B.C. Muddle, Transformation toughening in zirconia-containing ceramics, J. Am. Ceram. Soc. 83 (2000) 461–487.
13. A. Suresh, M.J. Mayo, W.D. Porter, C.J. Rawn, Crystallite and grain-size-dependent phase transformations in yttria-doped zirconia, J. Am. Ceram. Soc. 86 (2003) 360–362.
14. R.C. Garvie, P.S. Nicholson, Phase analysis in zirconia systems, J. Am. Ceram. Soc. 55 (1972) 303–305.
15. A.G. Evans, E.A. Charles, Fracture toughness determinations by indentation, J. Am. Ceram. Soc. 59 (1976) 371–372.
16. Y. Moriyoshi, Y. Chida, T. Ikegami, H. Yamamura, A. Watanabe, Microstructure in Al_2O_3-ZrO_2 ceramics, in: S. Sōmiya, (Ed.), Zirconia ceramics, Uchida

Rokakuho Publishing Co., Ltd., Tokyo, 1983, pp. 97–108.

17. K. Maiti, A. Sil, Microstructural relationship with fracture toughness of undoped and rare earths (Y, La) doped Al_2O_3–ZrO_2 ceramic composites, Ceram. Int. 37 (2011) 2411–2421.
18. Y.P. Ye, J.G. Li, H.D. Zhou, J.M. Chen, Microstructure and mechanical properties of yttria-stabilized ZrO_2/Al_2O_3 nanocomposite ceramics, Ceram. Int. 34 (2008) 1797–1803.
19. G. Yang, J.C. Li, G.C. Wang, M. Yashima, S.L. Min, Influences of ZrO_2 nanoparticles on the microstructure and mechanical behavior of Ce-TZP/Al_2O_3 nanocomposites, J. Mater. Sci. 40 (2005) 6087–6090.
20. J.X. Fang, A.M. Thompson, M.P. Harmer, H.M. Chan, Effect of yttrium and lanthanum on the final-stage sintering behavior of ultrahigh-purity alumina, J. Am. Ceram. Soc. 80 (1997) 2005–2012.
21. W.H. Tuan, R.Z. Chen, T.C. Wang, C.H. Cheng, P.S. Kuo, Mechanical properties of Al_2O_3/ZrO_2 composites, J. Eur. Ceram. Soc. 22 (2002) 2827–2833.
22. C. Domínguez, J. Chevalier, R. Torrecillas, L. Gremillard, G. Fantozzi, Thermomechanical properties and fracture mechanisms of calcium hexaluminate, J. Eur. Ceram. Soc. 21 (2001) 907–917.
23. L. Xu, M. Chen, L.Y. Jin, X.L. Yin, N. Wang, L. Liu, Effect of ZrO_2 addition on densification and mechanical properties of $MgAl_2O_4$-$CaAl_4O_7$-$CaAl_{12}O_{19}$ composite, J. Am. Ceram. Soc. 98 (2015) 4117–4123.
24. L. Liu, M. Chen, L. Xu, X.L. Yin, W.J. Sun, Effect of BaO addition on

densification and mechanical properties of Al_2O_3-MgO-CaO refractories, Metals 6 (2016) 84.

25. J.A. Krogstad, R.M. Leckie, S. Krämer, J.M. Cairney, D.M. Lipkin, C.A. Johnson, C.G. Levi, Phase evolution upon aging of air plasma sprayed *t*′-zirconia coatings: II-microstructure evolution, J. Am. Ceram. Soc. 96 (2013) 299–307.
26. S. Kimura, E. Bannai, I. Shindo, Phase relations relevant to hexagonal barium aluminates, Mater. Res. Bull. 17 (1982) 209–215.
27. R. Salomão, V.L. Ferreira, I.R. de Oliveira, A.D.V. Souza, W.R. Correr, Mechanism of pore generation in calcium hexaluminate (CA_6) ceramics formed in situ from calcined alumina and calcium carbonate aggregates, J. Eur. Ceram. Soc. 36 (2016) 4225–4235.

Chapter 4: Effect of high-energy ball-milling on properties of Al_2O_3/Ba-β-Al_2O_3/ZrO_2 composites

4.1 Introduction

The elongated Ba-β-Al_2O_3 phase with a layered β-Al_2O_3 structure and monoclinic zirconia (*m*-ZrO_2) particles were formed during reactive sintering of Al_2O_3 and $BaZrO_3$ powders, which has been reported by Chen et al. [1,2]. The elongated Ba-β-Al_2O_3 phase is believed to enhance the fracture toughness of Al_2O_3 matrix composites through crack deflection and crack bridging. To further improve the mechanical properties of Al_2O_3/Ba-β-Al_2O_3/*m*-ZrO_2 composites, the effects of different 3 mol% yttria-stabilized zirconia (3YSZ) contents and YSZ with different Y_2O_3 contents have been investigated in chapter 2 and chapter 3 [3,4].

The layered β-Al_2O_3 structure makes Ba-β-Al_2O_3 phase difficult to be densified by conventional solid-state reaction sintering due to the suppressed interlayer diffusion of atoms [5]. To obtain fully dense ceramics, high sintering temperatures, hot pressing (HP), microwave sintering, and spark plasma sintering (SPS) have been widely used. Compared to HP, SPS, and microwave sintering, conventional solid-state reactions are much more suitable for mass production. In addition, higher sintering temperatures and longer sintering duration presumably lead to abnormal grain growth, which is detrimental to the mechanical properties of ceramics. Considering these aspects, mechanical activation synthesis of materials has paid much attention in preparing compounds [6-13]. The high-energy ball-milling (HEBM) has been successfully used as a vehicle to obtain fine and uniform dispersion, as well as enhanced reactivity of powders for solid-state reactions [14,15].

In this chapter, the influences of HEBM on sintering ability, microstructure, and mechanical properties of Al_2O_3/Ba-β-Al_2O_3/ZrO_2 composites were investigated.

4.2 Experimental procedure

Al_2O_3 (average particle size 0.16 μm, 99.99% purity; Taimei Chemicals, Tokyo, Japan), 3YSZ (3 mol% Y_2O_3-ZrO_2 (TZ-3Y); 50 nm, 99.9% purity; Tosoh, Tokyo), and $BaZrO_3$ (1.5 μm, 99% purity; Kojundo Chemical Lab., Saitama, Japan) powders were used as the starting materials. The nominal composition of Al_2O_3/Ba-β-Al_2O_3/ZrO_2 composites was: 70 vol% Al_2O_3, 20 vol% Ba-β-Al_2O_3, and 10 vol% (YSZ + *m*-ZrO_2). The as-received Al_2O_3 and $BaZrO_3$ powders were milled in ethanol with ZrO_2 balls (5 mm in diameter) as milling media using a planetary ball-milling system for different ball-milling times: 0, 4, 8, 12, 24, 48, and 72 h. The mass ratio of ball to powder was equal to 10:1, and the milling speed was 200 rpm. Then the high-energy ball-milled powder mixtures of Al_2O_3 and $BaZrO_3$ were mixed with YSZ powder in ethanol for 24 h at a speed of 90 rpm using Al_2O_3 balls as milling media. After milling, the mixtures were dried at 110 °C for 24 h. The pellets (sized Φ19 mm × 3 mm) were prepared by uniaxial pressing at 20 MPa for 2 min, followed by cold isostatic pressing at 200 MPa for 2 min. These prepared samples were sintered in an electric furnace at 1400, 1500, and 1600 °C in air with a heating rate of 400 °C/h and a dwelling time of 2 h at each temperature. The samples were then cooled down to room temperature at a rate of 400 °C/h.

The density of the sintered samples was measured in distilled water using the Archimedes' principle. The densification behavior of Al_2O_3-$BaZrO_3$ powder mixtures (Φ6 mm×15 mm) was performed at 5 °C/min from room temperature to 1500 °C using thermal dilatometer (DL-9800, ULVAC, Japan). The phase identification of ball-milled powders of Al_2O_3 and $BaZrO_3$ was investigated by X-ray diffraction (XRD; RINT-TTR III, Rigaku, Japan) using Cu Kα radiation with a step of 0.02^{o} (2θ) and a scanning rate of 2 ^{o}/min ranging from 15^{o} to 75^{o}. The crystallite sizes of Al_2O_3 and $BaZrO_3$ powders were estimated using the Scherrer formula.

Microstructural observations were conducted by scanning electron microscopy (FE-SEM; S4800, Hitachi, Japan) on polished surfaces after thermal etching at 1300 °C for 30 min. The Vickers hardness and fracture toughness were determined by an indentation method using a load of 98 N with a holding time of 15 s, and 10 indentations were made to obtain representative mean values of hardness and toughness. The fracture toughness was calculated by the following equation [16].

$$K_{\mathrm{IC}} = 0.16 HV \cdot a^{1/2} \cdot (c / a)^{-3/2} \tag{4.1}$$

where K_{IC} is the fracture toughness (MPa $m^{1/2}$), HV is the Vickers hardness (MPa), a is the half diagonal length of the indentation (m), and c is the half length of the radical crack (m).

4.3 Results and discussion

4.3.1 Powder characterization

Fig. 4.1 shows the SEM images of the two starting powders (Al_2O_3 and $BaZrO_3$) and corresponding powders ball-milled for 48 h. Particle breakage takes place by the collision of balls in many places. The collision between the balls falling down after reaching maximum height would be the most efficient for particle size reduction. Because the container wall is made of refractory material (ZrO_2 ceramics), the collision between the balls and container wall would also be one of the efficient ways of particle breakage [9]. No significant difference between initial Al_2O_3 powder and Al_2O_3 powder ball-milled for 48 h in terms of the particle size was observed. The particle size of $BaZrO_3$ powder was reduced efficiently and individual $BaZrO_3$ particle was even difficult to identify. Thus, more contact points between the particles are formed, favoring the sintering process of the composites, as shown below.

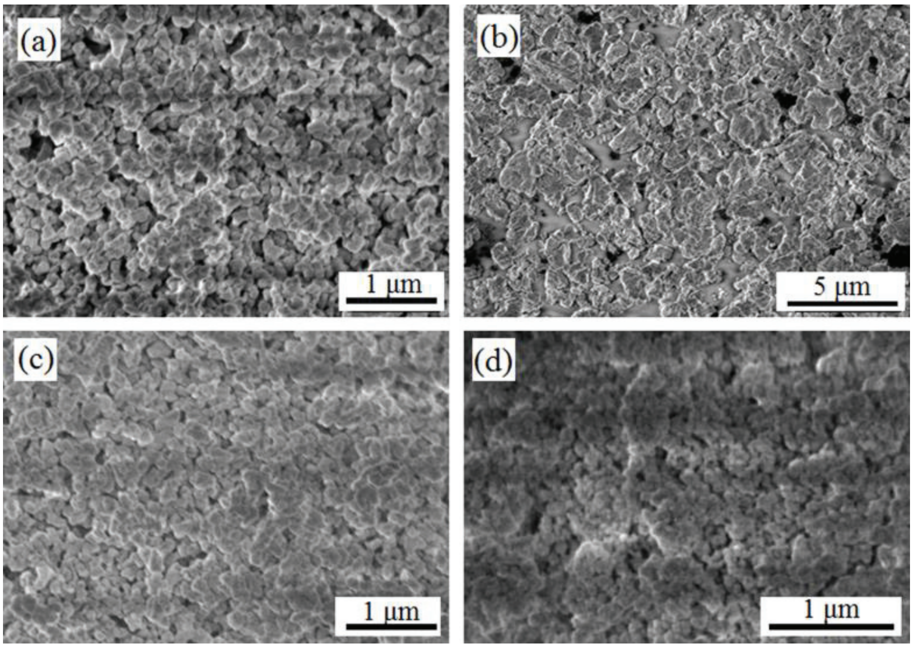

Fig. 4.1 SEM images of starting powders: (a) Al_2O_3, (b) $BaZrO_3$, and powders ball-milled for 48 h: (c) Al_2O_3, (d) $BaZrO_3$.

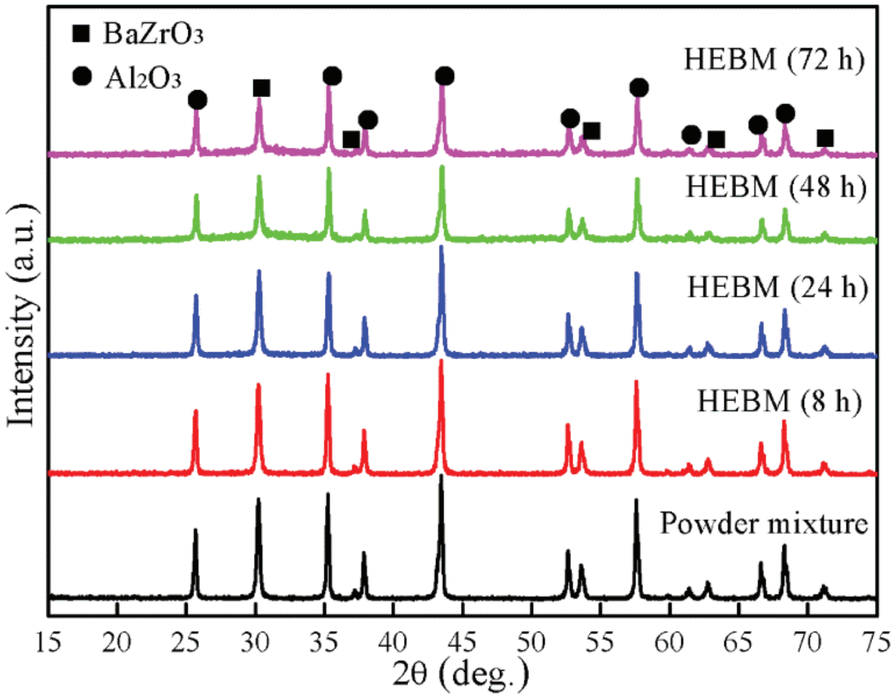

Fig. 4.2 XRD patterns of Al_2O_3 and $BaZrO_3$ powders with different ball-milling times.

The XRD patterns of Al_2O_3 and $BaZrO_3$ powders with different ball-milling times are shown in Fig. 4.2. All the XRD patterns of the ball-milled powders were similar to those of two starting powders. No new phase was observed even after ball-milling for 72 h, indicating that the reactions between Al_2O_3 and $BaZrO_3$ do not occur during the HEBM process. The crystallite sizes of Al_2O_3 and $BaZrO_3$ powders as a function of ball-milling time were determined from the XRD results using Scherrer formula and the results are presented in Fig. 4.3. The crystallite size of $BaZrO_3$ powder (Fig. 4.3) decreased as the ball-milling time increased, which is consistent with the variations of the particle size (Fig. 4.1). However, this should be ruled out for Al_2O_3 powder. As shown in Fig. 4.1, there was no significant refinement of Al_2O_3 powder after ball-milling for 48 h, resulting from the small initial particle size (average particle size: 0.16 μm). The milling process only increased the lattice strain of Al_2O_3 powder, not resulting in a refinement in particle size. The residual stress induced by HEBM is likely responsible for the wider XRD peaks of Al_2O_3 powder, which has also been reported in previous literature [17].

The shrinkage curves of Al_2O_3-$BaZrO_3$ powder mixtures as a function of temperature are shown in Fig. 4.4. The temperature at which densification commenced (T_{dens}) was decreased with increasing ball-milling time, especially the powder mixtures ball-milled for 48 and 72 h. In addition, the maximum shrinkages (S_{max}) of the powder mixtures ball-milled for 48 and 72 h were obviously larger than those ball-milled for 0, 8, and 24 h. This implies that the HEBM promotes the densification of the composites, whereas significant shrinkage behavior was observed until ball-milling for 48 h, which is attributed to the much less pronounced powder refinement of wet milling than that of dry milling [9].

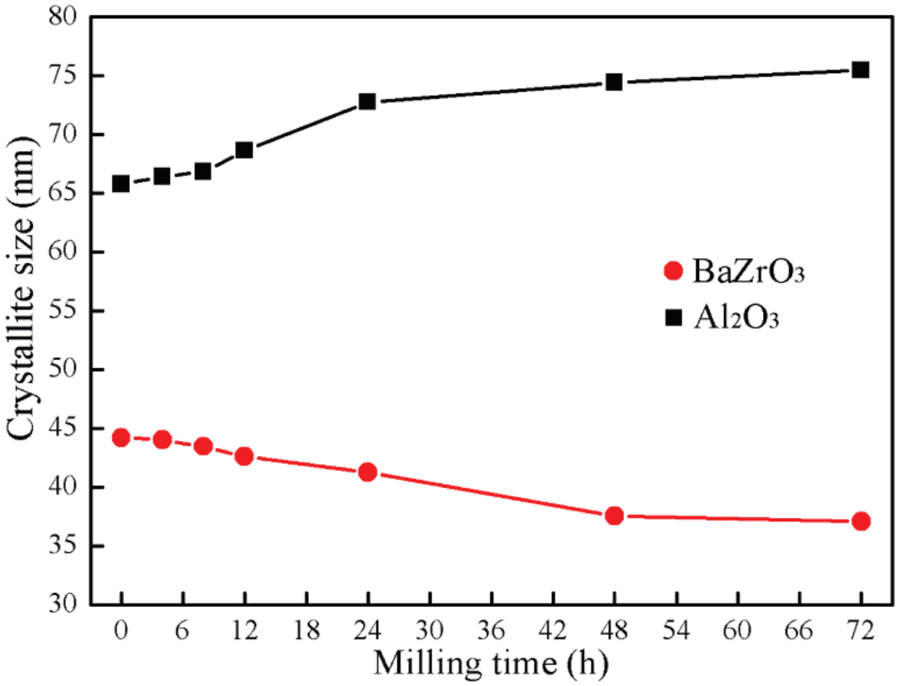

Fig. 4.3 Crystallite sizes of Al_2O_3 and $BaZrO_3$ powders as a function of ball-milling time.

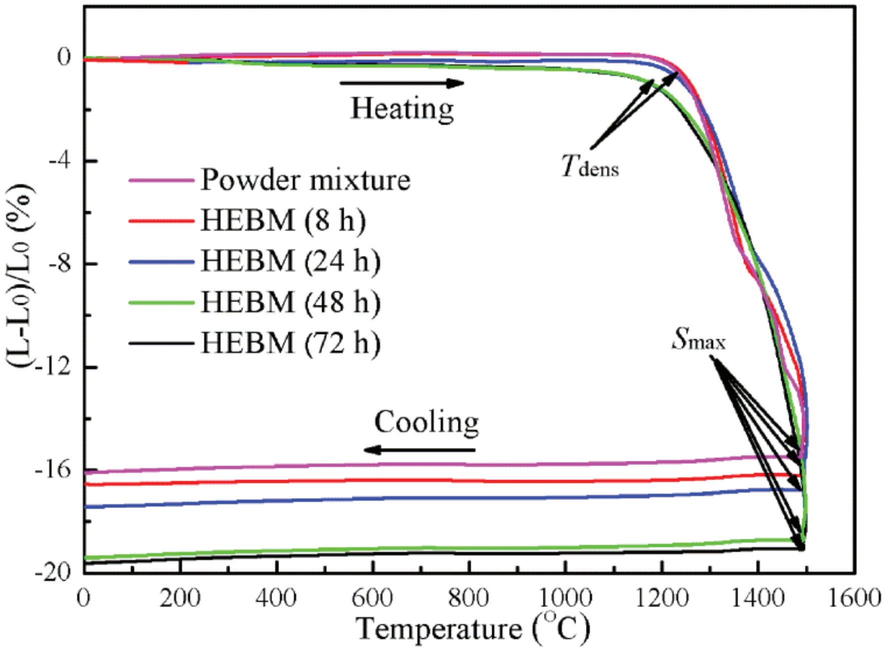

Fig. 4.4 Shrinkage curves of Al_2O_3-$BaZrO_3$ powder mixtures as a function of temperature.

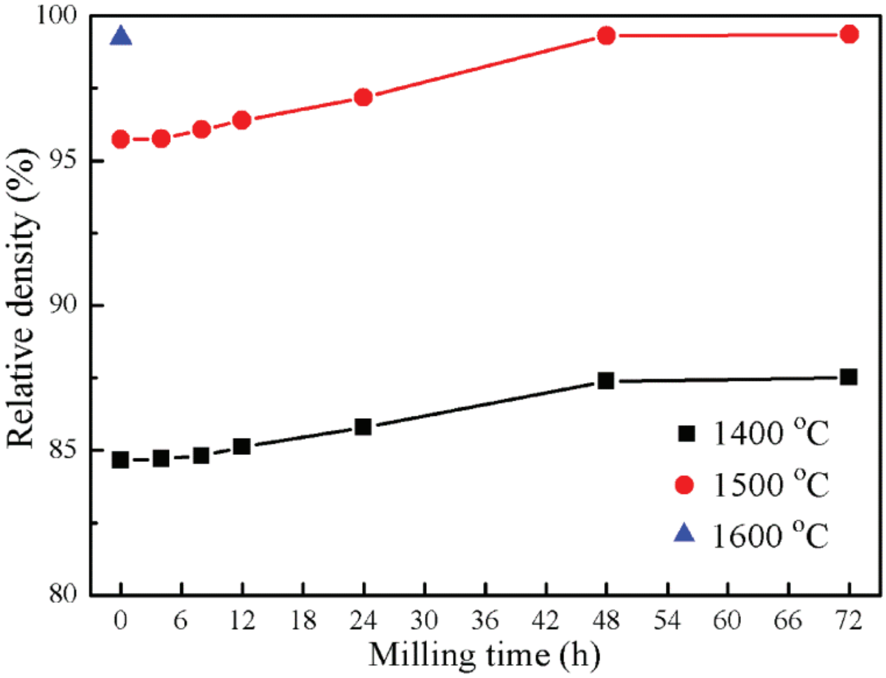

Fig. 4.5 Relative density of Al_2O_3/Ba-β-Al_2O_3/ZrO_2 composites as a function of ball-milling time.

Fig. 4.5 shows the relative density of Al_2O_3/Ba-β-Al_2O_3/ZrO_2 composites as a function of ball-milling time. The relative density of the composites increased as the ball-milling time increased, at 1400 and 1500 °C. Low relative density value of 87.5% was obtained for the sample sintered at 1400 °C even ball-milling for 72 h, suggesting the poor sintering ability and slow diffusion rate of ions at 1400 °C. With increasing sintering temperature to 1500 °C, an increase in relative density from 95.7 to 99.4% was observed with the increase in ball-milling time from 0 to 72 h. This indicates that the HEBM promotes the densification of Al_2O_3/Ba-β-Al_2O_3/ZrO_2 composites, in particular at 1500 °C.

4.3.2 Microstructure

The SEM images (backscattered electron mode) of the polished and then thermally etched Al_2O_3/Ba-β-Al_2O_3/ZrO_2 composites sintered at 1500 ^{o}C are shown in Fig. 4.6. Equiaxed Al_2O_3 grains, white ZrO_2 particles and elongated Ba-β-Al_2O_3 phase were observed. For the sample without HEBM (Fig. 4.6(a)), the Ba-β-Al_2O_3 phase showed high aspect ratios (higher than 5:1), which is responsible for the pores existed in the sample. When Al_2O_3 and $BaZrO_3$ powders were mixed by HEBM, the aspect ratio of the Ba-β-Al_2O_3 decreased and denser microstructure was formed. In particular, an almost fully dense structure was observed in the sample ball-milled for 72 h, and the Ba-β-Al_2O_3 phase presented a more equiaxed morphology with lower aspect ratios (approximate to 3:1).

As reported in the literature [1-5], the platelet morphology of Ba-β-Al_2O_3 phase results from the preferred orientational diffusion of Ba^{2+}. When the starting powders were prepared without HEBM, the Ba-β-Al_2O_3 phase exhibited elongated morphology with high aspect ratios. On the other hand, owing to the decreased amount of $BaZrO_3$ powder near Al_2O_3 powder by using HEBM (Fig. 4.7), there were insufficient Ba^{2+} to diffuse to develop high aspect ratios. It can be concluded that the morphology of Ba-β-Al_2O_3 phase is associated with the particle size and particle distribution of the starting powders in green specimens. Similar results have also been found in fabricating calcium hexaluminate ($CaAl_{12}O_{19}$, or CA_6) ceramics [18].

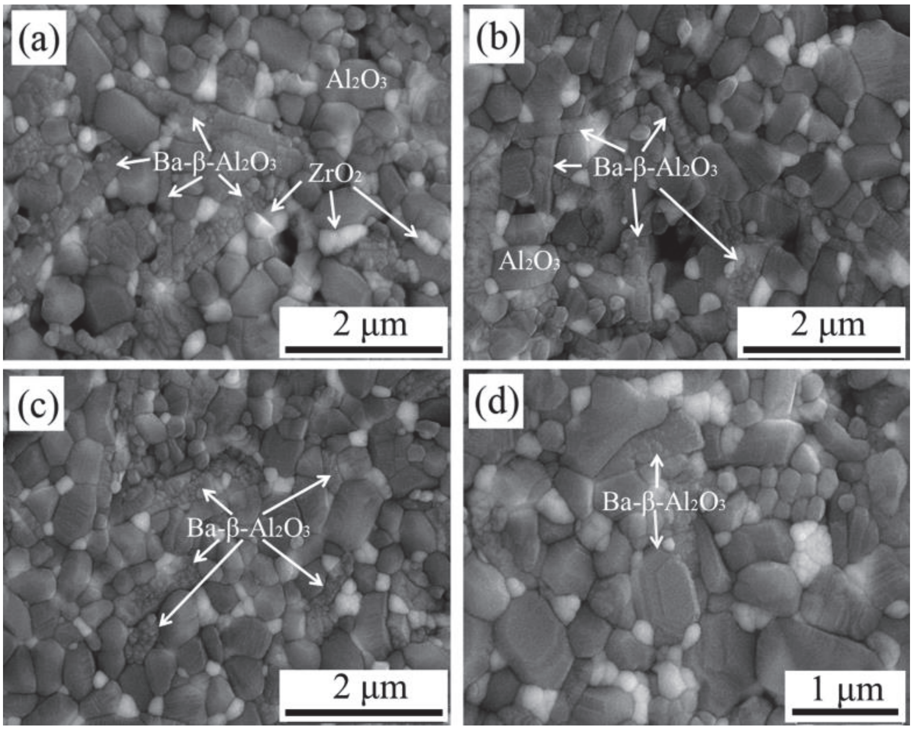

Fig. 4.6 SEM images showing the microstructure of Al_2O_3/Ba-β-Al_2O_3/ZrO_2 composites sintered at 1500 °C with different ball-milling times: (a) 0 h, (b) 24 h, (c) 48 h, and (d) 72 h.

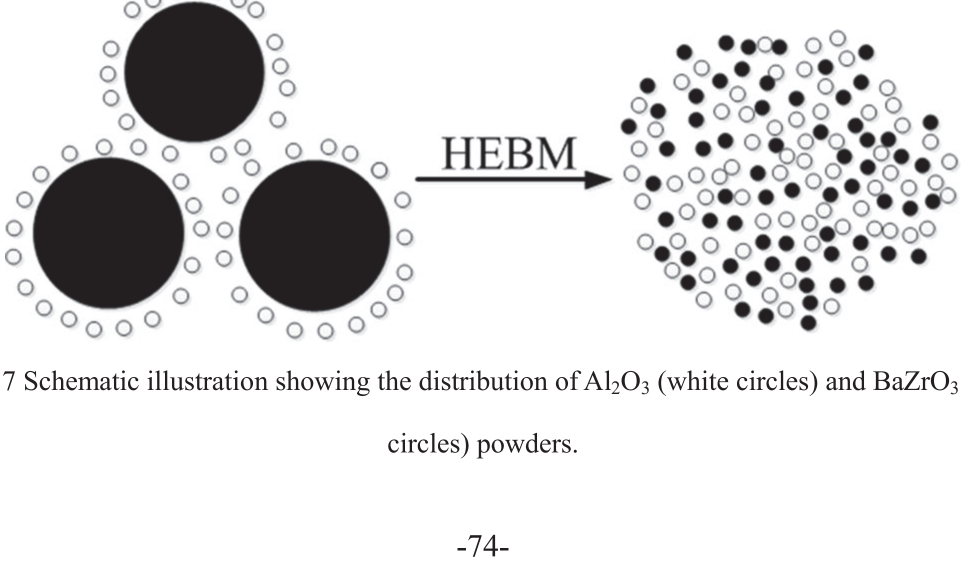

Fig. 4.7 Schematic illustration showing the distribution of Al_2O_3 (white circles) and $BaZrO_3$ (black circles) powders.

4.3.3 Mechanical properties

Vickers hardness and fracture toughness of Al_2O_3/Ba-β-Al_2O_3/ZrO_2 composites as a function of ball-milling time are shown in Fig. 4.8. For the samples sintered at 1400 °C, the effect of ball-milling time on Vickers hardness was insignificant, resulting from a slight increase in relative density. In general, the Vickers hardness values were lower than 10 GPa. In addition, the Vickers hardness of the samples sintered at 1500 °C was improved significantly with increasing ball-milling time, which is mainly ascribed to the enhancement of densification. The sample sintered at 1600 °C without HEBM presented the hardness value of 16.2 GPa, while the sample ball-milled for 72 h and sintered at 1500 °C showed the highest hardness value of 17.3 GPa. This is mainly attributed to the refinement of Al_3O_2 grains and ZrO_2 particles (Table 4.1). Furthermore, the dispersion strengthening of ZrO_2 particles is also considered to be enhanced due to the refined ZrO_2 particles.

Table 4.1 Particle sizes of ZrO_2 in Al_2O_3/Ba-β-Al_2O_3/ZrO_2 composites sintered at different temperatures with different ball-milling times (μm).

Ball-milling times (h)	1400 °C	1500 °C	1600 °C
0	0.26	0.33	0.48
8	0.26	0.32	-
24	0.24	0.31	-
48	0.20	0.25	-
72	0.19	0.25	-

In comparison with the samples sintered at 1400 °C, the samples sintered at 1500 °C presented a higher increase rate of fracture toughness as a function of ball-milling time, achieving an increase from 3.5 to 4.0 MPa $m^{1/2}$. The reduction of the aspect ratios of the Ba-β-Al_2O_3 probably leads to the degradation of fracture toughness to some extent [19-21]. However, owing to the reduced particle size of $BaZrO_3$, smaller reaction-formed ZrO_2 particles formed by the reactions are more easily stabilized in denser microstructure, contributing to the improvement of fracture toughness.

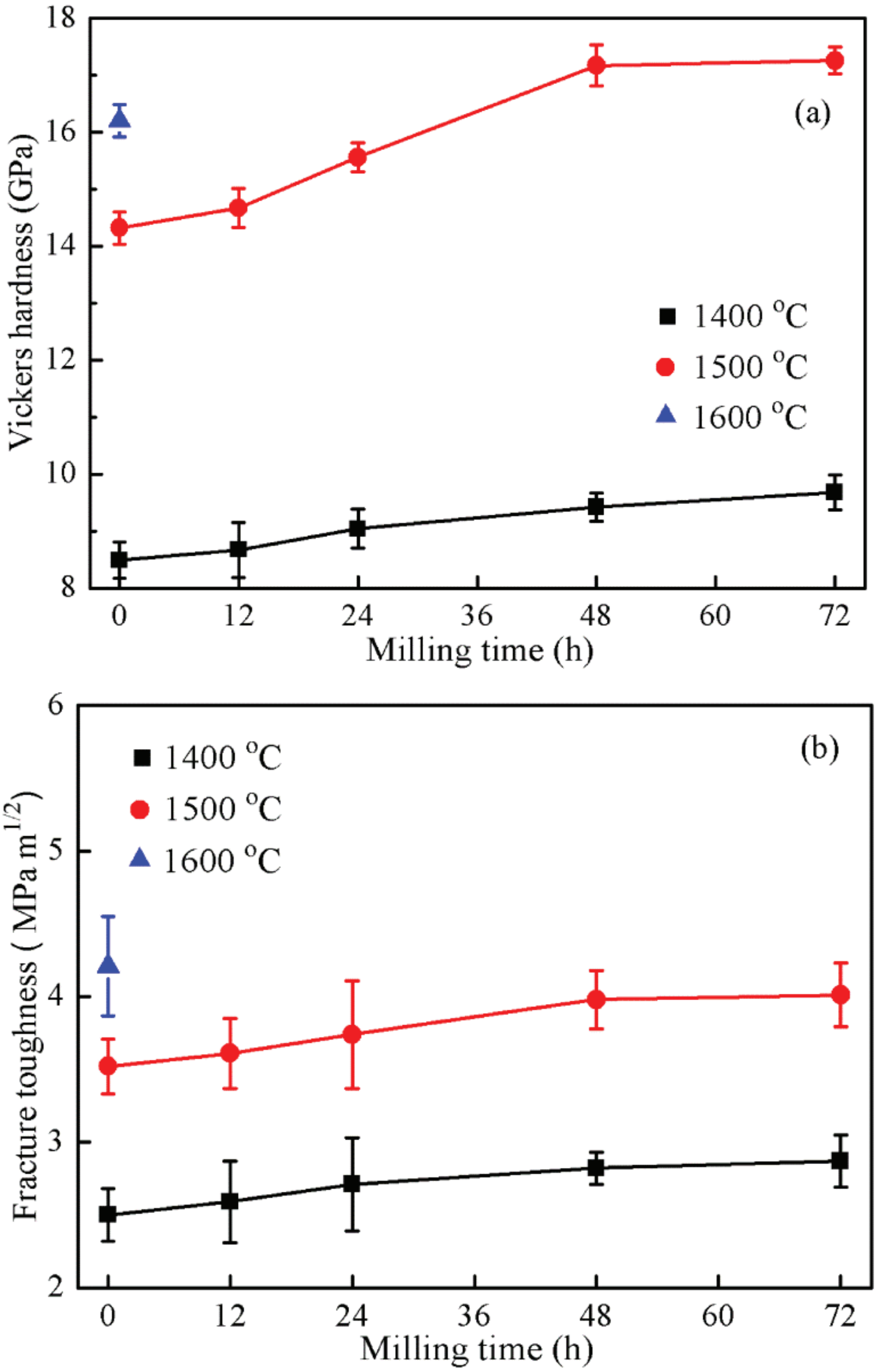

Fig. 4.8 (a) Vickers hardness and (b) fracture toughness of Al_2O_3/Ba-β-Al_2O_3/ZrO_2 composites as a function of ball-milling time.

4.4 Conclusions

Al_2O_3/Ba-β-Al_2O_3/ZrO_2 composites were prepared by solid-state reaction sintering of high-energy ball-milled Al_2O_3–$BaZrO_3$ powder mixtures and YSZ nanopowder. Fully dense Al_2O_3/Ba-β-Al_2O_3/ZrO_2 composites with fine microstructure were successfully fabricated at 1500 °C using HEBM. The HEBM significantly reduced the particle size and crystallite size of $BaZrO_3$ powder, but did not decrease the particle size of Al_2O_3. Owing to grain refinement of Al_2O_3 matrix and ZrO_2 particles, as well as enhanced dispersion strengthening of ZrO_2 particles, Al_2O_3/Ba-β-Al_2O_3/ZrO_2 composites sintered at 1500 °C, based on powders ball-milled for 48 and 72 h, exhibited larger Vickers hardness than at 1600 °C without HEBM.

References

1. Z.C. Chen, S. Nugroho, M. Ezumi, T. Akao, T. Onda, In situ synthesis of alumina-matrix oxide/oxide composites by reactive sintering, Mater. Sci. Eng. A 557 (2012) 59–68.
2. Z.C. Chen, K.K. Chawla, M. Koopman, Microstructure and mechanical properties of in situ synthesized alumina/Ba-β-alumina/zirconia composites, Mater. Sci. Eng. A 367 (2004) 24–32.
3. L. Liu, K. Maeda, T. Onda, Z.C. Chen, Effect of YSZ with different Y_2O_3 contents on toughening behavior of Al_2O_3/Ba-β-Al_2O_3/ZrO_2 composites, Ceram. Int. 45 (2019) 18037–18043.
4. L. Liu, K. Maeda, T. Onda, Z.C. Chen, Microstructure and improved mechanical properties of Al_2O_3/Ba-β-Al_2O_3/ZrO_2 composites with YSZ addition, J. Eur. Ceram. Soc. 38 (2018) 5113–5121.
5. L. Liu, Y. Takasu, T. Onda, Z.C. Chen, Influence of in-situ synthesized Ba-β-Al_2O_3 on mechanical properties and thermal shock resistance of ZTA/Ba-β-Al_2O_3 composites, Ceram. Int. 46 (2020) 3738–3743
6. P. Molaiyan, R. Witter, Mechanochemical synthesis of solid-state electrolyte $Sm_{1-x}CaxF_{3-x}$ for batteries and other electrochemical devices, Mater. Lett. 244 (2019) 22–26.
7. C. Santos, M.H. Koizumi, J.K.M.F. Daguano, F.A. Santos, C.N. Elias, A.S. Ramos, Properties of Y-TZP/Al_2O_3 ceramic nanocomposites obtained by high-energy ball milling, Mater. Sci. Eng. A 502 (2009) 6–12.

8. A.O. Zhigachev, A.V. Umrikhin, Y.I. Golovin, The effect of calcia content on phase composition and mechanical properties of Ca-TZP prepared by high-energy milling of baddeleyite, Ceram. Int. 41 (2015) 13804–13809.

9. A.L. Ortiz, F. Sánchez-Bajo, V.M. Candelario, F. Guiberteau, Comminution of B_4C powders with a high-energy mill operated in air in dry or wet conditions and its effect on their spark-plasma sinterability, J. Eur. Ceram. Soc. 37 (2017) 3873–3884.

10. M. Ahsanzadeh-Vadeqani, R.S. Razavia, M. Barekat, G.H. Borhani, A.K. Mishra, Preparation of yttria nanopowders for use in transparent ceramics by dry ball-milling technique, J. Eur. Ceram. Soc. 37 (2017) 2169–2177.

11. H.H. Kumar, C.M. Lonkar, K. Balasubramanian, Structure-property correlation and harvesting power from vibrations of aerospace vehicles by nanocrystalline La-Pb($Ni_{1/3}Sb_{2/3}$)-$PbZrTiO_3$ ferroelectric ceramics synthesized by mechanical activation, J. Am. Ceram. Soc. 100 (2017) 215–223.

12. Q.L. He, A.Y. Wang, C. Liu, W.M. Wang, H. Wang, Z.Y. Fu, Microstructures and mechanical properties of B_4C-TiB_2-SiC composites fabricated by ball milling and hot pressing, J. Eur. Ceram. Soc. 38 (2018) 2832–2840.

13. L. Feng, S.H. Lee, H.L. Wang, H.S. Lee, Nanostructured HfC–SiC composites prepared by high-energy ball-milling and reactive spark plasma sintering, J. Eur. Ceram. Soc. 36 (2016) 235–238.

14. C. Suryanarayana, E. Ivanov, V.V. Boldyrev, The science and technology of mechanical alloying, Mater. Sci. Eng. A 304 (2001) 151–158.

15. C. Suryanarayana, Mechanical alloying and milling, Prog. Mater. Sci. 46 (2001) 1–184.
16. A.G. Evans, E.A. Charles, Fracture toughness determinations by indentation, J. Am. Ceram. Soc. 59 (1976) 371–372.
17. G.D. Zhan, J. Kuntz, J. Wan, J. Garay, A.K. Mukherjee, A novel processing route to develop a dense nanocrystalline alumina matrix (<100 nm) nanocomposite material, J. Am. Ceram. Soc. 86 (2003) 200–202.
18. C. Domínguez, J. Chevalier, R. Torrecillas, L. Gremillard, G. Fantozzi, Thermomechanical properties and fracture mechanisms of calcium hexaluminate, J. Eur. Ceram. Soc. 21 (2001) 907–917.
19. Y.L. Chin, W.H. Tuan, Contribution of plastic deformation of Ti_3SiC_2 to the crack deflection in the Al_2O_3/Ti_3SiC_2 composites, Mater. Sci. Eng. A 528 (2011) 3270–3274.
20. H. Tang, M.H. Fang, X. Min, X.J. Wang, Z.H. Huang, R.L. Wen, Y.A. Liu, X.W. Wu, Mechanical properties and solid particle erosion behavior of $LaMgAl_{11}O_{19}$-Al_2O_3 ceramic at room and elevated temperatures, J. Am. Ceram. Soc. 99 (2016) 2138–2146.
21. H. Tang, M.H. Fang, C. Tang, Z.H. Huang, H.T. Liu, H.K. Zhu, Y.A. Liu, X.W. Wu, Effect of $LaMgAl_{11}O_{19}$ addition and temperature on the mechanical properties of Al_2O_3-based ceramics, Mater. Sci. Eng. A 655 (2016) 160–167.

Chapter 5: Influence of in-situ synthesized Ba-β-Al_2O_3 on mechanical properties and thermal shock resistance of ZTA/Ba-β-Al_2O_3 composites

5.1 Introduction

Toughening of Al_2O_3 ceramic via in-situ formation of reinforcements with elongated morphologies during sintering has attracted much attention [1-14]. In comparison with the incorporation of fibers, whiskers, and platelets, formation of elongated reinforcements with high aspect ratios through in-situ reactions has many advantages such as less fabrication process, lower costs, and easily obtaining denser and more homogeneous microstructure [4-6]. The formation of these hexaaluminate compounds with elongated morphologies is believed to enhance the fracture toughness of Al_2O_3 matrix composites by crack deflection/bridging.

Al_2O_3/Ba-β-Al_2O_3/ZrO_2 composites with an attractive combination of the Vickers hardness, fracture toughness, and flexure strength have been prepared through reactive sintering of Al_2O_3 and $BaZrO_3$ powders [4,5]. The reaction-formed ZrO_2 exists in monoclinic form (m-ZrO_2) and the improvement in fracture toughness results mainly from the contribution of elongated Ba-β-Al_2O_3 phase. Moreover, Al_2O_3/Ba-β-Al_2O_3 composites can also be synthesized with the help of chemical reactions between Al_2O_3 and $BaCO_3$ [4].

During the past several decades, a considerable amount of research work has incorporated yttria-stabilized zirconia (YSZ) into Al_2O_3 to form zirconia toughened alumina (ZTA) composites [15-17]. ZTA shows excellent mechanical properties such as high strength, fracture toughness, and wear resistance. It has been widely recognized that the improved fracture toughness is mainly attributed to stress-induced transformation toughening and microcrack toughening [15,16].

On the other hand, the coefficient of thermal expansion (CTE) values of Al_2O_3 and YSZ in the temperature range of 25-1000 °C are 8.1×10^{-6} °C^{-1} and 10.3×10^{-6} °C^{-1}, respectively [17]. The CTE mismatch between Al_2O_3 and YSZ may lead to failures of ZTA composites when they are subjected to significant temperature fluctuations or temperature gradient [18-20]. Consequently, thermal shock resistance of ZTA composites is another important factor to be considered. Although there have been many studies on densification behavior, phase evolution, microstructure, and mechanical properties of ZTA composites, no relevant studies regarding the improvement of thermal shock resistance have been reported in the literature.

Considering the positive roles of hexaaluminate compounds in improving the fracture toughness [1-14], flexural strength [5,10,13,14], and thermal shock resistance [21-23] of ceramic materials, in the present work, $BaCO_3$ was introduced into ZTA as an additive to form ZTA/Ba-β-Al_2O_3 composites. The objective of this work was to clarify the effect of in-situ synthesized Ba-β-Al_2O_3 phase on densification behavior, phase evolution, microstructure, mechanical properties, and thermal shock resistance of ZTA/Ba-β-Al_2O_3 composites.

5.2 Experimental procedure

Al_2O_3 (99.99% purity, Taimei Chemicals, Tokyo, Japan), YSZ (3 mol%

Y_2O_3-ZrO_2 (TZ-3Y), 99.9% purity, Tosoh, Tokyo), and $BaCO_3$ (99.95% purity, Kojundo Chemical Lab., Saitama, Japan) powders were used as the starting materials in this study. The average particle sizes of Al_2O_3, YSZ, and $BaCO_3$ powders were 0.16 μm, 50 nm, and 1.5 μm, respectively. 0–8 wt% $BaCO_3$ powder was added to the powder mixtures of 80 wt% Al_2O_3 and 20 wt% YSZ, where the mass ratio of Al_2O_3 to YSZ was fixed to 4:1. The nominal compositions of ZTA/Ba-β-Al_2O_3 composites are shown in Table 5.1.

The raw powders were ball-milled in ethanol using a planetary ball milling system for 10 h at a speed of 200 rpm. Al_2O_3 balls (5 mm in diameter) were used as milling media, and the ball to powder mass ratio was equal to 10:1. After drying at 120 °C for 24 h, the mixtures were calcined at 1000 °C for 1 h to decompose $BaCO_3$ into BaO. The resulting powders were uniaxially pressed into pellets (Φ19 mm × 3 mm) under 20 MPa, followed by cold isostatic pressing under 200 MPa for 2 min. These prepared green compacts were sintered in an electric furnace at 1600 °C for 2 h in air with heating and cooling rates of 400 °C/h.

The density of the sintered samples was measured in distilled water using the Archimedes' principle. Phase identification of the sintered samples and fractured surfaces was performed by X-ray diffraction (XRD) using Cu Kα radiation. The volume amount of monoclinic ZrO_2 phase (V_m) was calculated by the modified Garvie and Nicholson equation [24]. The microstructural observations were conducted by scanning electron microscopy (SEM) on thermally etched (1300 °C for 30 min in air) samples.

Table 5.1 Nominal compositions of ZTA/Ba-β-Al_2O_3 composites (vol%).

Samples	$BaCO_3$ (wt%)	Al_2O_3	3YSZ	Ba-β-Al_2O_3
ZTA0	0	85.94	14.06	0
ZTA2	2	75.72	13.79	10.49
ZTA4	4	65.67	13.44	20.89
ZTA6	6	55.70	13.10	31.20
ZTA8	8	45.84	12.78	41.38

The specimens with dimensions of 3 mm × 4 mm × 36 mm were prepared to measure the flexural strength based on four-point bending method with upper and lower spans of 10 and 30 mm, respectively, and the crosshead speed was 0.5 mm/min. Each specimen was polished with diamond paste (3 μm) and the edges were chamfered at an angle of 45^o. The fracture toughness was determined by a single-edge-notched-beam (SENB) method with a span of 20 mm and a crosshead speed of 0.05 mm/min [25]. The dimensions of specimens were 2.5 mm × 5 mm × 25 mm, and a notch with depth of 2.5 mm and width of 0.3 mm was introduced. In addition, thermal shock tests were performed, where specimens were heated from room temperature to 1100 °C with a heating rate of 400 °C/h in air. After heating at 1100 °C for 15 min, the specimens were taken out and immersed into water immediately. The thermal shock resistance was evaluated by comparing the residual flexural strength after thermal shock tests. At least 8 specimens were performed for each testing condition in both bending and thermal shock tests, and the average values were reported. Vickers hardness tests were performed on the polished surfaces using a Vickers diamond indenter with a load of 98 N for 15 s, and the reported values of hardness were obtained from 10 indentations.

5.3 Results and discussion

5.3.1 Densification behavior

As an example, the XRD patterns of mixed and calcined ZTA8 powders are shown Fig. 5.1. The peaks of Al_2O_3, $BaCO_3$, and ZrO_2 (including monoclinic and tetragonal forms) were observed in the mixed powder. When the powder mixture was calcined at 1000 °C, the peaks of $BaCO_3$ almost disappeared. Instead, barium monoaluminate ($BaO\cdot Al_2O_3$) was formed as one of main phases. This indicates that $BaCO_3$ has been decomposed into BaO, which further reacts with Al_2O_3 to form $BaO\cdot Al_2O_3$ during calcining. In addition, the relative intensity of *m*-ZrO_2 peaks decreased sharply.

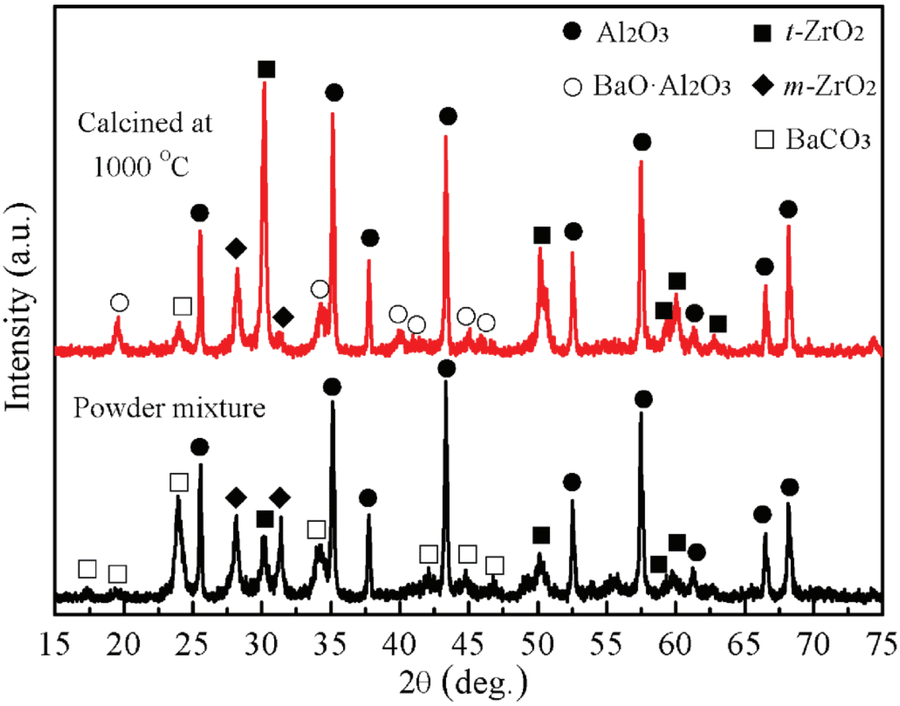

Fig. 5.1 XRD patterns of mixed and calcined ZTA8 powders.

The relative density of the sintered ZTA/Ba-β-Al_2O_3 samples is plotted in Fig. 5.2 as a function of $BaCO_3$ content. The relative density significantly decreased with increasing $BaCO_3$ content. Since the amount of Ba-β-Al_2O_3 in ZTA/Ba-β-Al_2O_3 composites depends on $BaCO_3$ content (Table 5.1), the density decrease with increasing $BaCO_3$ content is the result of formation of more Ba-β-Al_2O_3 phase. Our experimental results have demonstrated that small-sized $BaO\cdot Al_2O_3$ particles were formed during the calcining of Al_2O_3 and $BaCO_3$ powder mixtures at 1000 °C. The existence of $BaO\cdot Al_2O_3$ particles in the initial stage of sintering and subsequent formation of Ba-β-Al_2O_3 phase undoubtedly inhibit the densification of the Al_2O_3 matrix. Furthermore, as is known, Ba-β-Al_2O_3 phase with a layered structure is difficult to be densified by conventional solid-state reaction sintering due to the suppressed interlayer diffusion of atoms [7]. Another reason is related to the elongated morphology of Ba-β-Al_2O_3 phase, because its network restricts the densification of the composites.

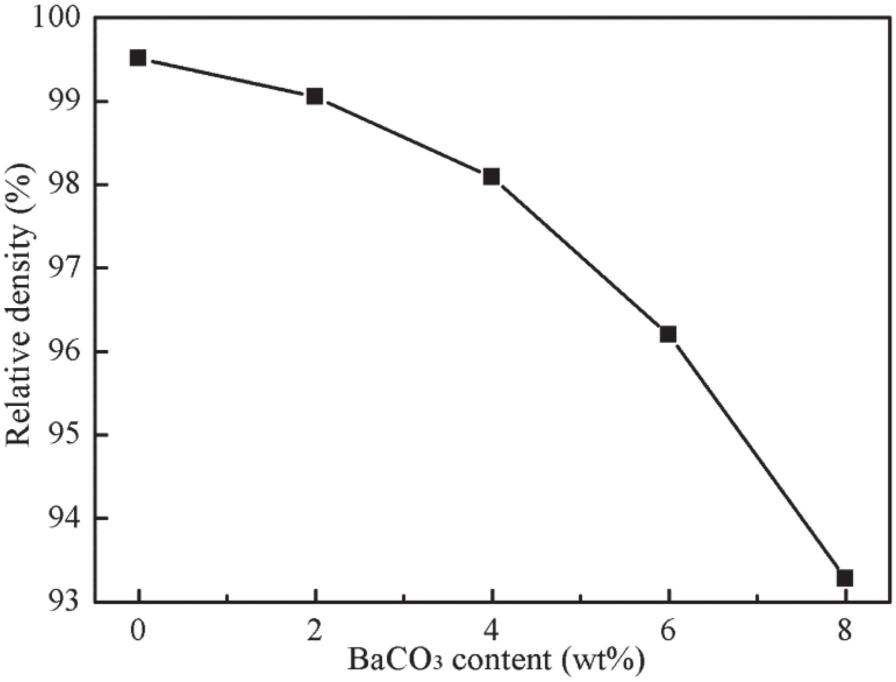

Fig. 5.2 Relative density of sintered ZTA/Ba-β-Al_2O_3 samples as a function of $BaCO_3$ content.

5.3.2 Phase analysis and microstructure

The XRD patterns of the sintered ZTA/Ba-β-Al_2O_3 samples are shown in Fig. 5.3. The ZTA sample without $BaCO_3$ addition (ZTA0) showed strong peaks of Al_2O_3 and tetragonal ZrO_2 (t-ZrO_2) with a small amount of m-ZrO_2. Similar results have been reported in the literature [26-28]. For the $BaCO_3$-added samples, Al_2O_3, Ba-β-Al_2O_3, and ZrO_2 (including m-ZrO_2 and t-ZrO_2) phases were detected, and relative intensity of the peaks corresponding to Ba-β-Al_2O_3 phase became larger with increasing $BaCO_3$ content. The volume percentages of m-ZrO_2 phase, calculated using the XRD data measured on polished surfaces of the sintered samples, are shown in Table 5.2. The amount of m-ZrO_2 phase in sintered samples gradually increased with increasing $BaCO_3$ content. Owing to lower Vickers hardness and Young's modulus of aluminates than those of Al_2O_3 [5,7], as well as a decreased density with the increase in $BaCO_3$ content, the subjected constraints of the ZrO_2 from the surroundings are reduced.

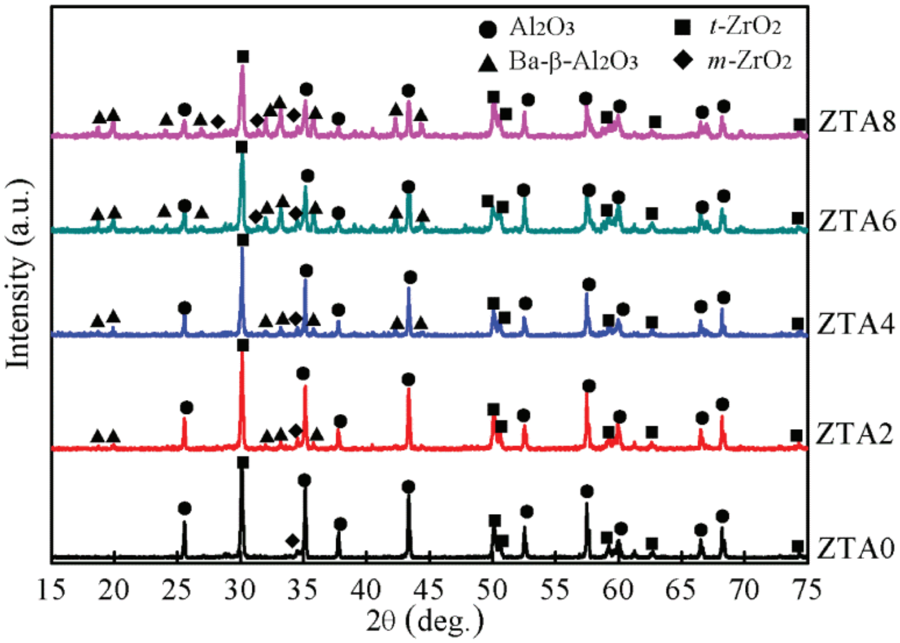

Fig. 5.3 XRD patterns of ZTA/Ba-β-Al_2O_3 samples sintered at 1600 °C.

Table 5.2 Volume amounts of m-ZrO_2 phase measured on polished and fractured surfaces of ZTA/Ba-β-Al_2O_3 samples (vol%).

Samples	Volume amounts of m-ZrO_2 on polished surfaces	Volume amounts of m-ZrO_2 on fractured surfaces	Volume amounts of $t \rightarrow m$ transformation
ZTA0	4.26	5.69	1.43
ZTA2	4.66	10.65	5.99
ZTA4	6.66	12.94	6.28
ZTA6	9.63	11.60	1.97
ZTA8	11.25	12.37	1.12

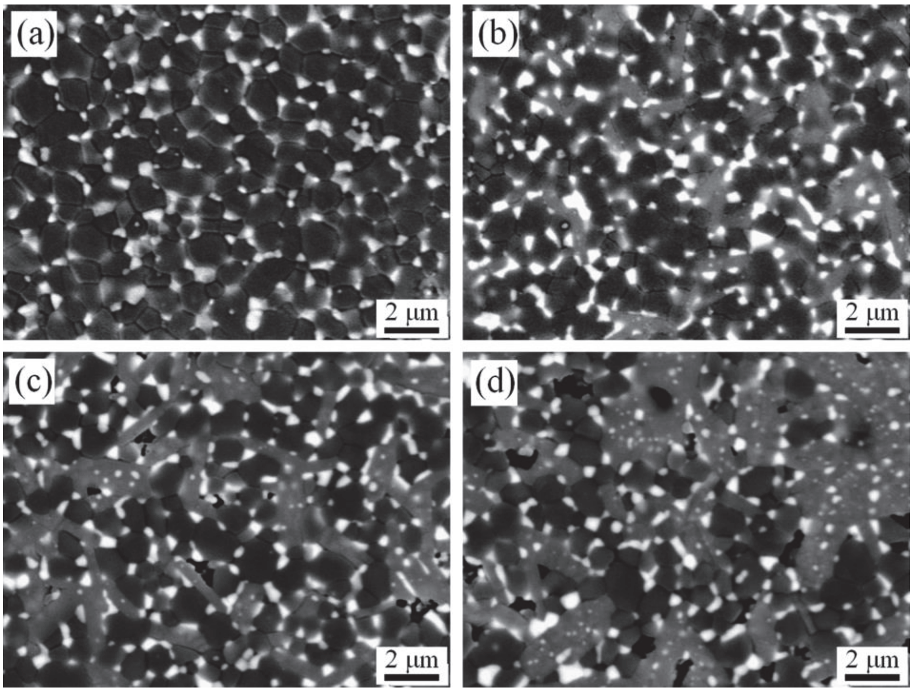

Fig. 5.4 BSE images of thermally etched samples sintered at 1600 °C. (a) Without $BaCO_3$, (b) 4 wt% $BaCO_3$, (c) 6 wt% $BaCO_3$, and (d) 8 wt% $BaCO_3$.

Fig. 5.4 shows the backscattered electron (BSE) images of the thermally etched samples. Both white ZrO_2 particles and gray Ba-β-Al_2O_3 with a platelet morphology were homogeneously distributed in the Al_2O_3 matrix with a dark contrast. As $BaCO_3$ content increased, the coarsening of Ba-β-Al_2O_3 phase was observed, which is presumably attributed to the coalescence of neighboring Ba-β-Al_2O_3. In fact, it is difficult to identify the morphology of Ba-β-Al_2O_3 phase in ZTA8 sample. Moreover, more pores remained in the samples with increasing $BaCO_3$ content.

5.3.3 Mechanical properties and thermal shock resistance

Fig. 5.5 shows the Vickers hardness and fracture toughness of the sintered ZTA/Ba-β-Al_2O_3 samples as a function of $BaCO_3$ content. As $BaCO_3$ content increased, the Vickers hardness monotonously decreased. This is mainly attributed to lower density values of the sintered samples (Fig. 5.2) due to formation of more Ba-β-Al_2O_3 phase. In addition, Ba-β-Al_2O_3 phase has a lower hardness value [5]. As shown in Fig. 5.5, the fracture toughness was enhanced with increasing $BaCO_3$ content up to 4 wt%, followed by a decrease when $BaCO_3$ content was further increased. A maximum value of fracture toughness (6.4 MPa $m^{1/2}$) was obtained in the ZTA/Ba-β-Al_2O_3 composite with 4 wt% $BaCO_3$ addition. As an example, the propagation behavior of cracks in ZTA4 sample (4 wt% $BaCO_3$ addition) is shown in Fig. 5.6. Crack deflection (indicated by arrows “a”) along the interfaces of Ba-β-Al_2O_3/Al_2O_3, ZrO_2/Al_2O_3, and ZrO_2/Ba-β-Al_2O_3 as well as crack bridging (indicated by arrows “b”) could be observed. Consequently, the increased fracture surface areas and total energy consumed during crack propagation lead to the enhancement of fracture toughness. Moreover, some of the elongated Ba-β-Al_2O_3 was observed to fracture transgranularly (indicated by arrows “c”) due to strong interfaces formed by in-situ reactions between Al_2O_3 and $BaCO_3$ at high temperatures, and relatively lower Young's modulus of Ba-β-Al_2O_3 than that of Al_2O_3. Similar phenomenon has also been reported by Domínguez et al. [29]. It is considered that the crack propagation inside Ba-β-Al_2O_3 phase probably occurs along the easy cleavage planes of {0001} [30,31].

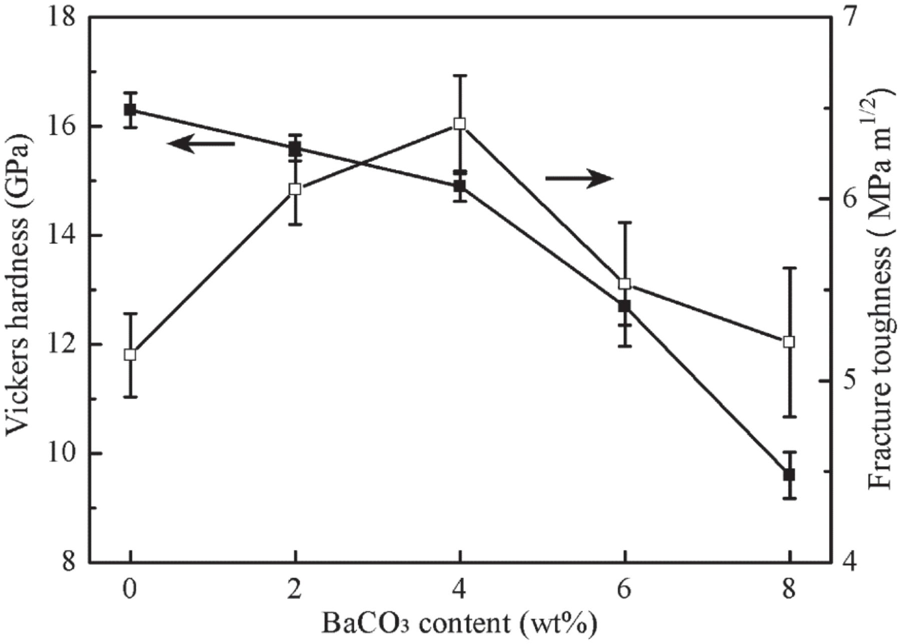

Fig. 5.5 Vickers hardness and fracture toughness of ZTA/Ba-β-Al_2O_3 samples as a function of $BaCO_3$ content.

The volume percentages of *m*-ZrO_2 phase measured on fractured surfaces and transformed ZrO_2 amounts during fracture were also included in Table 5.2. As compared to ZTA sample without Ba-β-Al_2O_3 phase, the ZTA/Ba-β-Al_2O_3 composites with 2 and 4 wt% $BaCO_3$ additions exhibited higher *t*→*m* transformation amounts during fracture. A further increase in $BaCO_3$ content, *e.g.*, 6 and 8 wt%, resulted in decrease in transformability of *t*-ZrO_2, which might be associated with formation of more Ba-β-Al_2O_3 and lower density of the composites. It should be noted that the residual stresses, generated during cooling from the sintering temperature due to thermal expansion anisotropy [32], may promote the martensitic transformation of ZrO_2. The variation in transformation amount of *t*-ZrO_2 during fracture is in good agreement with the change in fracture toughness shown in Fig. 5.5, indicating that martensitic transformation toughening of ZrO_2 is one of the important mechanisms. The improved fracture toughness of the ZTA/Ba-β-Al_2O_3 composites is the result of a multiple toughening effect including martensitic transformation of ZrO_2 and crack deflection/bridging.

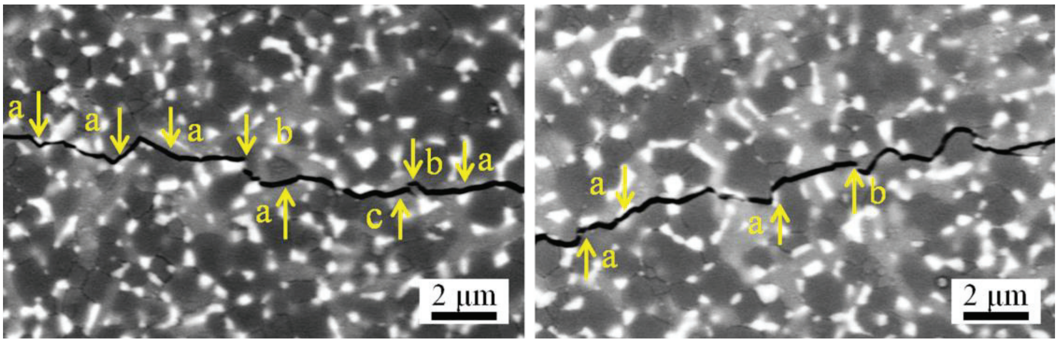

Fig. 5.6 SEM images showing crack propagation behavior in ZTA4 sample.

Fig. 5.7 shows the flexural strength at room temperature (RT) and residual strength after thermal shock tests of ZTA/Ba-β-Al_2O_3 samples as a function of $BaCO_3$ content. The ZTA/Ba-β-Al_2O_3 sample with 2 wt% $BaCO_3$ exhibited a slightly higher flexural strength than ZTA sample, which is probably attributed to dispersion strengthening of Ba-β-Al_2O_3 phase. The flexural strength significantly decreased with further increasing $BaCO_3$ content at >2 wt% due to density decrease of the composites (Fig. 5.2) and coarsening of Ba-β-Al_2O_3 phase. After thermal shock tests, the residual strength of all ZTA/Ba-β-Al_2O_3 samples was higher than that of ZTA, although the flexural strength of ZTA/Ba-β-Al_2O_3 samples with >2 wt% $BaCO_3$ was lower than that of ZTA.

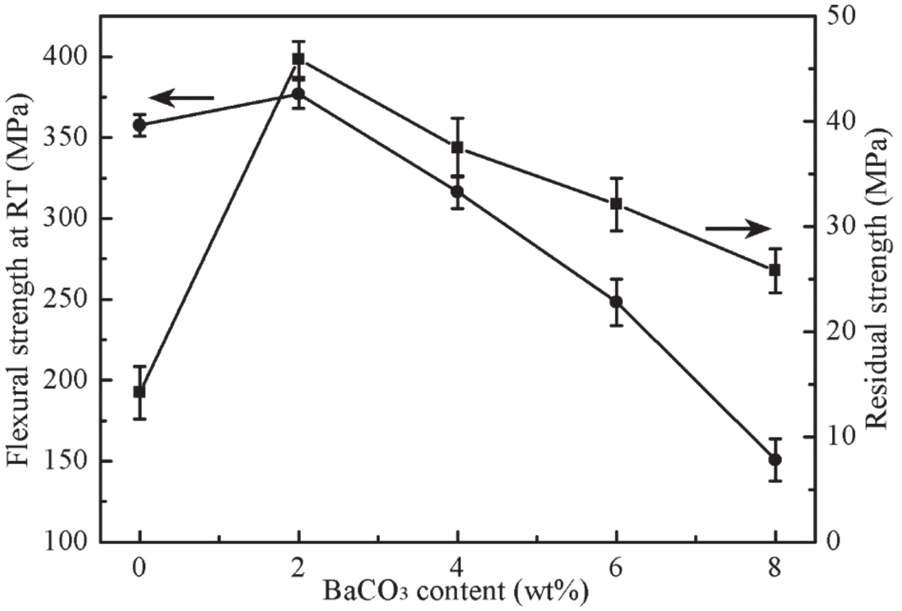

Fig. 5.7 Flexural strength at room temperature and residual strength after thermal shock tests of ZTA/Ba-β-Al_2O_3 samples as a function of $BaCO_3$ content.

The BSE images of ZTA0 and ZTA4 samples after thermal shock tests are shown in Fig. 5.8. The microcracks were mainly located at the interfaces between Al_2O_3 and YSZ (pointed by the arrows in Fig. 5.8(a)) on the polished surfaces of thermal shocked ZTA0 sample, which is mainly due to the CTE mismatch of Al_2O_3 and YSZ. As for thermal shocked ZTA4 sample, limited microcracks occurred at Al_2O_3/YSZ interfaces, and the cracks within Ba-β-Al_2O_3 platelets were observed (pointed by the arrows in Fig. 5.8(b)). The Ba-β-Al_2O_3 phase with a hexagonal structure would be greatly expanded along *c*-axis due to its highly anisotropic thermal expansion behavior. When the sintered samples are quenched in water from 1100 °C, considerable contraction is accumulated along *c*-axis. In addition, the bonding between basal planes in Ba-β-Al_2O_3 phase is weak. These result in formation and propagation of cracks within Ba-β-Al_2O_3 platelets.

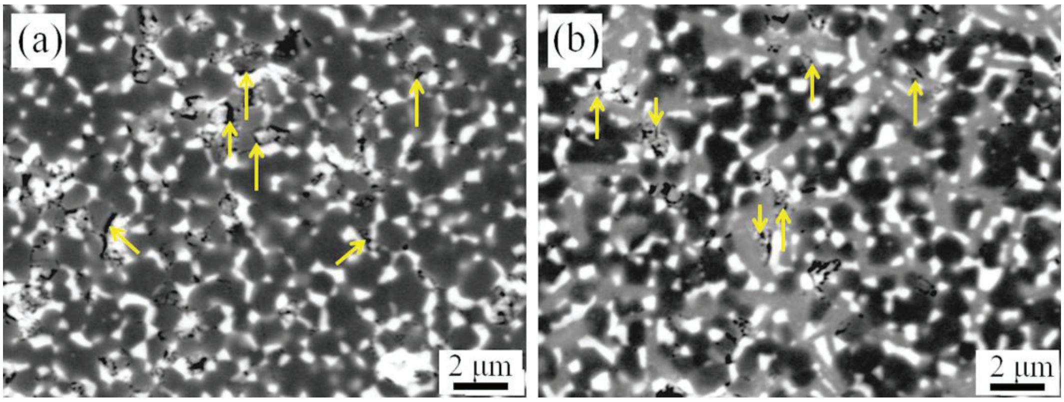

Fig. 5.8 BSE images of (a) ZTA0 and (b) ZTA4 samples after thermal shock tests.

Fig. 5.9 shows the SEM images (secondary electron mode) of the fracture surfaces of ZTA0 and ZTA4 samples after thermal shock tests. The composites exhibited a mixed mode of intergranular and transgranular fracture. Moreover, the fraction of intergranular fracture is much higher than that of transgranular fracture in ZTA0 sample. This is due to the fact that most microcracks preferentially propagated along the interfaces between Al_2O_3 and YSZ after thermal shock tests. For ZTA4 sample, the transgranular fracture becomes the dominant crack propagation mechanism when cracks pass through Ba-β-Al_2O_3 phase (indicated by the arrows in Fig. 5.9(b)).

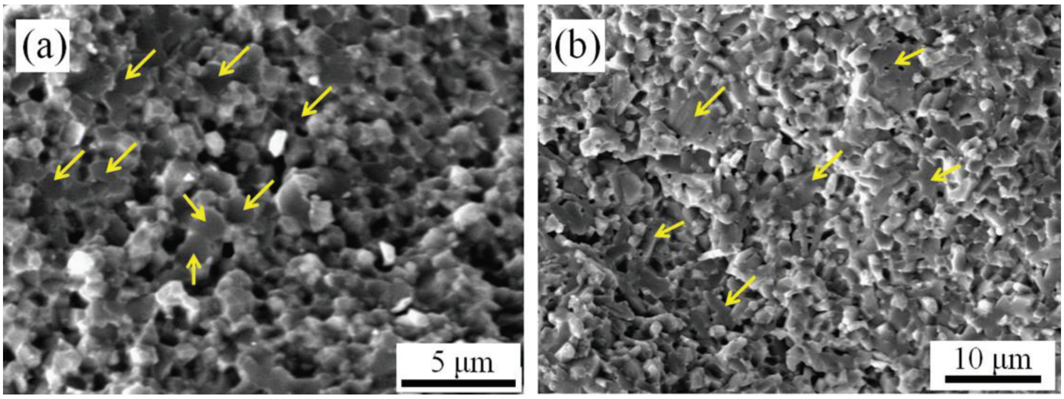

Fig. 5.9 SEM images showing fracture surfaces of (a) ZTA0 and (b) ZTA4 samples after thermal shock tests.

From the above results, it is believed that the improvement in thermal shock resistance of ZTA/Ba-β-Al_2O_3 composites is mainly ascribed to two aspects:

(1) The Ba-β-Al_2O_3 phase would be greatly expanded along *c*-axis due to its highly anisotropic thermal expansion behavior. The formation and propagation of cracks within Ba-β-Al_2O_3 platelets occur in thermal shocked ZTA/Ba-β-Al_2O_3 composites, which can dissipate the energy associated with crack propagation. Furthermore, the elongated Ba-β-Al_2O_3 phase also results in crack deflection/bridging.

(2) Higher toughness is beneficial to inhibiting crack growing and propagating [17,33,34]. In addition, the homogeneously distributed small pores in ZTA/Ba-β-Al_2O_3 composites could act as crack stoppers by crack tip blunting [35].

5.4 Conclusions

ZTA/Ba-β-Al_2O_3 composites were fabricated by solid-state reaction sintering of Al_2O_3, YSZ, and $BaCO_3$ powders, and the effect of in-situ synthesized Ba-β-Al_2O_3 phase on densification behavior, phase evolution, microstructure, mechanical properties, and thermal shock resistance was investigated. Based on the experimental results, several conclusions can be drawn:

(1) The relative density of ZTA/Ba-β-Al_2O_3 composites decreased with increasing $BaCO_3$ content, as a result of in-situ formation of elongated Ba-β-Al_2O_3 phase. The elongated Ba-β-Al_2O_3 phase was homogeneously distributed in ZTA matrix. Moreover, preferred orientational growth due to faster diffusion of Ba^{2+} along basal planes than along *c*-axis results in the formation of Ba-β-Al_2O_3 phase with high aspect ratios.

(2) The Vickers hardness and flexural strength of ZTA/Ba-β-Al_2O_3 composites decreased with the increase in $BaCO_3$ content except for the composite with 2 wt% $BaCO_3$ addition, where the flexural strength was slightly higher than that of ZTA sample. The decreased Vickers hardness and flexural strength mainly result from the lower density values at larger $BaCO_3$ contents.

(3) ZTA/Ba-β-Al_2O_3 composites exhibited enhanced fracture toughness, which is due to the synergistic toughening effects of martensitic transformation of ZrO_2 and crack deflection/bridging. A maximum value of fracture toughness (6.4 MPa $m^{1/2}$) was obtained in the ZTA/Ba-β-Al_2O_3 composite with 4 wt% $BaCO_3$ addition.

(4) After thermal shock tests, the residual strength of ZTA/Ba-β-Al_2O_3 composites was higher than that of ZTA, and reached a maximum value (45.9 MPa) at 2 wt% $BaCO_3$. The enhancement in thermal shock resistance of ZTA/Ba-β-Al_2O_3 composites is associated with the formation of Ba-β-Al_2O_3 phase with a hexagonal structure, improved fracture toughness, and homogeneously distributed small pores.

References

1. A.J. Sánchez-Herencia, R. Moreno, C. Baudín, Fracture behaviour of alumina–calcium hexaluminate composites obtained by colloidal processing, J. Eur. Ceram. Soc. 20 (2000) 2575–2583.
2. Z.D.I. Sktani, A.Z.A. Azhar, M.M. Ratnam, Z.A. Ahmad, The influence of in-situ formation of hibonite on the properties of zirconia toughened alumina (ZTA) composites, Ceram. Int. 40 (2014) 6211–6217.
3. D. Asmi, I.M. Low, Processing of an in-situ layered and graded alumina/calcium-hexaluminate composite: physical characteristics, J. Eur. Ceram. Soc. 18 (1998) 2019–2024.
4. Z.C. Chen, S. Nugroho, M. Ezumi, T. Akao, T. Onda, In situ synthesis of alumina-matrix oxide/oxide composites by reactive sintering, Mater. Sci. Eng. A 557 (2012) 59–68.
5. Z.C. Chen, K.K. Chawla, M. Koopman, Microstructure and mechanical properties of in situ synthesized alumina/Ba-β-alumina/zirconia composites, Mater. Sci. Eng. A 367 (2004) 24–32.
6. M. Yasuoka, K. Hirao, M.E. Brito, S. Kanzaki, High-strength and high-fracture-toughness ceramics in the $Al_2O_3/LaAl_{11}O_{18}$ systems, J. Am. Ceram. Soc. 78 (1995) 1853–1856.
7. Z. Negahdari, M. Willert-Porada, C. Pfeiffer, Mechanical properties of dense to porous alumina/lanthanum hexaaluminate composite ceramics, Mater. Sci. Eng. A 527 (2010) 3005–3009.

8. R. Guo, D. Guo, Y. Chen, Z. Yang, Q. Yuan, In situ formation of $LaAl_{11}O_{18}$ rodlike particles in ZTA ceramics and effect on the mechanical properties, Ceram. Int. 28 (2002) 699–704.
9. K. Vishista, F.D. Gnanam, Microstructural development of $SrAl_{12}O_{19}$ in alumina-strontia composites, J. Eur. Ceram. Soc. 29 (2009) 77–83.
10. K. Vishista, F.D. Gnanam, Effect of strontia on the densification and mechanical properties of sol-gel alumina, Ceram. Int. 32 (2006) 917–922.
11. R.A. Cutler, R.J. Mayhew, K.M. Prettyman, A.V. Virkar, High-toughness Ce-TZP/Al_2O_3 ceramics with improved hardness and strength, J. Am. Ceram. Soc. 74 (1991) 179–186.
12. P.L. Chen, I.W. Chen, In-situ alumina/aluminate platelet composites, J. Am. Ceram. Soc. 75 (1992) 2610–2612.
13. H. Tang, M.H. Fang, X. Min, X.J. Wang, Z.H. Huang, R.L. Wen, Y.A. Liu, X.W. Wu, Mechanical properties and solid particle erosion behavior of $LaMgAl_{11}O_{19}$-Al_2O_3 ceramic at room and elevated temperatures, J. Am. Ceram. Soc. 99 (2016) 2138–2146.
14. H. Tang, M.H. Fang, C. Tang, Z.H. Huang, H.T. Liu, H.K. Zhu, Y.A. Liu, X.W. Wu, Effect of $LaMgAl_{11}O_{19}$ addition and temperature on the mechanical properties of Al_2O_3-based ceramics, Mater. Sci. Eng. A 655 (2016) 160–167.
15. W.H. Tuan, R.Z. Chen, T.C. Wang, C.H. Cheng, P.S. Kuo, Mechanical properties of Al_2O_3/ZrO_2 composites, J. Eur. Ceram. Soc. 22 (2002) 2827–2833.
16. R.H.J. Hannink, P.M. Kelly, B.C. Muddle, Transformation toughening in

zirconia-containing ceramics, J. Am. Ceram. Soc. 83 (2000) 461–487.

17. L. Liu, K. Maeda, T. Onda, Z.C. Chen, Microstructure and improved mechanical properties of Al_2O_3/Ba-β-Al_2O_3/ZrO_2 composites with YSZ addition, J. Eur. Ceram. Soc. 38 (2018) 5113–5121.
18. D.L. Cai, D.C. Jia, Z.H. Yang, Q.S. Zhu, V. Ocelik, I.D. Vainchtein, J.T.M. De Hosson, Y. Zhou, Effect of magnesium aluminum silicate glass on the thermal shock resistance of BN matrix composite ceramics, J. Am. Ceram. Soc. 100 (2017) 2669–2678.
19. M. Kašiarová, P. Tatarko, P. Burik, J. Dusza, P. Šajgalík, Thermal shock resistance of Si_3N_4 and Si_3N_4-SiC ceramics with rare-earth oxide sintering additives, J. Eur. Ceram. Soc. 34 (2014) 3301–3308.
20. Z. Wang, P. Zhou, Z.J. Wu, Effect of surface oxidation on thermal shock resistance of ZrB_2-SiC-ZrC ceramic at temperature difference from 800 to 1900 °C, Corros. Sci. 98 (2015) 233-239.
21. X.Q. Cao, Y.F. Zhang, J.F. Zhang, X.H. Zhong, Y. Wang, H.M. Ma, Z.H. Xu, L.M. He, F. Lu, Failure of the plasma-sprayed coating of lanthanum hexaluminate, J. Eur. Ceram. Soc. 28 (2008) 1979–1986.
22. X.L. Chen, Y.F. Zhang, X.H. Zhong, Z.H. Xu, J.F. Zhang, Y.L. Cheng, Y. Zhao, Y.J. Liu, X.Z. Fan, Y. Wang, H.M. Ma, X.Q. Cao, Thermal cycling behaviors of the plasma sprayed thermal barrier coatings of hexaluminates with magnetoplumbite structure, J. Eur. Ceram. Soc. 30 (2010) 1649–1657.
23. X.L. Chen, Y. Zhao, W.Z. Huang, H.M. Ma, B.L. Zou, Y. Wang, X.Q. Cao,

Thermal aging behavior of plasma sprayed $LaMgAl_{11}O_{19}$ thermal barrier coating, J. Eur. Ceram. Soc. 31 (2011) 2285–2294.

24. R.C. Garvie, P.S. Nicholson, Phase analysis in zirconia systems, J. Am. Ceram. Soc. 55 (1972) 303–305.
25. G.V. Guinea, J.Y. Pastor, J. Planas, M. Elices, Stress intensity factor, compliance and CMOD for a general three-point-bend beam, Int. J. Fract. 89 (1998) 103–116.
26. X.Q. Xu, X.X. Hu, S. Ren, H.T. Geng, H.Y. Du, J.C. Liu, Fine grained Al_2O_3-ZrO_2 (Y_2O_3) ceramics by controlled crystallization of amorphous phase, J. Eur. Ceram. Soc. 36 (2016) 1791–1796.
27. W.M. Ma, L. Wen, R.G. Guan, X.D. Sun, X.K. Li, Sintering densification, microstructure and transformation behavior of $Al_2O_3/ZrO_2(Y_2O_3)$ composites, Mater. Sci. Eng. A 477 (2008) 100–106.
28. A.Z.A. Azhar, L.C. Choong, H. Mohamed, M.M. Ratnam, Z.A. Ahmad, Effects of Cr_2O_3 addition on the mechanical properties, microstructure and wear performance of zirconia-toughened-alumina (ZTA) cutting inserts, J. Alloys Compd. 513 (2012): 91–96.
29. C. Domínguez, J. Chevalier, R. Torrecillas, L. Gremillard, G. Fantozzi, Thermomechanical properties and fracture mechanisms of calcium hexaluminate, J. Eur. Ceram. Soc. 21 (2001) 907–917.
30. M.K. Cinibulk, R.S. Hay, Textured magnetoplumbite fiber-matrix interphase derived from sol-gel fiber coatings, J. Am. Ceram. Soc. 79 (1996) 1233–1246.
31. M.K. Cinibulk, Hexaluminates as a cleavable fiber–matrix interphase: synthesis,

texture development, and phase compatibility, J. Eur. Ceram. Soc. 20 (2000) 569–582.

32. V. Tvergaard, J.W. Hutchinson, Microcracking in ceramics induced by thermal expansion or elastic anisotropy, J. Am. Ceram. Soc. 71 (1988) 157–166.
33. L. Xu, M. Chen, L.Y. Jin, X.L. Yin, N. Wang, L. Liu, Effect of ZrO_2 addition on densification and mechanical properties of $MgAl_2O_4$-$CaAl_4O_7$-$CaAl_{12}O_{19}$ composite, J. Am. Ceram. Soc. 98 (2015) 4117–4123.
34. L. Liu, M. Chen, L. Xu, X.L. Yin, W.J. Sun, Effect of BaO addition on densification and mechanical properties of Al_2O_3-MgO-CaO refractories, Metals 6 (2016) 84.
35. Z.Y. Deng, J.H. She, Y. Inagaki, J.F. Yang, T. Ohji, Y. Tanaka, Reinforcement by crack-tip blunting in porous ceramics. J. Eur. Ceram. Soc. 24 (2004) 2055–2059.

Chapter 6: Microstructure and promoted densification of Ti^{4+}-doped calcium hexaaluminate ceramics

6.1 Introduction

Calcium hexaaluminate ($CaAl_{12}O_{19}$, or CA_6) is the most alumina-rich intermediate compound of the $CaO–Al_2O_3$ system, and its theoretical density is 3.79 g/cm^3 [1-6]. CA_6 has a magnetoplumbite structure (hexagonal, $P6_3/mmc$), which is composed of layered spinel blocks $[Al_{11}O_{16}]^+$ separated by mirror planes $[CaAlO_3]^-$ [7-10]. CA_6 is one of the promising ceramic materials for refractory applications because of the resistance to slag corrosion, thermal shock, and creep [11-15]. In addition, the in-situ formation of CA_6 with high aspect ratios has been widely used to enhance the fracture toughness of Al_2O_3 matrix composites due to crack deflection and crack bridging [16-20]. The layered magnetoplumbite structure makes CA_6 phase difficult to be densified by solid-state reaction sintering, which is ascribed to the suppressed interlayer diffusion of ions [8,21]. Thus, the open porosity of CA_6 sintered at 1600 °C was high (higher than 20%) [1,2,22], leading to low strength and poor molten slag resistance.

Spark plasma sintering (SPS) has been used to obtain dense CA_6 by optimizing sintering parameters [23]. By conventional reaction sintering, the densification of CA_6 can be enhanced by creating defects along *c*-axis (perpendicular to basal plane). The length in short-axis direction of the CA_6 was increased by substituting Ba^{2+} for Ca^{2+}, whereas the open porosity value (18.5%) of the doped CA_6 is still large [6]. For high-alumina refractory castables based on the Al_2O_3–MgO–CaO system, the densification of the composites can be promoted by doping Ti^{4+} [24-27].

In this study, CA_6 ceramics were fabricated by solid-state reaction sintering of Al_2O_3 and $CaCO_3$ powder mixtures. The aim was to fabricate denser CA_6 ceramics and investigate the influence of TiO_2 addition on densification behavior, phase evolution, and microstructure of CA_6 ceramics.

6.2 Experimental procedure

Al_2O_3 (average particle size 0.16 μm, 99.99% purity; Taimei Chemicals, Tokyo, Japan), $CaCO_3$ (5 μm, 99% purity; Kojundo Chemical Lab., Saitama, Japan), and TiO_2 (0.2 μm, 99% purity; IoLiTec, Heilbronn, Germany) powders were used as the starting materials. Al_2O_3 and $CaCO_3$ powders were used to synthesize CA_6 ceramics. 0–4 wt% TiO_2 powder was added to the above-mentioned powder mixtures. The raw powders were milled in ethanol for 24 h with Al_2O_3 balls as milling media, and then the slurries were dried at 120 °C for 24 h. After drying, the pellets (Φ19 mm × 3 mm) were prepared by uniaxial pressing at 20 MPa. The prepared green compacts were sintered at 1600 °C for 2 h in air, and the heating/cooling rate was 400 °C/h.

The open porosity of the sintered samples was measured in distilled water using the Archimedes' principle. Phase identification was performed by X-ray diffraction (XRD; RINT-TTR III, Rigaku, Japan) using Cu Kα radiation. The microstructural observations and compositional analyses were performed by scanning electron microscopy (SEM; JXA-9800RL, JEOL, Japan) and energy-dispersive X-ray spectroscopy (EDS), respectively.

6.3 Results and discussion

6.3.1 Densification behavior and phase analysis

The open porosity of CA_6 samples with different TiO_2 contents is shown in Table 6.1. The network structure and poor sintering ability of CA_6, resulting from its suppressed interlayer diffusion of ions, were responsible for the high open porosity (22.5%) of the pure CA_6 [21,28]. CA_6 samples with a higher TiO_2 content exhibited lower open porosity, indicating that the addition of TiO_2 promotes the densification of CA_6 ceramics.

Table 6.1 Open porosity and morphology of CA_6 ceramics.

Samples	Open porosity (%)	Length (μm)	Width (μm)	Aspect ratio
CA_6	22.5	4.7	0.9	5.22
CA_6-2T	9.8	8.3	3.8	2.18
CA_6-4T	8.2	8.4	3.9	2.15

Fig. 6.1(a) shows the XRD patterns of the CA_6 samples sintered at 1600 °C. For the sample without TiO_2, only CA_6 phase was formed. No peaks of $CaCO_3$, Al_2O_3 or intermediate phases, such as $Ca_3Al_2O_6$, $Ca_{12}Al_{14}O_{33}$, $CaAl_2O_4$, and $CaAl_4O_7$, were detected within the detection limit of the XRD analysis. For the sample with 2 wt% TiO_2, the peaks of CA_6 showed a shift to lower 2θ values, and the peaks of Al_2O_3 were also observed. The substitutions of V^{5+}, Fe^{3+}, Cr^{3+}, Mg^{2+}, and Ti^{4+} for Al^{3+} in CA_6 have been reported in the literature [29]. It is reasonable to consider that Ti^{4+} has dissolved into the crystal lattices of CA_6 by replacing Al^{3+}. Compared to 2 wt%

TiO_2-added sample, the peak intensities of CA_6 tended to decrease when 4 wt% TiO_2 was added. From the phase diagram of Al_2O_3–TiO_2–CaO system [30], $CaTiO_3$ was formed due to the reactions between TiO_2 and CaO. Consequently, the amounts of Al_2O_3 and $CaTiO_3$ increase, while CA_6 decreases slightly. As shown in Fig. 6.1(c), both lattice parameters a and c increased up to 2 wt% TiO_2-added sample, which is ascribed to the larger ionic radius of Ti^{4+} than that of Al^{3+} (ionic radii of Al^{3+} and Ti^{4+} are 0.053 and 0.060 nm, respectively).

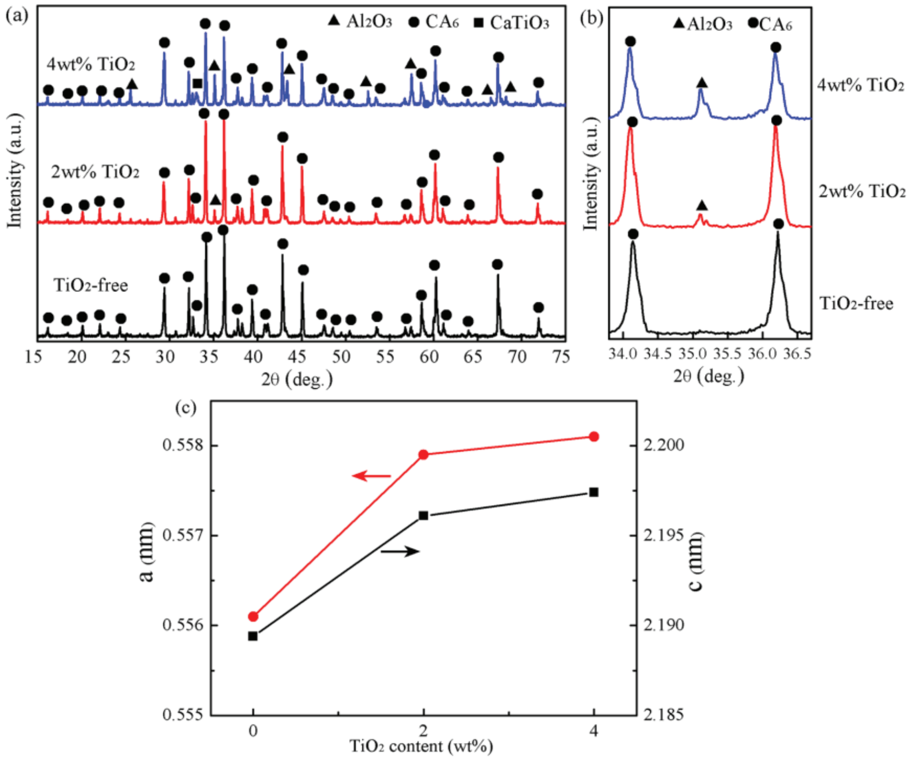

Fig. 6.1 (a) XRD patterns, (b) enlarged XRD patterns in selected 2θ range, and (c) the measured lattice parameters of CA_6 with different TiO_2 contents.

6.3.2 Microstructure characterization

To reveal the amounts, sizes, and distributions of the pores within the CA_6 ceramics as well as the morphologies of the CA_6 grains, the microstructure of the sintered samples were observed. The low-magnification (overview) and high-magnification (detailed) SEM images (backscattered electron mode) of the thermally etched CA_6 samples with different TiO_2 contents are shown in Fig. 6.2 and Fig. 6.3, respectively. As shown in Fig. 6.2(a), the sample without TiO_2 addition exhibited porous CA_6 microstructure, in which trace amount of Al_2O_3 with a dark contrast was distributed due to uncompleted reactions between Al_2O_3 and $CaCO_3$. When Ti^{4+} was doped (Fig. 6.2(b) and 6.2(c)), the porosity decreased significantly, and the amounts of Al_2O_3 and $CaTiO_3$ (pointed by the arrows in Fig. 6.2(b) and 6.2(c)) increased with increasing TiO_2 content, which is attributed to the reactions between CaO and TiO_2. Furthermore, the Al_2O_3 particles showed larger sizes.

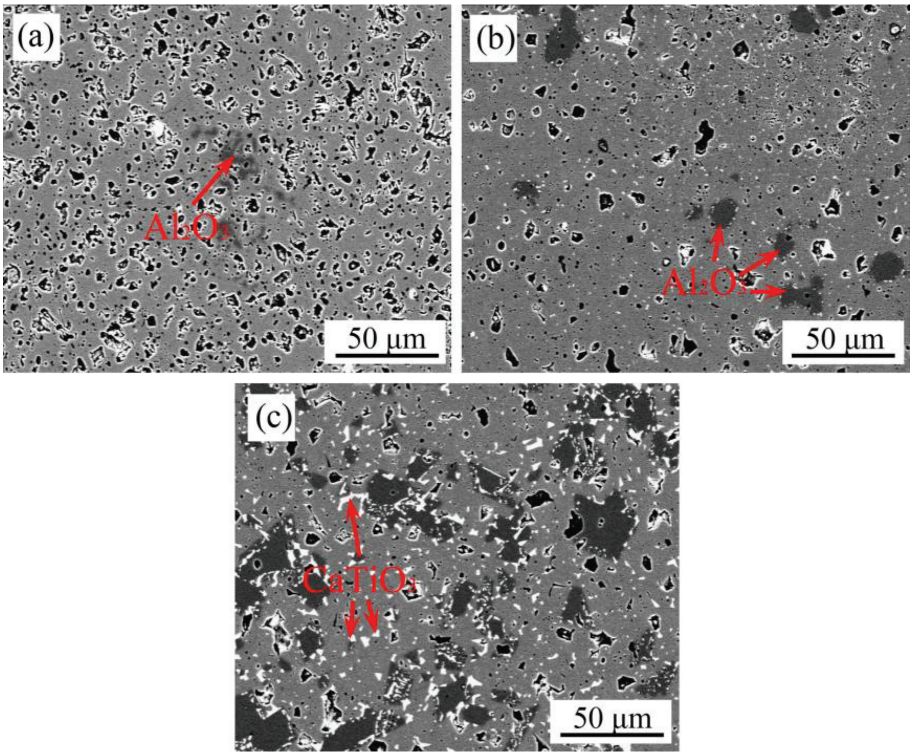

Fig. 6.2 Low-magnification SEM images of CA_6 samples with different TiO_2 contents. (a) 0, (b) 2 wt%, and (c) 4 wt%.

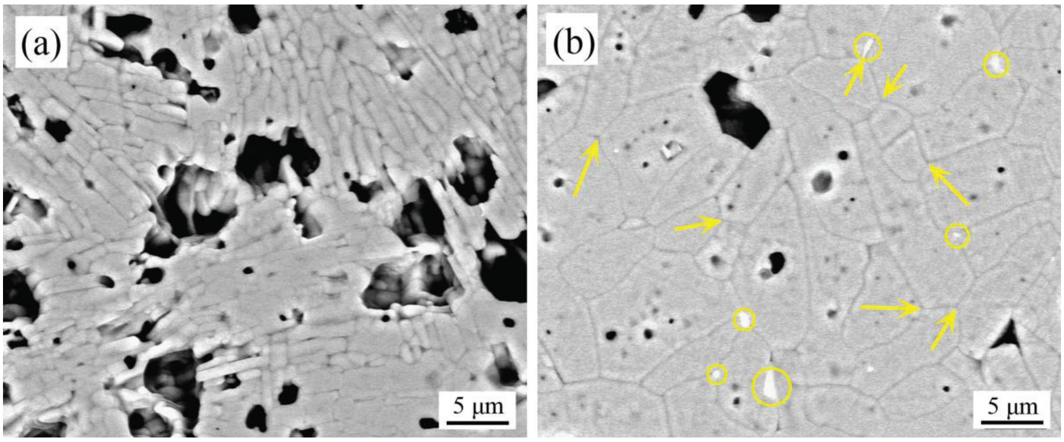

Fig. 6.3 High-magnification SEM images showing the microstructure of CA_6 samples with (a) 0 and (b) 2 wt% TiO_2.

As seen in Fig. 6.3(a), the CA_6 grains exhibited high aspect ratios in pure CA_6 sample. However, most of CA_6 presented a more equiaxed morphology in the Ti^{4+}-doped samples, contributing to denser microstructure. In particular, a lot of grain boundaries intersected with each other at an angel of ~120^o (indicated by the arrows in Fig. 6.3(b), indicating a balance of grain-boundary energy. In addition, it was observed that the $CaTiO_3$ particles (marked by the circles) exhibited equiaxed and elongated morphologies, and most of them were located at the grain boundaries of CA_6. Thus, the crystal growth of CA_6 along basal plane was prohibited to some extent. From the elemental mapping shown in Fig. 6.4, it can be seen that Ti^{4+} was almost homogeneously distributed in the whole CA_6 region, while there existed some regions with concentrated Ti and Ca elements. This suggests that Ti^{4+} has indeed migrated into crystal lattices of CA_6. Combined with the XRD results, the phases pointed by the arrows "A" and "B" are considered to be Al_2O_3 and $CaTiO_3$, respectively. Besides, Ti^{4+} was also found within Al_2O_3 particles, indicating the substitution of Ti^{4+} for Al^{3+} in Al_2O_3. This leads to the generation of V_{Al} and enhanced diffusion of ions, thus promoted grain growth of Al_2O_3 [31-33].

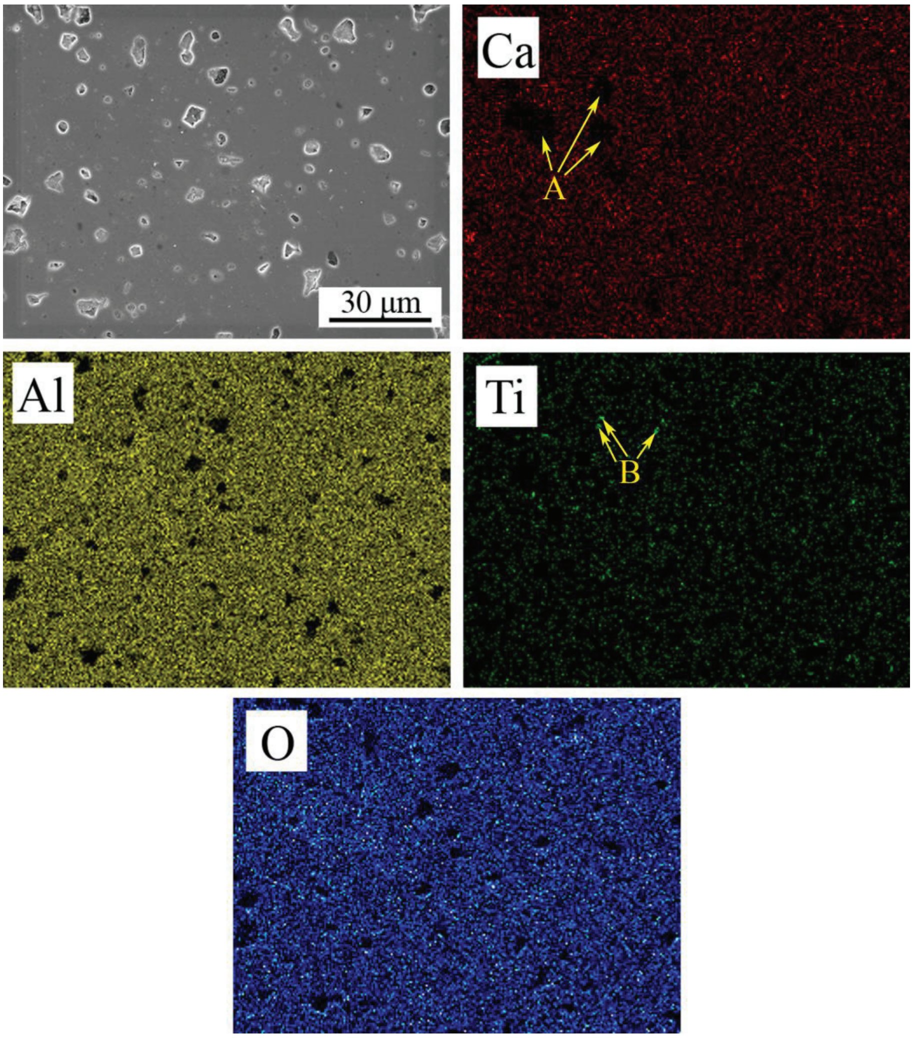

Fig. 6.4 EDS analysis of CA_6 sample with 2 wt% TiO_2.

The measured dimensions of CA_6 grains were also included in Table 6.1. The TiO_2-free CA_6 sample showed a larger average aspect ratio. However, both the length and width increased when 2 wt% TiO_2 was doped, and the aspect ratio decreased significantly. The reduction in aspect ratio is mainly due to more promoted crystal growth along *c*-axis than that along basal plane and the pinning effect of $CaTiO_3$ grains. Moreover, limited differences in lengths, widths, and thus aspect ratios of the CA_6 grains were found while further increasing TiO_2 content up to 4 wt%.

6.3.3 Mechanism of promoted densification

A schematic illustration of the mirror layers of the CA_6 is shown in Fig. 6.5. As discussed before, Ti^{4+} dissolved into the lattices of the CA_6 by substituting for Al^{3+}. In addition, Ti^{4+} has been reported to preferentially occupy the octahedral face-sharing Al site in the mirror layers, rather than trigonal bipyramidal Al site in the mirror layers and the Al site in the spinel blocks [34]. Meanwhile, Al vacancies were formed to make a balance. Considerable vacancy concentration gradients from mirror layers to spinel blocks would be generated along *c*-axis. Subsequently, the crystal growth along *c*-axis was greatly promoted, resulting in the elimination of pores located between/within CA_6 phase. Compared to 2 wt% TiO_2-added sample, the densification enhancement of 4 wt% TiO_2-added sample is mainly attributed to the decreased amount of CA_6 with low sintering ability.

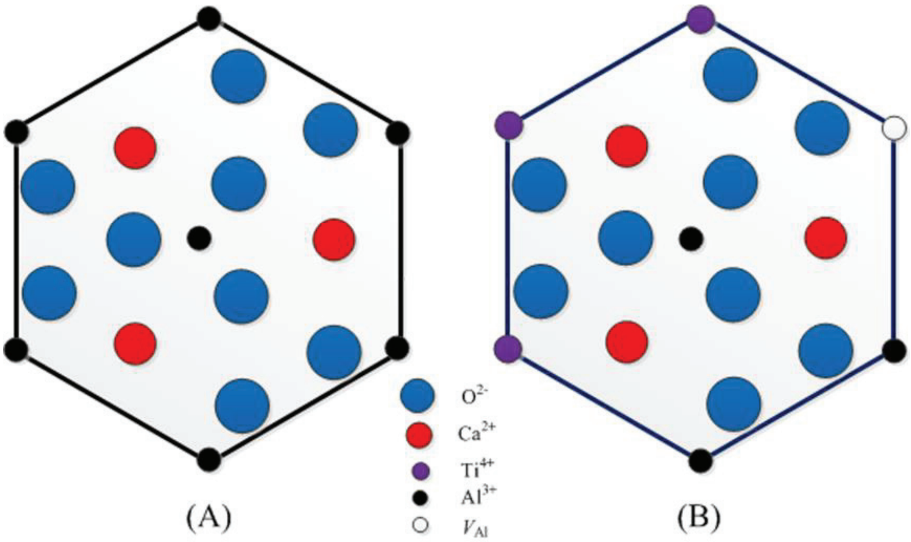

Fig. 6.5 Schematic illustration showing the mirror layers of (A) before doping and (B) after doping.

6.4 Conclusions

Denser CA_6 ceramics with a more equiaxed morphology were successfully fabricated by doping Ti^{4+}. In addition, this also provides a method to optimize the mechanical properties of Al_2O_3/CA_6 composites by tailoring the microstructure of CA_6. The doped Ti^{4+} leads to V_{Al} in mirror planes in CA_6 by replacing Al^{3+}. The crystal growth of CA_6 along c axis was further promoted, thus the aspect ratios of the CA_6 grains were decreased, and higher density was obtained. Meanwhile, Al_2O_3 and $CaTiO_3$ were also formed in Ti^{4+}-doped samples.

References

1. C. Domínguez, J. Chevalier, R. Torrecillas, L. Gremillard, G. Fantozzi, Thermomechanical properties and fracture mechanisms of calcium hexaluminate, J. Eur. Ceram. Soc. 21 (2001) 907–917.
2. C. Domínguez, J. Chevalier, R. Torrecillas, G. Fantozzi, Microstructure development in calcium hexaluminate, J. Eur. Ceram. Soc. 21 (2001) 381–387.
3. R. Salomão, V.L. Ferreira, I.R. de Oliveira, A.D.V. Souza, W.R. Correr, Mechanism of pore generation in calcium hexaluminate (CA_6) ceramics formed in situ from calcined alumina and calcium carbonate aggregates, J. Eur. Ceram. Soc. 36 (2016) 4225–4235.
4. K. Kawaguchi, Y. Suzuki, T. Goto, S.H. Cho, T. Sekino, Homogeneously bulk porous calcium hexaaluminate ($CaAl_{12}O_{19}$): reactive sintering and microstructure development, Ceram. Int. 44 (2018) 4462–4466.
5. X.Y. Liu, D.X. Yang, Z.H. Huang, J.K. Ye, S.W. Zhang, M.H. Fang, H. Ding, Y.G. Liu, In-situ synthesis of porous calcium hexa-aluminate ceramics and growth mechanism of the plate-like grains, Ceram. Int. 41 (2015) 14727–14732.
6. J.H. Chen, H.Y. Chen, W.J. Mi, Z. Cao, B. Li, C.J. Liang, Substitution of Ba for Ca in the structure of $CaAl_{12}O_{19}$, J. Am. Ceram. Soc. 100 (2017) 413–418.
7. M.K. Cinibulk, R.S. Hay, Textured magnetoplumbite fiber-matrix interphase derived from sol-gel fiber coatings, J. Am. Ceram. Soc. 79 (1996) 1233–1246.
8. L. Liu, Y. Takasu, T. Onda, Z.C. Chen, Influence of in-situ synthesized Ba-β-Al_2O_3 on mechanical properties and thermal shock resistance of

ZTA/Ba-β-Al_2O_3 composites, Ceram. Int. 46 (2020) 3738–3743

9. L. An, H.M. Chan, R-curve behavior of in-situ-toughened Al_2O_3: $CaAl_{12}O_{19}$ ceramic composites, J. Am. Ceram. Soc. 79 (1996) 3142–3148.
10. L. Liu, M. Chen, L. Xu, X.L. Yin, W.J. Sun, Effect of BaO addition on densification and mechanical properties of Al_2O_3-MgO-CaO refractories, Metals 6 (2016) 84.
11. L.A. Díaz, R. Torrecillas, F. Simonin, G. Fantozzi, Room temperature mechanical properties of high alumina refractory castables with spinel, periclase and dolomite additions, J. Eur. Ceram. Soc. 28 (2008) 2853–2858.
12. C. Gogtas, H.F. Lopez, K. Sobolev, Role of cement content on the properties of self-flowing Al_2O_3 refractory castables, J. Eur. Ceram. Soc. 34 (2014) 1365–1373.
13. J.M. Auvray, C. Gault, M. Huger, Microstructural changes and evolutions of elastic properties versus temperature of alumina and alumina–magnesia refractory castables, J. Eur. Ceram. Soc. 28 (2008) 1953–1960.
14. J.M. Auvray, C. Gault, M. Huger, Evolution of elastic properties and microstructural changes versus temperature in bonding phases of alumina and alumina–magnesia refractory castables, J. Eur. Ceram. Soc. 27 (2007) 3489–3496.
15. A. Pieta, M.M. Bucko, M. Janus, J. Lis, S. Jonas, Calcium hexaaluminate synthesis and its influence on the properties of CA_2–Al_2O_3-based refractories, J. Eur. Ceram. Soc. 35 (2015) 4567–4571.

16. D. Asmi, I.M. Low, Self-reinforced Ca-hexaluminate/alumina composites with graded microstructures, Ceram. Int. 34 (2008) 311–316.
17. D. Asmi, I.M. Low, Processing of an in-situ layered and graded alumina/calcium-hexaluminate composite: physical characteristics, J. Eur. Ceram. Soc. 18 (1998) 2019–2024.
18. L.N. An, H.C. Ha, H.M. Chan, High-strength alumina/alumina: calcium-hexaluminate layer composites, J. Am. Ceram. Soc. 81 (1998) 3321–3324.
19. A.J. Sanchez-Herencia, R. Moreno, C. Baudin, Fracture behaviour of alumina–calcium hexaluminate composites obtained by colloidal processing, J. Eur. Ceram. Soc. 20 (2000) 2575–2583.
20. A. Altay, M.A. Gulgun, Microstructural evolution of calcium-doped α-alumina, J. Am. Ceram. Soc. 86 (2003) 623–629.
21. Z. Negahdari, M. Willert-Porada, Tailoring the microstructure of reaction-sintered alumina/lanthanum hexaaluminate particulate composites, J. Eur. Ceram. Soc. 30 (2010) 1381–1389.
22. C. Domínguez, R. Torrecillas, Influence of Fe^{3+} on sintering and microstructural evolution of reaction sintered calcium hexaluminate, J. Eur. Ceram. Soc. 18 (1998) 1373–1379.
23. P.G. De La Iglesia, O. Garcia-Moreno, R. Torrecillas, J.L. Menendez, Influence of different parameters on calcium hexaluminate reaction sintering by spark plasma, Ceram. Int. 38 (2012) 5325–5332.

24. S.H. Badiee, S. Otroj, The effect of nano-titania addition on the properties of high-alumina low-cement self-flowing refractory castables, Ceram-Silikaty 55 (2011) 319–325.

25. M.A.L. Braulio, V.C. Pandolfelli, Tailoring the microstructure of cement-bonded alumina–magnesia refractory castables, J. Am. Ceram. Soc. 93 (2010) 2981–2985.

26. W.J. Yuan, C.J. Deng, H.X. Zhu, Effects of TiO_2 addition on the expansion behavior of alumina-magnesia refractory castables, Mater. Chem. Phys. 162 (2015) 724–733.

27. S. Maitra, S. Das, A. Sen, The role of TiO_2 in the densification of low cement Al_2O_3–MgO spinel castable, Ceram. Int. 33 (2007) 239–243.

28. H. Tang, M.H. Fang, C. Tang, Z.H. Huang, H.T. Liu, H.K. Zhu, Y.A. Liu, X.W. Wu, Effect of $LaMgAl_{11}O_{19}$ addition and temperature on the mechanical properties of Al_2O_3-based ceramics, Mater. Sci. Eng. A 655 (2016) 160–167.

29. J.T. Armstrong, G.P. Meeker, J.C. Huneke, G.J. Wasserburg, The blue angel: I. the mineralogy and petrogenesis of a hibonite inclusion from the Murchison meteorite, Geochim. Cosmochim. Ac. 46 (1982) 575–595.

30. K.T. Jacob, G. Rajitha, Gibbs energy of formation of $Ca_3Ti_8Al_{12}O_{37}$ and phase relations and chemical potentials in the system Al_2O_3-TiO_2-CaO, J. Phase. Equilib. Diff. 33 (2012) 293–302.

31. C.J. Wang, C.Y. Huang, Effect of TiO_2 addition on the sintering behavior, hardness and fracture toughness of an ultrafine alumina, Mater. Sci. Eng. A 492

(2008) 306–310.

32. R.D. Bagley, I.B. Cutler, D.L. Johnson, Effect of TiO_2 on initial sintering of Al_2O_3, J. Am. Ceram. Soc. 53 (1970) 136–141.
33. R.J. Brook, Effect of TiO_2 on the initial sintering of Al_2O_3, J. Am. Ceram. Soc. 55 (1972) 114.
34. P.M. Doyle, P.F. Schofield, A.J. Berry, A.M. Walker, K.S. Knight, Substitution of Ti^{3+} and Ti^{4+} in hibonite, Am. Mineral. 99 (2014) 1369–1382.

Chapter 7: Summary

Al_2O_3 is one of the most widely used ceramic materials because of its high strength and hardness, excellent heat and wear resistances. Nevertheless, the large-scale applications of monolithic Al_2O_3 ceramic are very limited due to its relatively low fracture toughness. Compared to direct additions of fibers, whiskers, and platelets, the incorporation of elongated reinforcements with high aspect ratios through in-situ reactions has advantages of reducing processing costs, as well as obtaining denser and more homogeneous microstructure.

In the present work, Al_2O_3/Ba-β-Al_2O_3/ZrO_2 composites were fabricated by solid-state reaction sintering, and the effects of 3 mol% yttria-stabilized zirconia (3YSZ), YSZ with different Y_2O_3 contents, and Y_2O_3 additions on densification behavior, phase evolution, microstructure, and mechanical properties of Al_2O_3/Ba-β-Al_2O_3/ZrO_2 composites were investigated. To improve the mechanical properties and thermal shock resistance of zirconia toughened alumina (ZTA) composites and investigate the interaction mechanism between martensitic transformation toughening of ZrO_2 and crack deflection, crack bridging toughening of in-situ formed elongated phases, $BaCO_3$ was added to the powder mixtures of Al_2O_3 and YSZ, and ZTA/Ba-β-Al_2O_3 composites were fabricated by a solid-state reactive sintering method. The effects of high-energy ball-milling (HEBM) on sintering ability, phase evolution, microstructure, and mechanical properties of Al_2O_3/Ba-β-Al_2O_3/ZrO_2 composites were investigated. In addition, microstructural evolution of Ti^{4+}-doped calcium hexaaluminate ($CaAl_{12}O_{19}$, or CA_6) ceramics was also studied. The main results obtained in the present research can be summarized as follows.

Chapter 1 described the background of the present research. In order to improve the fracture toughness of monolithic Al_2O_3 ceramic, a combination of crack deflection, crack bridging, and martensitic transformation of ZrO_2 from tetragonal to monoclinic phase was proposed to fabricate Al_2O_3/Ba-β-Al_2O_3/ZrO_2 composites.

In Chapter 2, Al_2O_3/Ba-β-Al_2O_3/ZrO_2 composites were fabricated by solid-state reaction sintering of Al_2O_3, $BaZrO_3$, and 3YSZ powders. The effects of YSZ addition on microstructure and mechanical properties have been investigated. The incorporation of YSZ promoted the densification of the composites and formation of tetragonal ZrO_2 phase. The microstructure of the composites was characterized by elongated Ba-β-Al_2O_3 phase and equiaxed ZrO_2 particles including added YSZ and reaction-formed ZrO_2. The Al_2O_3/Ba-β-Al_2O_3/ZrO_2 composites with YSZ addition exhibited improved fracture toughness, as a result of multiple toughening effects including crack deflection, crack bridging, crack branching, and martensitic transformation of ZrO_2 formed by the reactions between Al_2O_3 and $BaZrO_3$. Moreover, owing to the grain refinement of Al_2O_3 matrix, dispersion strengthening of the added YSZ particles, and an increase in density of the composites, the Vickers hardness and flexural strength of Al_2O_3/Ba-β-Al_2O_3/ZrO_2 composites were dramatically enhanced in comparison with the composites without YSZ addition.

In Chapter 3, Al_2O_3 matrix composites containing in-situ formed monoclinic zirconia (m-ZrO_2) and Ba-β-Al_2O_3 were prepared via reactive sintering of Al_2O_3 and $BaZrO_3$ powders. To improve the fracture toughness of Al_2O_3/Ba-β-Al_2O_3/m-ZrO_2

composites, YSZ with different Y_2O_3 contents (1.5YSZ, 2YSZ, and 3YSZ) and Y_2O_3 particles were introduced into Al_2O_3 and $BaZrO_3$ powder mixtures, and the effect of YSZ or Y_2O_3 addition on densification behavior, microstructure, and mechanical properties of Al_2O_3/Ba-β-Al_2O_3/ZrO_2 composites has been investigated. The reaction-formed *m*-ZrO_2 was transformed into tetragonal ZrO_2 (*t*-ZrO_2), resulting from the migration of Y^{3+} from YSZ or Y_2O_3. The incorporation of YSZ particles contributed to the refinement of Al_2O_3 grains, whereas Y_2O_3-added samples showed larger grain sizes of Al_2O_3 matrix. The Al_2O_3/Ba-β-Al_2O_3/ZrO_2 composites with YSZ or Y_2O_3 addition exhibited high fracture toughness, which is attributed to crack deflection/bridging and $t \rightarrow m$ transformation toughening. Although the phase transformation is mainly derived from ZrO_2 formed during sintering, 1.5YSZ particles added in the composites still showed much higher phase transformability compared to 2YSZ and 3YSZ particles.

In Chapter 4, Al_2O_3/Ba-β-Al_2O_3/ZrO_2 composites were prepared by solid-state reaction sintering of high-energy ball-milled Al_2O_3–$BaZrO_3$ powder mixtures and 3YSZ nanopowder. The powder characterization of Al_2O_3 and $BaZrO_3$ powders as well as sintering behavior and microstructure of Al_2O_3/Ba-β-Al_2O_3/ZrO_2 composites were investigated in this chapter. After HEBM for 48 h, the particle size of $BaZrO_3$ was significantly reduced. However, no evident particle refinement of Al_2O_3 occurred. The Ba-β-Al_2O_3 phase presented a more equiaxed morphology instead of platelet structure, which enhanced the densification of the composites. Al_2O_3/Ba-β-Al_2O_3/ZrO_2 composites sintered at 1500 °C, based on powders ball-milled for 72 h, presented the highest Vickers hardness of 17.3 GPa. Meanwhile, the composites sintered at 1600 °C, based on powders without HEBM, presented the highest fracture toughness of 4.3 MPa $m^{1/2}$.

In Chapter 5, to improve the mechanical properties and thermal shock resistance of ZTA composites, $BaCO_3$ was added to 3YSZ and Al_2O_3 powders to form ZTA/Ba-β-Al_2O_3 composites, which were prepared by a solid-state reactive sintering method. As $BaCO_3$ content increased, more Ba-β-Al_2O_3 was formed, resulting in the decreases in relative density and Vickers hardness. The fracture toughness was enhanced with increasing $BaCO_3$ content and reached a peak at 4 wt% $BaCO_3$. The improved fracture toughness is the result of synergistic toughening effects of martensitic transformation of ZrO_2 and crack deflection/bridging. After thermal shock tests, the residual strength of ZTA/Ba-β-Al_2O_3 composites was higher than that of ZTA. The improvement in thermal shock resistance is mainly ascribed to the formation of elongated Ba-β-Al_2O_3 with a hexagonal structure, which can dissipate the energy associated with crack propagation during thermal shock.

In Chapter 6, CA_6 ceramics were fabricated by reactive sintering of Al_2O_3 and $CaCO_3$ powder mixtures. Owing to the suppressed interlayer diffusion of ions, the elongated CA_6 phase with high aspects ratios was formed, and the open porosity of CA_6 ceramics was high (22.5%). Al vacancies (V_{Al}) in mirror planes of CA_6 were created by the incorporation of Ti^{4+}, the diffusion rate of ions along c axis was accelerated and thus the crystal growth of CA_6 along c axis was facilitated. As a result, the aspect ratios of the CA_6 were decreased, and the densification was significantly promoted. In particular, low open porosity value of 8.2% was obtained when 4 wt% TiO_2 was added. $CaTiO_3$ was formed in TiO_2-added samples due to the reactions between CaO and TiO_2, thus residual Al_2O_3 was observed.

Evaluation of high-temperature mechanical properties and thermal stability of the composites will be performed in our future work.

Achievements

Journal publications

1. Lei Liu, Kensaku Maeda, Tetsuhiko Onda, Zhong-Chun Chen, Microstructure and improved mechanical properties of Al_2O_3/Ba-β-Al_2O_3/ZrO_2 composites with YSZ addition. Journal of the European Ceramic Society, 38 (2018) 5113–5121. (SCI, IF=4.029)
2. Lei Liu, Kensaku Maeda, Tetsuhiko Onda, Zhong-Chun Chen, Effect of YSZ with different Y_2O_3 contents on toughening behavior of Al_2O_3/Ba-β-Al_2O_3/ZrO_2 composites. Ceramics International, 45 (2019) 18037–18043. (SCI, IF=3.450)
3. Lei Liu, Yu Takasu, Tetsuhiko Onda, Zhong-Chun Chen, Influence of in-situ formed Ba-β-Al_2O_3 on mechanical properties and thermal shock resistance of ZTA/Ba-β-Al_2O_3 composites. Ceramics International, 46 (2020) 3738–3743. (SCI, IF=3.450)
4. Lei Liu, Tetsuhiko Onda, Zhong-Chun Chen, Microstructural evolution of Ti^{4+}-doped calcium hexaaluminate ceramics. Ceramics International, in press. (SCI, IF=3.450)
5. Lei Liu, Hiraku Oda, Tetsuhiko Onda, Zhong-Chun Chen, Microstructure and thermoelectric properties of higher manganese silicides fabricated via gas atomization and spark plasma sintering. Materials Chemistry and Physics, revise. (SCI, IF=2.781)

International conferences

1. Lei Liu, Kenta Sakuragawa, Yu Takasu, Kensaku Maeda, Tetsuhiko Onda, Zhong-Chun Chen, Toughening and strengthening of Al_2O_3/Ba-β-Al_2O_3/*m*-ZrO_2 composites with TZP addition. The 60th JSPM International Conference on Powder and Powder Metallurgy, Kyoto, Japan, Nov. 2017.
2. Lei Liu, Tetsuhiko Onda, Zhong-Chun Chen, Microstructure and improved mechanical properties of Al_2O_3/Ba-β-Al_2O_3/ZrO_2 composites with YSZ addition. The 7th Joint Symposium on Materials and Mechanical Engineering between Northeastern University and Tottori University, Shenyang, China, Sep. 2018.
3. Lei Liu, Kensaku Maeda, Tetsuhiko Onda, Zhong-Chun Chen, Effect of YSZ with different Y_2O_3 contents on toughening behavior of Al_2O_3/Ba-β-Al_2O_3/ZrO_2 composites. The 36th International Japan-Korea Seminar on Ceramics, Tottori, Japan, Nov. 2019.

Domestic conferences

1. Lei Liu, Tetsuhiko Onda, Zhong-Chun Chen, Microstructure and mechanical properties of Al_2O_3/Ba-β-Al_2O_3/ZrO_2 composites with YSZ addition. The 58th Chugoku Shikoku Branch Meeting of the Japan Institute of Metals and Materials, Kagawa, Japan, Aug. 2018.
2. Lei Liu, Tetsuhiko Onda, Zhong-Chun Chen, Influence of in-situ synthesized Ba-β-Al_2O_3 on mechanical properties and thermal shock resistance of ZTA/Ba-β-Al_2O_3 composites. The 31st Fall Meeting of the Ceramic Society of Japan, Nagoya, Japan, Sep. 2018.

3. Lei Liu, Hiraku Oda, Tetsuhiko Onda, Noriharu Yodoshi, Takeshi Wada, Zhong-Chun Chen, Microstructure and thermoelectric properties of higher manganese silicides fabricated via gas atomization and spark plasma sintering. The 59th Chugoku Shikoku Branch Meeting of the Japan Institute of Metals and Materials, Ehime, Japan, Aug. 2019.
4. Lei Liu, Kanta Okumura, Tetsuhiko Onda, Noriharu Yodoshi, Takeshi Wada, Zhong-Chun Chen, Microstructure and thermoelectric properties of Cr-doped higher manganese silicides fabricated via gas atomization and spark plasma sintering. The 165st Annual Fall Meeting of the Metals and Materials, Okayama, Japan, Sep. 2019.

Acknowledgments

First and foremost I would like to thank my supervisor, Prof. Zhong-chun Chen, for his educational support during the past three years. His diligent working attitude and rigorous research methods taught me so much from research to life. I am deeply indebted to him and truly appreciate his professional advices, guidance, and discussions in accomplishing this thesis.

Worth to be mentioned, I am also indebted to my former supervisor, Prof. Min Chen (Northeastern University, China), who initially led me to the field of ceramic materials.

I would like to thank Dr. Tetsuhiko Onda for his experimental help and fruitful discussions.

Many thanks should also go to previous and present members in *Laboratory of Materials Engineering, Tottori University*: Dr. Li-fu Yi, Mr. Kensaku Maeda, Mr. Kenta Sakuragawa, and Miss Yu Takasu for their collaborative work.

This work was financially supported by JSPS KAKENHI Grant Number 23560835 and Electric Technology Research Foundation of Chugoku.

Finally, I am deeply grateful to my parents and girlfriend for their love, sacrifice, and encouragement.